ADA031828

PREDICTION OF SUPERSONIC STORE SEPARATION CHARACTERISTICS
VOLUME I. - THEORETICAL METHODS AND COMPARISONS WITH EXPERIMENT

NIELSEN ENGINEERING & RESEARCH, INC.
MOUNTAIN VIEW, CALIFORNIA 94043

MAY 1976

D D C

NOV 10 1976

B

When Government drawings, specifications, or other data are used for any purpose other than in connection with a definitely related Government procurement operation, the United States Government thereby incurs no responsibility nor any obligation whatsoever; and the fact that the Government may have formulated, furnished, or in any way supplied the said drawings, specifications, or other data, is not to be regarded by implication or otherwise as in any manner licensing the holder or any other person or corporation, or conveying any rights or permission to manufacture, use, or sell any patented invention that may in any way be related thereto.

This technical report has been reviewed and is approved for publication.

FOR THE COMMANDER

E. H. Flinn, Chief
Control Criteria Branch
Flight Control Division

Calvin L. Dyer
Project Engineer
Control Criteria Branch
Flight Control Division

Lt Col Larry M. Hadley, Chief
Flight Control Division

Copies of this report should not be returned unless return is required by security consideration, contractual obligations, or notice on a specific document.

AIR FORCE - 1 OCTOBER 76 - 175

REPORT DOCUMENTATION PAGE	READ INSTRUCTIONS BEFORE COMPLETING FORM

1. REPORT NUMBER	2. GOVT ACCESSION NO.	3. RECIPIENT'S CATALOG NUMBER
AFFDL-TR-76-41, Vol. I		

Final Rept. 24 Feb 75 - 24 Mar 76

4. TITLE (and Subtitle)	5. TYPE OF REPORT & PERIOD COVERED
PREDICTION OF SUPERSONIC STORE SEPARATION CHARACTERISTICS Volume I. Theoretical Methods and Comparisons with Experiment	Final Technical 2/24/75 to 3/24/76
	6. PERFORMING ORG. REPORT NUMBER NEAR-TR-105

7. AUTHOR(s)	8. CONTRACT OR GRANT NUMBER(s)
Marnix F. E. Dillenius, Frederick K. Goodwin, and Jack N. Nielsen	F33615-75-C-3053

9. PERFORMING ORGANIZATION NAME AND ADDRESS	10. PROGRAM ELEMENT, PROJECT, TASK AREA & WORK UNIT NUMBERS
Nielsen Engineering & Research, Inc. 510 Clyde Avenue Mountain View, CA 94043	Program Element 62201 F 8219-01-13

11. CONTROLLING OFFICE NAME AND ADDRESS	12. REPORT DATE
Air Force Flight Dynamics Laboratory (FGC) Wright-Patterson Air Force Base Ohio 45433	May 1976
	13. NUMBER OF PAGES 162

14. MONITORING AGENCY NAME & ADDRESS(if different from Controlling Office)	15. SECURITY CLASS. (of this report)
AFFDL	Unclassified
	15a. DECLASSIFICATION DOWNGRADING SCHEDULE

16. DISTRIBUTION STATEMENT (of this Report)

Approved for public release; distribution unlimited.

TR-76-41-Vol-1

17. DISTRIBUTION STATEMENT (of the abstract entered in Block 20, if different from Report)

18. SUPPLEMENTARY NOTES

19. KEY WORDS (Continue on reverse side if necessary and identify by block number)

Aerodynamic Loads	Flow Fields
Aerodynamic Interference	Store Separation
External Stores	Supersonic Flow

20. ABSTRACT (Continue on reverse side if necessary and identify by block number)

The primary objective of this report is to describe an investigation to develop a method for predicting the separation characteristics of a store released from a supersonic parent aircraft. The present computer program is designed to handle configurations consisting of a wing without dihedral or incidence which is attached to an axisymmetric fuselage. A pylon can be attached to the wing or under the fuselage.

over

DD FORM 1473 1 JAN 73   EDITION OF 1 NOV 65 IS OBSOLETE

389783

Block 20 Continued.

In this work, supersonic flow models are described to represent the configuration and special attention is given to the flow field calculation method. It is shown that the basic method utilizing linear, potential flow theory must be corrected for nonlinear effects caused by the shock from the wing leading edge. Experimental results are presented from a wind-tunnel test program designed to provide data to aid in developing and testing the theory. Comparisons between theory and experiment for flow fields, store loading distributions and store forces and moments indicate fair to very good agreement. Recommendations are given for improving the present method.

ACCESSION for

NTIS	White Section	☑
DDC	Buff Section	☐
UNANNOUNCED		☐
JUSTIFICATION		

BY
DISTRIBUTION/AVAILABILITY CODES

| Dist. | AVAIL. and/or SPECIAL |

A

FOREWORD

This report, "Prediction of Supersonic Store Separation Characteristics," describes a combined theoretical-experimental program directed toward developing a computer program for predicting the trajectory of an external store separated from an aircraft flying at supersonic speed. This volume, Volume I.- "Theoretical Methods and Comparisons with Experiment," describes the theoretical approach and presents extensive comparisons with experimental data. The second volume, Volume II.- "Users Manual for the Computer Program," presents detailed instructions on the use of the computer program.

The work documented in this report was started on February 24, 1975 and was effectively concluded with the submission of this report. The report was submitted by the authors in March 1976.

TABLE OF CONTENTS

TABLE OF CONTENTS (CONCLUDED)

LIST OF ILLUSTRATIONS

LIST OF ILLUSTRATIONS (CONCLUDED)

LIST OF SYMBOLS

a_1 panel left-side length, figure 2

a_2 panel right-side length, figure 2

c panel chord passing through the centroid, figure 2; local wing chord

c_m store pitching-moment coefficient, pitching moment/$q_{\infty_s} S_R \ell_R$; positive nose up and taken about store midpoint

c_n store yawing-moment coefficient, yawing moment/$q_{\infty_s} S_R \ell_R$; positive to the right and taken about store midpoint

c_N store normal-force coefficient, normal force/$q_{\infty_s} S_R$; positive up

c_Y store side-force coefficient, side force/$q_{\infty_s} S_R$; positive to the right when viewing upstream

d maximum store diameter; Appendix III, diameter of circular forebody, figure III-2

d' length associated with sonic point location, figure III-2, Appendix III

$d(\xi)$ function associated with line doublet strength

$f(\xi)$ function associated with line source strength

F_1, F_2, F_4, F_5, F_7 geometric functions defined in Appendix II

F_u, F_v, F_w aerodynamic influence functions defined by equation (12)

$F_{u_t}, F_{v_t}, F_{w_t}$ aerodynamic influence functions defined by equation (14)

h panel span, figure 2

K constant associated with line source strength function $f(\xi)$, equation (I-8)

K_d constant associated with line doublet strength function $d(\xi)$, equation (I-22)

ℓ_R reference length, taken equal to d

ℓ_s length of store

M_ℓ local Mach number defined by equation (28)

$m_{\ell e}$ tangent of leading-edge sweep angle associated with semi-infinite triangle

M_N Mach number in direction normal to wing leading edge

M_∞ free-stream Mach number

MP   number of constant u-velocity panels on the pylon

n   running index governing constant u-velocity panels; Appendix I, running index governing body definition points and line singularities

nt   running index governing constant source panels

NPANLS   number of constant u-velocity panels on left wing

NPTOT   total number of constant u-velocity panels

NXBODY   number of line singularities used to model fuselage or store

p   local static pressure

p_α free-stream static pressure

q_{α_s} free-stream dynamic pressure associated with the store

$R(x_B)$ function relating body radius to x_B

S   surface in Appendix II

S_R reference area, $\pi d^2/4$

u_+ axial velocity in x-direction in the constant u-velocity panel or semi-infinite triangle, figure 3

u_- axial velocity immediately below the constant u-velocity panel or semi-infinite triangle, figure 3

$\dfrac{u_+}{V}$ strength of constant u-velocity panel with u_+ equal to the axial velocity u in the panel

u,v,w   section 3, perturbation velocity components in the x,y,z directions; section 3.3.4, perturbation velocity components in the coordinate system associated with the semi-infinite triangle, figure 3; figures 8 through 16 and 19 through 22, velocity components with u positive back, positive v to the right when viewing upstream and positive w upwards

u_B, v_B, w_B section 3.2, perturbation velocity components in the x_B, r_B, θ directions

u_t, v_t, w_t	perturbation velocity components associated with a semi-infinite, constant source triangle in the x, y, z directions, figure 3
u_W, v_W, w_W	perturbation velocity components in the x_W, y_W, z_W directions, figure 1
V_∞	free-stream velocity
x_S	length along the store measured from nose
x_O	shock location, figure III-2, Appendix III
x, y, z	section 3, rectangular coordinate system with x-axis in the free-stream direction; section 3.3.4, coordinate system associated with semi-infinite triangle, figure 3
x_B, y_B, z_B	fuselage coordinate system with its origin fixed at the nose, figure 1; section 3.2, coordinate system used with fuselage/store flow model
x_B, r_B, θ	section 3.2, cylindrical coordinate system associated with fuselage/store flow model
x_W, y_W, z_W	wing coordinate system with origin in vertical plane of symmetry, figure 1
Δz	distance down from attached store position
α_f	angle of attack of the fuselage and wing
α_ℓ	local angle of attack due to twist and camber; section 5.3.2, local upwash flow angle
β	$\sqrt{M_\infty^2 - 1}$
δ_{cone}	vertex angle of cone
δ_{det}	wedge angle for shock detachment
ϵ_s	shock wave angle for sonic flow behind the shock
η	angle between normal to the free stream and the control line, figure III-2, Appendix III
ϑ	angle associated with streamwise thickness slope
ϑ_N	angle associated with thickness slope measured normal to the wing leading edge
μ	section 3.3.3, running index governing the constant u-velocity panels on the body interference shell; Mach cone angle, $\mu = \sin^{-1}(1/M_\infty)$

ν	running index governing control points; section 3.4.1, Prandtl-Meyer angle; Appendix III, variable along the conormal
ξ	dummy variable in Appendix I
$\xi_0, \xi_1, \xi_2 ..$	starting points of line singularities
ξ, η, ζ	dummy coordinate system used in Appendix II
σ	variable of integration defined by equation (I-5) in Appendix I
σ_ℓ	section 5.3.2, local sidewash angle, positive to the right
τ	domain of dependence in Appendix II
ψ	complete potential for an axisymmetric body; section 3.3.3, body panel orientation angle
ϕ_a	axisymmetric body potential for zero angle of attack
ϕ_c	crossflow potential associated with axisymmetric body
ψ	sweep angle
Ω	potential or velocity component in equation (II-2), Appendix II

SUBSCRIPTS

a	axial
B	body
c	crossflow
d	doublet
i	induced
Le, ℓe	leading edge
N	normal
s	store
t	thickness
TE, te	trailing edge
W	wing
1, 2, 3, 4	numbers of panel corners

xiii

PREDICTION OF SUPERSONIC STORE
SEPARATION CHARACTERISTICS

Volume I.- Theoretical Methods and
Comparisons with Experiment

1. INTRODUCTION

This report presents the results of a combined theoretical/experimental research program aimed at extending the subsonic six-degree-of-freedom store separation trajectory prediction method of references 1 and 2 to supersonic speeds. The accompanying computer program is described in Volume II of this report, reference 3. Data from the experimental part of the program are available in reference 4.

The theoretical work reported herein is the result of the initial effort towards building up a supersonic store separation trajectory method and computer program which will eventually have the same capabilities as the subsonic method and program described in references 1 and 2. With this view, the input and output of the supersonic computer program have been designed to resemble the existing subsonic program to the maximum possible extent. Following the subsonic approach, the present and future work are designed to proceed from simple configurations to more complicated ones in flow modeling and store load calculation methods. The present computer program is designed to handle a configuration consisting of an axisymmetric fuselage and a wing without dihedral with one pylon per half-wing or one pylon under the fuselage. Both the wing and pylon may have thickness and the wing-fuselage junction may be off the midplane. This configuration can be viewed as a basic one to which other components can be attached and included in the flow model systematically as was done during the advanced phases of the subsonic work. As such, the present program is the logical starting point for one which will ultimately predict store separation trajectories from aircraft with features such as a noncircular fuselage, air inlets, and MER and TER store groupings.

The experimental program carried out in conjunction with the theoretical work was directed towards providing data to aid in the development of the flow models for the wing, pylon, and fuselage components. In order to isolate pylon effects, data were taken with and without the pylon. The data consist of flow field surveys, store pressure distributions, and store forces and moments.

The next section of this report describes in considerable detail the flow models based on linear, potential flow theory for the components of the supersonic aircraft and the store. A special section is devoted to nonlinear aspects of the flow field; namely, effects associated with blunt wing leading edges and shock waves that do not coincide with Mach lines. Following this the store force distribution and total force and moment calculation methods are summarized and certain significant aspects are discussed. In connection with the loading calculation methods and the trajectory calculation method, reference is made to the applicable subsonic work of references 1, 2, and 5.

Finally, comparisons are made between theory and results obtained during the wind-tunnel test program in order to assess the accuracy of the theoretical methods in predicting flow fields about a wing-fuselage configuration with and without the pylon. Comparisons are shown for three Mach numbers and two angles of attack. For some of these conditions, comparisons are presented between the measured and predicted store load distributions and forces and moments. In addition, flow field comparisons are made using a different wind-tunnel model. Problem areas requiring further attention are indicated and recommendations are made to improve the present method.

2. GENERAL APPROACH

It is possible to determine the forces and moments acting on an external store in the presence of a parent aircraft in the following manner. Consider first the entire airframe excluding the store in question. The nonuniform flow field, induced by the flow model representing the airframe, is computed in the region occupied by the store. If the store is now placed in this nonuniform flow field, then the calculated loading acting on it includes primary interference. The primary interference can be viewed as the first term in an iterative procedure. Higher-order solutions would be generated as follows. After modeling the store subjected to the primary interference flow field, its effects on the airframe can be determined. These effects, in terms of velocities normal to the wing, pylon, and fuselage, must then be cancelled by an additional set of singularities distributed over these components. A new nonuniform flow field can now be computed in the region occupied by the store, and the loading acting on it can be recalculated. At this stage, the result is associated with the second term in the iteration procedure. The

2

difference between the results of the second and the first loading calculation is due to additional interference. This process can be continued until the effects of additional interference become negligible.

For the purpose of expediting the procedure mentioned above, the approach taken here for supersonic flow, which was used during the earlier subsonic work (refs. 1, 2, and 5), involves a modification to the first iteration after which the calculation is stopped. The modification consists of including in the first iteration the effects of the store in the boundary condition applied to the airframe flow model. In general, the flow field under the wing tends to align itself with the wing. Since the store diameters are usually small compared to the local wing chord, the induced sidewash and downwash at points on the wing due to crossflow over the store are very small. Volume effects can be important in connection with the shock associated with the store nose. At this point, the calculated store loads can be looked upon as the result of one and one-half iterations. The success of this method depends on the degree to which the primary interference, accounted for in this way, encompasses the significant effects. Methods for calculating additional interference have been developed in reference 5 for the subsonic case. It is shown that the effect due to this interference on store loading is small, provided that important interference causing components such as the pylon are included as part of the airframe.

For the supersonic case, store volume effects are expected to be significant if the store nose shock intersects the wing and reflects back onto the store. In this situation, the nonuniform flow field in which the store is actually submerged may be heavily influenced by the store nose shock reflected off the wing. It is for this reason that the store volume effects should be included in the first iteration. An important advantage realized by this method is that the need for resolving the complete mutual interference problem between the separated store and airframe throughout the trajectory is eliminated, thereby saving large amounts of computer time. If the store nose shock influences the airframe appreciably, the method has a disadvantage in that the airframe loading must be recomputed as the store drops away. At present, the computer program does not recalculate the aircraft loadings during a store trajectory, but means for simply overcoming this difficulty are subsequently recommended.

3

The flow models used to represent the aircraft components and store in supersonic flow will be discussed and the geometric parameters of the various components and the flight conditions described. The fuselage is flow modeled first and its effects on the wing-pylon combination determined. Certain terms in the flow tangency boundary conditions are explained in relation to the mutual interference between the aircraft components. Shocks associated with the wing leading edge receive special attention because of their influence on the interference flow field. Methods for determining the store forces, moments, and trajectories are summarized.

3. FLOW MODELS

In general, the flow models for the components to be described are based on linear theory for steady, inviscid flow. Because the flow regime considered here is supersonic, the associated potential flow is governed by the wave equation. In a rectangular coordinate system (x,y,z) with the x-axis in the direction of the free-stream vector, the potential ϕ is given by

$$(M_\infty^2 - 1) \frac{\partial^2\phi}{\partial x^2} - \frac{\partial^2\phi}{\partial y^2} - \frac{\partial^2\phi}{\partial z^2} = 0 \tag{1}$$

This equation is valid if the perturbation velocities u,v,w given below in terms of the potential are small.

$$\left. \begin{array}{l} u = \dfrac{\partial\phi}{\partial x} \\[2mm] v = \dfrac{\partial\phi}{\partial y} \\[2mm] w = \dfrac{\partial\phi}{\partial z} \end{array} \right\} \tag{2}$$

Because of the linearity of the potential ϕ in equation (1), it is possible to make use of superposition. This principle allows for the representation of the aircraft components by distributions of potentials or singularities. Flow conditions at a given field point are given by the summed influences of all the singularities. In particular, the influence of each singularity is included in the flow tangency condition as will be shown in a later discussion concerned with the flow tangency

4

condition. Before describing the flow models in detail, the geometric characteristics of the airframe and store are listed next.

3.1 Description of Aircraft Components and Flight Conditions

The configuration of interest consists of a wing attached to a fuselage. A pylon can be positioned under the wing or under the fuselage centerline.

The geometric parameters of the aircraft components described below are accounted for in the computer program. Flight conditions cover the supersonic speed regime and are specified below together with the expected range of validity of the present method.

3.1.1 Fuselage

The fuselage is axisymmetric and has a pointed nose. A fuselage meridian is described by a set of polynomials. The afterbody need not be pointed.

3.1.2 Wing

The wing may have twist and camber and the leading and trailing edges can have breaks in sweep. Dihedral angle and incidence relative to the fuselage centerline are not accounted for. Vertical location of the wing attachment on the fuselage is not limited to the midplane. Effects of wing thickness are included in the program. The wing leading edge can be blunt or sharp.

3.1.3 Pylon

Leading and trailing edges may be swept without breaks in sweep. The length of the pylon root chord need not equal the local wing chord. Thickness is accounted for and the leading edge can be blunt or sharp. The pylon can be located under the wing or fuselage but is aligned with the free stream.

3.1.4 Store

The general shape is a body of revolution with a pointed nose. A body meridian is described by a set of polynomials. The store can have one set of planar or cruciform stabilizing fins. The present program will only handle a single store. Initial velocity, pitch angle and position, and the initial rolling, pitching, yawing rates can be prescribed. The store may be powered with a specified thrust-time history. Store mass and moments of inertia are constant and the center of gravity may be located off the longitudinal axis.

5

3.1.5 Flight conditions

The flight path is straight, angle of attack is constant, and angle of sideslip is zero. The Mach number should lie between 1.2 and 3.0. The angle of attack should be in the $0°-10°$ range.

The flow model for each of the components will be described next. It will be shown how the mutual interference between the wing, pylon, and fuselage is accounted for.

3.2 Flow Model for the Fuselage and Store Body

The potential flow method used to represent an axisymmetric body at incidence in supersonic flow is discussed in this section. The basic theory is given in references 6, 7, and 8. Fundamentally, an axisymmetric body in supersonic flow can be represented by a distribution of line sources or sinks and doublets on the body centerline to account for volume and angle of attack effects, respectively. The strengths of these singularities are determined from the flow tangency conditions applied at points on the body surface. Consider a body of revolution and the cylindrical coordinate system used in the solution as shown in the following sketch. The angle between body centerline and free-

stream direction, α_f, is assumed small. Velocity component w_B is tangent to the body contour in the crossflow plane and velocity component v_B is positive in the radially outward direction. It is, therefore, necessary only to consider the flow tangency in the meridian plane because w_B is already tangent to the body surface. In any meridian plane the body contour is given by
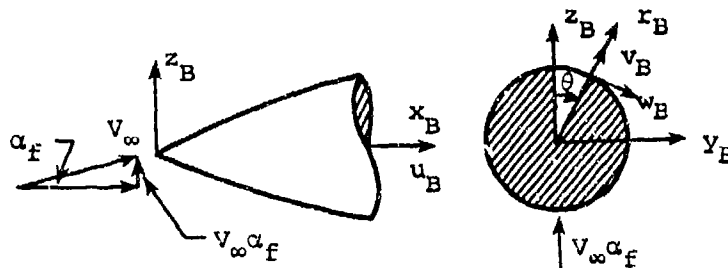
$$r_B = R(x_B) \tag{3}$$

The flow tangency boundary condition at the body surface is

$$\frac{\dfrac{v_B}{V_\infty} + \alpha_f \cos\theta}{1 + \dfrac{u_B}{V_\infty}}\Bigg|_{\substack{\text{body}\\\text{surface}}} = \frac{dR}{dx_B} \tag{4}$$

The governing potential, equation (1), is now expressed in the cylindrical coordinate system shown in the sketch above as

$$(M_\infty^2 - 1)\frac{\partial^2\phi}{\partial x_B^2} - \frac{1}{r_B}\frac{\partial\phi}{\partial r_B} - \frac{1}{r_B^2}\frac{\partial^2\phi}{\partial\theta^2} - \frac{\partial^2\phi}{\partial r_B^2} = 0 \tag{5}$$

Because of the linear character of this equation, the complete solution ϕ can be written as the sum of two potentials.

$$\phi(x_B, r_B, \theta) = \phi_a(x_B, r_B) + \phi_c(x_B, r_B, \theta) \tag{6}$$

which satisfies equation (5). These solutions are called the axial and crossflow potentials, respectively. The perturbation velocities are related to the two potentials by

$$\left.\begin{aligned}
\frac{u_B}{V_\infty} &= \frac{\partial\phi_a}{\partial x_B} + \frac{\partial\phi_c}{\partial x_B}\\[2mm]
\frac{v_B}{V_\infty} &= \frac{\partial\phi_a}{\partial r_B} + \frac{\partial\phi_c}{\partial r_B}\\[2mm]
\frac{w_B}{V_\infty} &= \frac{1}{r_B}\frac{\partial\phi_c}{\partial\theta}
\end{aligned}\right\} \tag{7}$$

Equation (4) can therefore be split into two parts for bodies of revolution as follows.

$$\frac{\dfrac{\partial\phi_a}{\partial r_B}}{1 + \dfrac{\partial\phi_a}{\partial x_B}}\Bigg|_{\substack{\text{body}\\\text{surface}}} = \frac{dR}{dx_B} \; ; \; \text{axial flow} \tag{8a}$$

7

$$\frac{\dfrac{\partial \phi_c}{\partial r_B} + \alpha_f \cos \theta}{\dfrac{\partial \phi_c}{\partial x_B}} \Bigg|_{\substack{\text{body} \\ \text{surface}}} = \frac{dR}{dx_B} \quad ; \text{ crossflow} \tag{8b}$$

It is noted that equation (8a) is the boundary condition for the axial flow problem with free-stream velocity, V_∞. Similarly, equation (8b) involves only crossflow velocities and is the boundary condition for the crossflow problem with crossflow velocity, $V_\infty \alpha_f$. The sum of equations (8a) and (8b) yields the complete flow tangency condition, equation (4). Thus, the first term on the right-hand side of equation (6) together with equation (8a) constitute the axial flow problem. The second term on the right-hand side of equation (6) together with equation (8b) formulate the crossflow problem. These two problems are uncoupled and can therefore be solved separately. Adding the two solutions will satisfy equations (4) and (5) exactly.

The choice of singularity types or potentials for the axial and crossflow problems is described in some detail in Appendix I. This appendix also shows the incorporation of the boundary conditions (8a) and (8b) in the determination of the singularity strengths for the two problems. A distribution of supersonic cone solutions along the body axis will be used to solve the axial flow problem. The crossflow problem is solved by means of a distribution of supersonic line doublets along the body axis. Collectively, these singularity distributions form the flow model for a body of revolution in supersonic flow based on linear, potential flow theory. Presently, the nonlinear effects of the shock associated with the fuselage nose or store nose are not accounted for in the computer program. Instead, the first effects of the fuselage or store when traversing along a line parallel to the centerline are based on linear theory and are determined by the Mach cone from the nose.

3.3 Flow Model for Wing-Pylon Combination and Interference Shell on the Fuselage

This section describes the representation of the wing-pylon in terms of elements from linear, potential flow theory. Also, the methods used to account for mutual interference between the wing-pylon and the fuselage are discussed. Specifically, constant u-velocity panels are distributed over the wing, pylon, and part of the fuselage. These panels

were originally called constant pressure panels by Woodward in reference 9. In addition, constant source panels distributed over the wing and pylon account for thickness effects. The constant u-velocity panels laid out on the fuselage form the interference shell and serve primarily to cancel interference effects from the wing-pylon combination.

3.3.1 Geometrical layout

The leftwing and pylon and the left half of the fuselage are divided up into area panels of trapezoidal shape. The right half of the airframe is accounted for by employing symmetry properties discussed later. Figure 1 shows a swept wing-swept pylon combination attached to a fuselage above its midplane. The rectangular coordinate systems used in the layout part of the computer program and associated with the fuselage (x_B, y_B, z_B) and the wing (x_W, y_W, z_W) are shown. The origin of the former is at the fuselage nose. The wing coordinate system has its origin in the $y_B = 0$ plane at the point where it is intersected by the line connecting the leading edges of the root chords of the left and right wing halves. The coordinate system (x, y, z) with its origin at corner 1 of the cross-hatched panel is associated with a semi-infinite triangle which is part of the solution for the panel to be described later.

A distribution of constant u-velocity type panels to model loading and a distribution of constant source type panels to model thickness will be laid out on the wing and pylon. The distributions of the two types of panels need not be the same in the chordwise direction, but they do coincide in the spanwise direction. The sides of both types of panels are taken parallel to the centerline of the fuselage. Their leading and trailing edges are swept along constant percent chordlines of the wing or pylon. A leading or trailing edge is called subsonic or supersonic depending on whether or not the component of the free-stream velocity perpendicular to the edge in question is subsonic or supersonic, respectively. Figure 1 shows a simplified layout of 2 chordwise by 6 spanwise panels on the left wing half. A distribution of 2 chordwise by 2 spanwise panels covers the pylon. Generally, more panels are required to obtain accurate results as described in the section concerned with comparisons.

Constant u-velocity panels only are laid out over part of the fuselage and designated body interference panels. The leading and trailing edges of these panels are unswept. Only the left half of the

9

aircraft configuration needs to be covered because of symmetry about the $y_B = 0$ plane provided that the effects of the other half are accounted for as discussed later. The length of fuselage covered by the body interference panels is determined by the range of influence of the wing, pylon, and store. This range is taken as the length along the body measured from the leading edge of the wing-fuselage junction, or root chord, to the trailing edge for a supersonic wing trailing edge. For the case of a subsonic trailing edge, the length should extend back further. In this case, the interference shell should be extended back as far as the axial location of the trailing edge of the wing tip. As such, the length of the body interference shell is sufficient to account for wing-pylon to fuselage interference. If the store to be separated lies close to the fuselage, the fuselage interference shell must also be long enough to cancel store effects on the fuselage. In the simplified layout of figure 1, the body interference shell consists of 5 circumferential rings with 4 panels per half ring.

Each constant u-velocity panel contains a control point placed at the 95-percent location on the chord containing the panel centroid as shown in figure 1. The flow tangency condition is applied at these points. Figure 2 shows the geometric characteristics of a panel in detail. Before specifying the boundary condition, the method of obtaining the constant u-velocity and constant source solutions for one panel will be described.

3.3.2 Constant u-velocity and constant source panel solutions

An explanation of the basic solution for the two types of trapezoidal panels is now given for completeness. The treatment is a condensed version of the one given in reference 10. However, all the equations necessary for the solutions are contained in this report.

In reference 9, Woodward, et al., derived general expressions for the solution to the wave equation for a semi-infinite triangular shape with a sweptback leading edge subject to a jump condition in axial (or u) velocity. The reference also contains the solution for the semi-infinite triangle with constant source strength. As written by Woodward, these results have a removable singularity for zero leading-edge sweep. The method of deriving these expressions is described in Appendix II, and the forms of the expressions used in the computer programs are given. The layout of the semi-infinite triangle with either a sweptback or

10

sweptforward leading edge and its relationship to the free-stream Mach cone are shown in figure 3. The sweptback case shown corresponds to a subsonic leading edge. The coordinate system associated with the triangle is also shown. Note that the x and z directions are opposite to the x_w and z_w directions shown in figure 1. The triangle lies in the $z = 0$ or planform plane. It should also be noted that the side edge lies along the x axis. The available solutions in Appendix II pertain to the sweptback triangular shape.

The solution for a constant u-velocity or constant source panel, such as the cross-hatched one shown in figure 1, is obtained through a superposition scheme using four semi-infinite triangular shapes with their apexes at each of the corners. The superposition scheme applied to the cross-hatched panel in figure 1 with sweptback leading and trailing edges on the left wing is shown in figure 4(a). The coordinate system shown in figure 4(a) is consistent with the coordinate system associated with the semi-infinite triangle of·figure 3, but the orientations of the semi-infinite triangles placed at the corner points correspond to swept-forward triangles. Thus, a transformation is used which reverses the y orientation of the triangles. The available solutions in Appendix II are then applied and the sign on the resulting sidewash is changed. If the panel leading or trailing edge is sweptforward (as on the right wing), the scheme such as that depicted in figure 4(b) for that edge must be employed in the superposition method for a trapezoidal panel on the left wing. In this case, the required solution for each semi-infinite triangle corresponds directly to the triangle with sweptback leading edge shown in figure 3 and is given in Appendix II. Trapezoidal panels may have swept-back, sweptforward, or mixed leading and trailing edges. Therefore, the superposition methods used in the computer program handle these conditions.

The superposition principle can also be used to obtain the perturbation velocities due to a constant u-velocity or constant source panel at any point in the field. Woodward, et al., in reference 9 give expressions for the velocity components due to a semi-infinite triangle with sweptback leading edge which can be used in the superposition process. The alternate forms of these expressions used in the computer program are given in Appendix II.

As described in Appendix II, the source panel strengths are directly related to the streamwise slopes of the wing and pylon thickness distributions and therefore must be specified. For blunt leading edges, a special procedure (described later) is used.

11

With the induced velocity expressions for the two types of panels known, it is possible to formulate the influence of a constant u-velocity panel of unknown strength and the influence of a constant source panel with known strength at any control point accounting for the region of influence inherent in supersonic flight. By considering interactions between all constant u-velocity panels laid out on the wing, pylon, and body interference shell, there results a set of simultaneous equations from which the unknown constant u-velocity panel strengths can be determined. This formulation will now be discussed.

3.3.3 Flow tangency boundary condition

The flow tangency boundary condition states that there is no flow through the constant u-velocity panels on the wing, pylon, and interference shell at each control point. A few control points are shown in figure 1.

Velocities normal to the wing include a component of the free-stream and perturbation velocities, w_W, induced by the constant u-velocity panels distributed over the wing, pylon, and interference shell. The line sources, sinks and line doublets used to model the fuselage induce interference velocities at the control points distributed over the wing. Components of these velocities normal to the wing are also included in the wing boundary condition. In this way, fuselage-to-wing interference is accounted for. Furthermore, the influence of the store body model is included in the wing boundary condition. Lastly, the effects of the source panels laid out on the pylon are added to the wing boundary condition to account for pylon thickness interference on the wing. The velocities induced by the fuselage and store sources, sinks, and doublets and wing thickness are designated externally induced interference down-wash w_{W_i}. Let ν be the control point index for the constant u-velocity panels on the wing and let n be the summation index for all the influencing constant u-velocity panels. The boundary condition applied at control points on the wing is then given in terms of the wing coordinate system (x_W, y_W, z_W) shown in figure 1 as follows

$$\sum_{n=1}^{NPTOT} \frac{w_{W_{\nu,n}}}{V_\infty} = (\alpha_f + \alpha_{\ell_\nu}) - \left(\frac{u_{Wi,\nu}}{V_\infty} \alpha_{\ell_\nu} + \frac{w_{Wi,\nu}}{V_\infty} \right) \tag{9}$$

$$\nu = 1, 2, \ldots NPANLS$$

12

where NPTOT is the sum of the number of constant u-velocity panels on the wing, pylon, and fuselage interference shell. The number of such panels on the wing is NPANLS. Angle α_f is the nondimensional upwash due to the free stream at the wing chordal plane and angle α_ℓ is the local angle of attack due to wing camber and/or twist as shown in the following sketch.
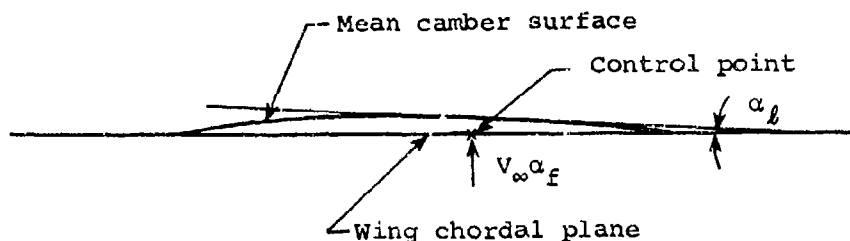
The boundary condition on the pylon states that the net velocity through the constant u-velocity panels at their control points equals zero. Velocities normal to the pylon include perturbation velocities v induced by the constant u-velocity panels distributed over the wing, pylon, and interference shell. Components of perturbation velocities induced by the line sources, sinks and line doublets representing the fuselage are included. Thus, fuselage-to-pylon interference is accounted for. Effects of the store line sources, sinks and line doublets are also included. The pylon boundary condition also contains contributions from the source panels on the wing accounting for wing thickness interference on the pylon. The last three contributions to sidewash added together are called externally induced sidewash v_{Wi}. Taking ν as the index of the control point on the pylon and n as the index of the influencing panels, the boundary condition is expressed as

$$ -\sum_{n=1}^{NPTOT} \frac{v_{W_{\nu,n}}}{V_\infty} = \frac{v_{Wi,\nu}}{V_\infty} \tag{10} $$

$$ \nu = \text{NPANLS+1, NPANLS+2, ..., NPANLS+MP} $$

This condition is also expressed in the wing coordinate system of figure 1. The number of constant u-velocity panels distributed on the pylon is MP. The right-hand side of equation (9) represents the free-stream component and externally induced perturbation downwash and the right-hand side of equation (10) represents externally induced perturbation sidewash.

13

Similarly, letting $v_{N_\nu,n}$ be the perturbation velocity in the direction normal to the νth body interference panel, the flow tangency condition states that the net velocity normal to the body interference panel is zero.

$$\sum_{n=1}^{NPTOT} \frac{v_{N_{\nu,n}}}{V_\infty} = \left(\frac{w_{Wi,\nu}}{V_\infty} \cos \phi_\mu - \frac{v_{Wi,\nu}}{V_\infty} \sin \phi_\mu \right) \tag{11}$$

$$\nu = NPANLS+MP+1, NPANLS+MP+2, \dots NPTOT$$

$$\mu = \nu - NPANLS - MP$$

The right-hand side of the above equation represents the externally induced perturbation velocity normal to the body interference panel under consideration. It contains interference velocities induced by source panels laid out on the wing and the pylon to model thickness. Store line sources, sinks and line doublet effects are also included. In this way, interference on the fuselage due to wing-pylon thickness and store body are accounted for. Angle ϕ_μ is called the body panel orientation angle measured relative to a plane parallel to the (x_B, y_B) or (x_W, y_W) plane as indicated in the following sketch looking in the positive x_B direction. The angle ϕ_μ shown in the sketch is a negative angle. The summation on the left-hand side of equation (9)
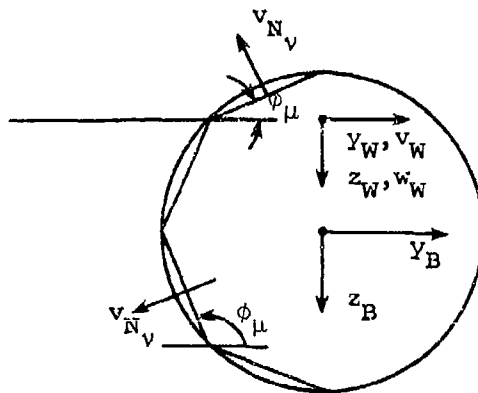
represents the downwash perturbation velocity at the control points on the wing induced by the constant u-velocity panels on the wing, pylon, and interference shell. The summation on the left-hand side of equation (10) represents the sidewash perturbation velocity at the control

points on the pylon induced by all the constant u-velocity panels.
Finally, the summation on the left-hand side of equation (11) represents
the perturbation velocity normal to the interference panel under consid-
eration induced by all constant u-velocity panels. So far, the strengths
of these panels are still unknown.

In the boundary conditions formulated above, advantage is taken of
the fact that the $y_B = 0$ or $y_W = 0$ plane is a plane of symmetry. Panels
are laid out over the left wing and pylon and only the left half of the
fuselage is covered with interference panels. Perturbation velocities
on both sides of equations (9), (10), and (11) are induced not only by
the panels to the left of the symmetry plane but also should contain
contributions from the right half. The required procedure is discussed
below in connection with the aerodynamic influence coefficients.

Next, it will be shown how the perturbation velocities are expressed
in terms of aerodynamic influence coefficients. These coefficients
relate the perturbation velocity components induced at some point by a
constant u-velocity panel to its strength u_+/V_∞ and the coordinates of
the point relative to the panel corners. A similar procedure relates the
perturbation velocities at a field point to the known strength of a source
panel.

3.3.4 Aerodynamic influence coefficients

Appendix II contains the results of the theory for determining the
perturbation velocities induced by a semi-infinite triangle subject to
a constant jump condition in axial velocity. The appendix also specifies
the perturbation velocities induced by a semi-infinite triangle with a
constant strength source distribution. The results are given below in
symbolic form. In terms of the coordinate system associated with the
triangle shown in figure 3, the perturbation velocities due to a triangle
with sweptback leading edge and with constant jump in u-velocity are
expressed as follows.

$$\left.\begin{array}{l} \dfrac{u}{V_\infty} = \dfrac{1}{\pi}\left(\dfrac{u_+}{V_\infty}\right) F_u(x,y,z,\beta,\psi_{LE}) \\[2em] \dfrac{v}{V_\infty} = \dfrac{1}{\pi}\left(\dfrac{u_+}{V_\infty}\right) F_v(x,y,z,\beta,\psi_{LE}) \\[2em] \dfrac{w}{V_\infty} = \dfrac{1}{\pi}\left(\dfrac{u_+}{V_\infty}\right) F_w(x,y,z,\beta,\psi_{LE}) \end{array}\right\} \tag{12}$$

15

The quantity u_+/V_∞ is the constant strength of the singularity distributed over the triangle. In fact, it is proportional to the axial velocity u_+ in the plane of the triangle ($z = 0$). The computer program has been arranged to predict axial velocity u_+ in the zero plane and requires a very small negative value for z to produce axial velocity u_- shown in figure 3. The complete expressions for the perturbation velocities are given in Appendix II. Functions F_u, F_v, F_w are called influence functions and depend on coordinates x, y, z of the point at which the velocities are computed relative to the apex of the semi-infinite triangle shown in figure 3. The influence functions can be determined from Appendix II, equations (II-4) and (II-12), and depend on the leading-edge sweep ψ_{LE} and the factor β given in terms of the free-stream Mach number by

$$\beta = \sqrt{M_\infty^2 - 1} \tag{13}$$

Perturbation velocities induced by the semi-infinite triangle with constant source strength are related to a surface tangent, $\tan\theta$, to be discussed later, and the coordinates of the field point relative to the triangle apex. Employing the subscript t to indicate association with thickness, the perturbation velocities are expressed as

$$\left.\begin{aligned}
\frac{u_t}{V_\infty} &= \frac{\tan\theta}{\pi} F_{u_t}(x,y,z,\beta,\psi_{LE}) \\[2mm]
\frac{v_t}{V_\infty} &= \frac{\tan\theta}{\pi} F_{v_t}(x,y,z,\beta,\psi_{LE}) \\[2mm]
\frac{w_t}{V_\infty} &= \frac{\tan\theta}{\pi} F_{w_t}(x,y,z,\beta,\psi_{LE})
\end{aligned}\right\} \tag{14}$$

Functions $F_{u_t}, F_{v_t}, F_{w_t}$ are the influence functions associated with the thickness and depend on coordinates x, y, z of the field point relative to the apex of the semi-infinite triangle such as the one with sweptback leading edge shown in figure 3. These functions can be determined from Appendix II, equations (II-15) and (II-16), and depend on the leading-edge sweep ψ_{LE} and the factor β given by equation (13).

16

In order to formulate the perturbation velocities induced by a trapezoidal constant u-velocity panel, the superposition principle described earlier and depicted in figure 4 must be employed. For example, for a panel with sweptback leading and trailing edges on the left wing, the upwash at the νth control point induced by the nth constant u-velocity panel is expressed in accordance with figure 4(a) as

$$\frac{w_{\nu,n}}{V_\infty} = \frac{1}{\pi}\left(\frac{u_+}{V_\infty}\right)\left[F_{w_n}(x_{2,\nu}, -y_{2,\nu}, z_{2,\nu}, \beta, \psi_{LE}) - F_{w_n}(x_{1,\nu}, -y_{1,\nu}, z_{1,\nu}, \beta, \psi_{LE})\right.$$

$$\left. - F_{w_n}(x_{4,\nu}, -y_{4,\nu}, z_{4,\nu}, \beta, \psi_{TE}) + F_{w_n}(x_{3,\nu}, -y_{3,\nu}, z_{3,\nu}, \beta, \psi_{TE})\right] \tag{15}$$

The subscripted coordinates represent the coordinates of the control point relative to one of the four panel corner points. The numbering sequence of the corner points is kept consistent in its relation to the directions of the coordinate systems shown in figure 4. The leading-edge and trailing-edge sweep angles of the panel are designated ψ_{LE} and ψ_{TE}, respectively. They are indicated in figure 2. Here function F_w is defined in equation (12). Similar expressions can be written for u/V_∞ and $-v/V_\infty$ using F_u and F_v, respectively. Likewise, the perturbation velocities induced by a trapezoidal constant source panel are obtained by means of a superposition scheme using the solutions for four semi-infinite triangles with their apexes at each of the panel corners. The source strength for one panel is given by the surface slope of the wing or pylon thickness distribution at the panel centroid. It is expressed as the tangent of the angle θ associated with the thickness envelope as shown in the following sketch. Therefore, the upwash due to thickness


17
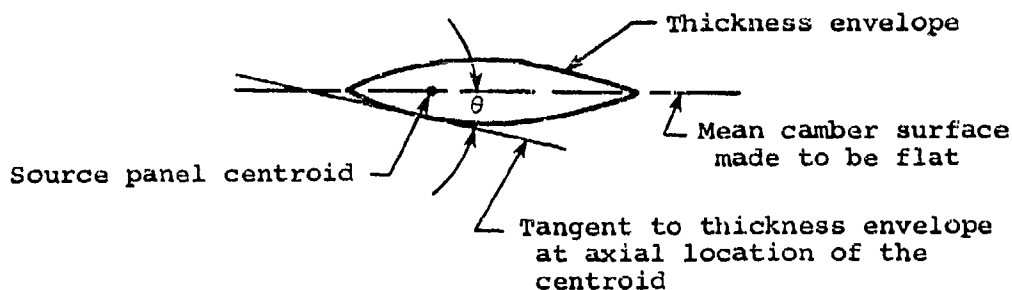
at the νth control point induced by the constant source panel with index nt on the left wing is expressed in accordance with figure 4(a) as

$$\frac{w_{t_{\nu,nt}}}{V_\infty} = \frac{\tan\theta}{\pi}\left[F_{w_t,nt}(x_{2,\nu},-y_{2,\nu},z_{2,\nu},\beta,\psi_{t_{LE}}) \right.$$

$$- F_{w_t,nt}(x_{1,\nu},-y_{1,\nu},z_{1,\nu},\beta,\psi_{t_{LE}}) - F_{w_t,nt}(x_{4,\nu},-y_{4,\nu},z_{4,\nu},\beta,\psi_{t_{TE}})$$

$$\left. + F_{w_t,nt}(x_{3,\nu},-y_{3,\nu},z_{3,\nu},\beta,\psi_{t_{TE}}) \right] \tag{16}$$

Here ψ_t pertains to the leading-edge or trailing-edge sweep of the constant source panel accounting for thickness. Note that if either the leading or trailing panel edge is sweptforward, the scheme shown in figure 4(b) must be used for the edge in question. The bracketed terms in equations (15) and (16) are designated as the upwash aerodynamic influence coefficients associated with a constant u-velocity panel and a constant source panel, respectively.

3.3.5 Symmetry considerations

In order to account for the effects of the constant u-velocity and source panels on the right half of the aircraft configuration, the perturbation velocity components induced by a panel on the left are augmented by a contribution from its image panel on the right. However, the following simplification is used. The effect of the image panel at a given point can be obtained using the panel on the left with a change in sign of the y_W or y_B coordinate of the point. The sidewash calculated this way at $P_i(x_W,-y_W,z_W)$ is then transformed back by a change in sign. The procedure is shown in the following sketch for a panel on the left wing half of a wing-alone configuration. The coordinate system

18

Image panel corresponding to panel on left wing
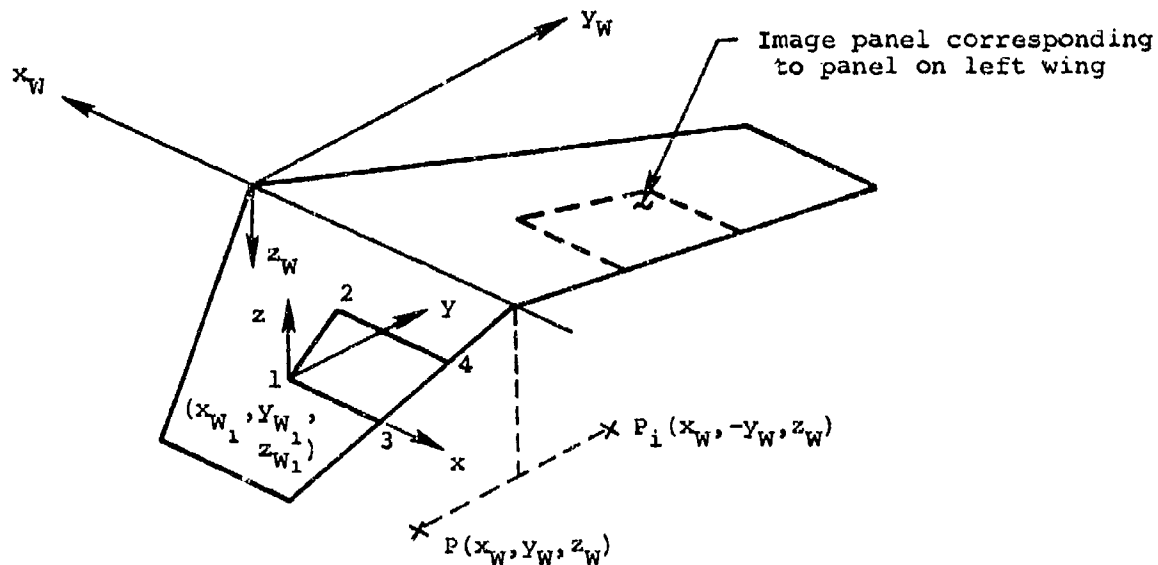
(x,y,z) associated with the semi-infinite triangle with its apex at corner 1 will be used. It is the same as the coordinate system of figure 3. The coordinates of point P relative to corner 1 $(x_{W_1}, y_{W_1}, z_{W_1})$ are then given by

$$
\left.\begin{array}{l}
x = -(x_W - x_{W_1}) \\[2mm]
y = y_W - y_{W_1} \\[2mm]
z = -(z_W - z_{W_1})
\end{array}\right\}
\tag{17}
$$

With these local coordinates, the direct influence of corner 1 at point P can be calculated. The influences of the other corners of the panel are added in accordance with the superposition scheme as indicated for the w component in equations (15) and (16). The coordinates of the point $P_i(x_W, -y_W, z_W)$ relative to corner 1 are

$$
\left.\begin{array}{l}
x = -(x_W - x_{W_1}) \\[2mm]
y = -y_W - y_{W_1} \\[2mm]
z = -(z_W - z_{W_1})
\end{array}\right\}
\tag{18}
$$

19

The influence of corner 1 is now calculated at point P_i. The influences of the other corners of the panel are added in accordance with the super-position scheme. The resulting velocity components u, v, w represent the influence of the panel on the left wing-half on the point P_i. With a change in the sign of the sidewash v, they also represent the influence of the image panel on the point P. Thus, at a given point P there will be a direct influence induced by a constant u-velocity or constant source panel and an indirect effect induced by the image of the panel under consideration.

This method of accounting for symmetry is also applied to constant u-velocity and constant source panels on a wing-mounted pylon and the constant u-velocity panels on the interference shell. The influence functions required in expressions (15) and (16) and defined by equations (12) and (14) for these panels are obtained from Appendix II, equations (II-4), (II-12) and equations (II-15), (II-16), using suitable transformations. For the pylon, a 90° counterclockwise rotation about the x-axis (viewing upstream) places the semi-infinite triangles in the vertical plane and the influence functions can be determined. The super-position scheme gives the solution for a trapezoidal panel on the pylon. Effects of the image wing-mounted pylon panel are obtained in the manner described above for a panel on the wing. The same procedure is applied to the pylon source panels. The influence functions associated with a body interference panel are also obtained after performing a rotation about the x-axis. The angle of rotation is different for each panel and is related to the body orientation angle ϕ_μ mentioned earlier in connection with the boundary conditions. Image panel effects are accounted for using the same procedure as used for a panel on the wing.

The terms on both sides of equations (9), (10), and (11) can now be specified. Equation (15) for w/V_∞ and a similar expression for $-v/V_\infty$ are used on the left-hand sides. A combination of the two components is required in equation (11). On the right-hand side, the contributions from the fuselage line sources, sinks and line doublets are given by equations (I-30) in Appendix I. Store effects are given by the same equations but require a translation of coordinate axes. Wing and pylon source panel effects are given by equation (16) for w_t/V_∞ with similar expressions for u_t/V_∞ and $-v_t/V_\infty$. Because of the difference in coordinate systems shown in figures 1 and 3, the following transformation is required to obtain the perturbation velocities in the wing coordinate system.

20

$$u_{t_W} = -u_t$$
$$v_{t_W} = v_t$$
$$w_{t_W} = -w_t$$
$$(19)$$

Perturbation velocities associated with the constant u-velocity panels must also be transformed as follows into the wing coordinate system.

$$u_W = -u$$
$$v_W = v$$
$$w_W = -w$$
$$(20)$$

3.3.6 Solution of constant u-velocity panel strengths

After recasting the perturbation velocities on both sides of equations (9), (10), and (11) in terms of the influence functions specified by equations (12) and (14) accounting for symmetry and the transformations in equations (19) and (20), there results a set of simultaneous equations in which the unknowns are the NPTOT values of panel strengths u_+/V_∞. The values can be obtained through a matrix solution for given angle of attack, α_f, and Mach number, M_∞.

3.4 Flow Field Calculation Including the Effects of the Shock Associated with the Wing Leading Edge

The method used to calculate the flow field below the wing plane of the parent aircraft is discussed in this section. The flow models representing the wing, pylon, and fuselage in supersonic flow are based on linear, potential flow theory and are described in the preceding sections. In order to predict the flow field in the vicinity of the airframe with some degree of accuracy, the linear flow theory must be augmented by nonlinear corrections. In linear theory, all disturbances travel and attenuate along Mach waves in the two-dimensional case or Mach cones in the three-dimensional case. For infinitely small disturbances, the description of the flow field and weak shock waves by linear theory is sufficiently accurate. However, when the disturbances are large, they will travel along curved characteristics in accordance with nonlinear

21

theory. Detached and/or attached shocks associated with the fuselage nose and wing leading edge will not lie along Mach lines or Mach cones.

In this work, a simplified method is used to position the wing leading-edge shock only. The technique is based on the assumption that the shock pattern from the leading edge depends on wing thickness only. For nonzero angle of attack, the shock pattern is assumed to rotate with the wing. This assumption is based on experimental evidence discussed later in the comparisons.

For a wing with either a blunt or sharp leading edge, the flow field due to wing thickness only is computed along a traverse parallel to the wing chord at the required y_W, z_W location. The flow properties at the location where wing effects due to thickness are first felt are used to determine a local Mach number. The flow properties due to wing thickness along the traverse are then recalculated with the local Mach number. The location where wing thickness effects are now felt first is taken as the location of the shock. This procedure does not depend on the wing leading edges being subsonic or supersonic. The procedure used to determine the flow field induced by the entire airframe will now be summarized. A detailed description is given in the next section. The effects of wing thickness and lift are computed at the field point in question on the basis of the local Mach number. The contribution from the interference shell is also calculated using the local Mach number. Velocities induced by the fuselage sources, sinks and doublets are still calculated using the free-stream Mach number. If a pylon is present, its effects are also based on the free-stream Mach number.

3.4.1 Flow angle and local Mach number calculation

Consider the basic airframe configuration comprised of a wing with thickness attached to a fuselage. The first step is to solve for the singularity strengths representing this configuration in accordance with the methods based on linear theory described earlier for the flight conditions at hand. The result is a complete flow model made up of line sources, sinks and line doublets to model the fuselage and constant u-velocity panels to model the lifting wing and wing-fuselage interference. There will also be source panels to account for wing thickness. The strengths of all the singularities are known at this point and the complete flow model is based on linear, potential flow theory. Special care must be exercised when assigning values to the strengths of the wing source panels as described next.

22

The strength of each source panel is directly related to the slope, tan θ, of the wing thickness envelope evaluated at the panel centroid. For wings with supersonic, sharp leading edges for which the shock remains attached, the magnitudes of the slopes at the leading edge are bounded. Figure 4 in reference 11 contains a curve relating the minimum Mach number to wedge angle for the shock to be attached. Since the leading edge of the wing is supersonic, the pertinent Mach number and wedge angle are defined in the direction perpendicular to the wing leading edge. They are related to the streamwise properties as follows.

$$
\left.
\begin{array}{l}
M_N = M_\infty \cos \psi_{WLE} \\[2ex]
\theta_N = \tan^{-1} \left(\dfrac{\tan \theta}{\cos \psi_{WLE}} \right)
\end{array}
\right\}
\tag{21}
$$

Here ψ_{WLE} is the sweep angle of the wing leading edge. If for the given free-stream Mach number and wing thickness slope at the leading edge the shock is detached, the procedure described below is used. This procedure is also used for all wings with supersonic, blunt leading edges and involves certain concepts from normal shock analysis summarized in Appendix III. The maximum slope input in the computer program is related to the shock detachment wedge angle, δ_{det}. This angle, δ_{det}, is the semi-vertex angle of a wedge for which the shock first detaches for a given Mach number normal to the leading edge. Appendix III contains a graph based on chart 2 of reference 11 from which δ_{det} can be deduced. The maximum slope $\tan \theta_{max}$ in the streamwise direction is then given by

$$
\tan \theta_{max} = (\tan \delta_{det}) \cos \psi_{WLE}
\tag{22}
$$

If for a given wing the thickness slope of one of the forward source panels is larger than $\tan \theta_{max}$, the slope is set equal to $\tan \theta_{max}$ in the input data.

The case of the subsonic leading edge will now be discussed. In this case, the flow in the direction normal to the wing leading edge is subsonic. Considering only linear theory, there is a limiting Mach cone (based on free-stream Mach number) with its origin at the leading edge of the wing-fuselage junction as shown in the following sketch. On the basis of a local Mach number discussed later, the linear theory is

23

Nonlinear Mach cones

Shock

M_N M_∞

$M_\infty > 1$

$M_N < 1$

Limiting Mach cone
based on M_∞

Linear Mach
cones

Fuselage
center-
line
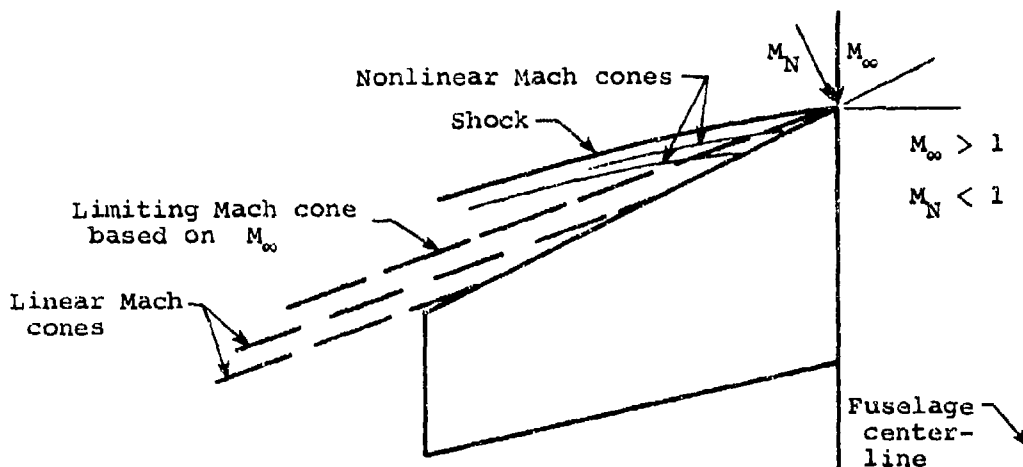
corrected. The corrected theory predicts nonzero influences ahead of the
limiting Mach wave. Thus, in a nonlinear sense, a shock shape is gene-
rated which lies in front of the limiting Mach cone. In fact, this shock
is the envelope of many nonlinear Mach "cones."

If the subsonic leading edge of a wing is sharp, the maximum stream-
wise slope, $\tan \theta_{max}$, is the value at the leading edge. If the leading
edge is blunt, the thickness slopes input into the computer program must
be bounded. Since the Mach number normal to the leading edge is sub-
sonic, the method given above for the supersonic leading edge is no
longer valid. However, assuming that the shock originates at or near
the leading edge of the wing-fuselage junction, an approach analogous
to the one used for the supersonic leading-edge case is employed. The
supersonic flow runs parallel to the fuselage as it approaches the
leading edge of the wing-fuselage junction. The shock detachment angle,
δ_{det}, is determined for the streamwise Mach number, and the maximum
slope, $\tan \theta_{max}$, is then taken equal to $\tan \delta_{det}$ directly. Away from
the junction, this upper bound is retained for all spanwise locations.
If for a given blunt wing with a subsonic leading edge the streamwise
thickness slope of one of the forward source panels is larger than
$\tan \theta_{max}$, the slope is set equal to $\tan \theta_{max}$.

For a given field point (x_W, y_W, z_W) under the wing at which the flow
field is to be calculated, an axial traverse is laid out parallel to the
fuselage centerline (and therefore parallel to the wing plane). In the
crossflow plane, the lateral coordinates of the traverse are (y_W, z_W)
associated with the field point under consideration. For the purpose of

24

calculating the local Mach number, the length of the traverse is chosen
to be from the axial location of the leading edge of the wing-fuselage
junction (or wing root chord) to the axial location of the trailing edge
of the local wing chord. The local wing chord is the chord which has
the lateral coordinates $(y_W, 0)$ in the crossflow plane. For a sharp or
blunt wing with either a subsonic or supersonic leading edge, the flow
field due to wing thickness only is computed at points along the traverse
from its starting point to its end by means of the linear theory method
described in an earlier section. For example, the upwash due to one
source panel is given by equation (16). All three velocity components
due to wing thickness are then obtained by summing the effects of all
the source panels laid out over the left wing and their images on the
right wing.

Once the perturbation velocities due to wing thickness only have
been calculated along the traverse, the point on the traverse at which
the effects are first felt is isolated. This point corresponds to the
intersection of the traverse with a Mach cone based on free-stream Mach
number and with its origin at one corner of a source panel. This corner
lies on the leading edge and inboard of the traverse for a sweptback wing
leading edge. The situation is depicted below in side view.
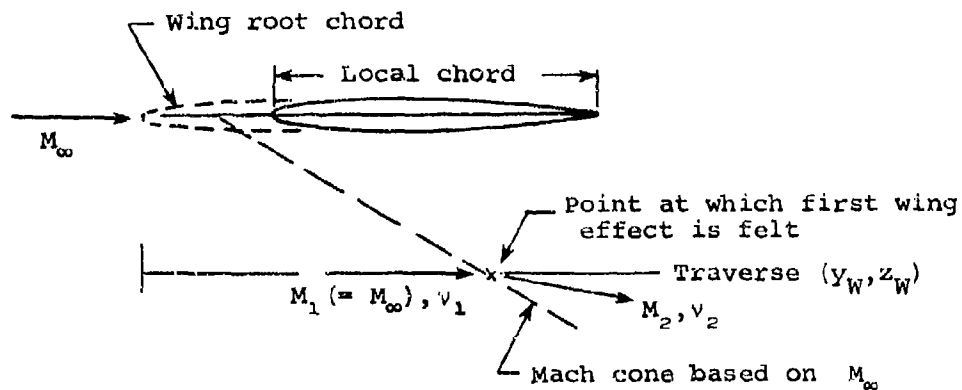
The change in flow angle, $\Delta \nu$, is determined at the point on the
traverse where wing thickness influence is first felt. The quantity
$\Delta \nu$ can be calculated from the velocity components, u_W/V_∞, v_W/V_∞, and
w_W/V_∞.

25

$$\tan \Delta \nu = \frac{\sqrt{v_W^2 + w_W^2}}{U} \qquad (23)$$

Velocity component U/V_∞ is the nondimensional total velocity in the free-stream direction and v_W/V_∞ and w_W/V_∞ are the lateral perturbation velocities in the wing coordinate system shown in figure 1. In this system, the nondimensional total axial velocity is then given by

$$\frac{U}{V_\infty} = 1 - \frac{u_W}{V_\infty} \qquad (24)$$

The change in flow angle, $\Delta \nu$, corresponds to a compression of the free-stream flow. Assuming that this compression is isentropic, the Prandtl-Meyer angle at the point where the flow is first disturbed is obtained from Prandtl-Meyer flow theory.

$$\nu_2 = \nu_1 - \Delta \nu \qquad (25)$$

Prandtl-Meyer angle ν_1 is related to the free-stream Mach number $M_\infty (= M_1)$. It is given by equation (171c) in reference 11 and repeated here for convenience.

$$\nu_1 = 2.4495 \tan^{-1}\left[0.40825 (M_1^2 - 1)^{1/2}\right] - \tan^{-1}(M_1^2 - 1)^{1/2} \qquad (26)$$

In accordance with reference 12, the Mach number associated with Prandtl-Meyer angle ν_2 can be determined most conveniently as follows in accordance with the Prandtl-Meyer relationship.

$$\left.\begin{array}{l} M_2 = \dfrac{1 + 1.3604\,p + 0.0962\,p^2 - 0.5127\,p^3}{1 - 0.6722\,p - 0.3278\,p^2} \\[2em] p = \left(\dfrac{\nu_2}{\nu_{max}}\right)^{2/3} \\[2em] \nu_{max} = \dfrac{\pi}{2}\left(\sqrt{\dfrac{\gamma + 1}{\gamma - 1}} - 1\right) = \dfrac{\pi}{2}\left(\sqrt{6} - 1\right) \quad \text{for} \quad \begin{array}{l} M = \infty \\ \gamma = 1.4 \end{array} \end{array}\right\} \qquad (27)$$

The author of reference 12 claims 0.05-percent accuracy over the entire range of Mach number ($1 < M_2 < \infty$). The component of the Mach number, M_2, in the axial or free-stream direction is then given by

26

$$M_2\Big|_{streamwise} = M_2 \cos \Delta\nu = M_\ell \qquad (28)$$

From here on, this streamwise Mach number will be designated and referred to as the local Mach number, M_ℓ.

3.4.2 Shock shape and flow field calculated on the basis of local Mach number

Under the assumption that the shape of the shock associated with the wing leading edge depends on wing thickness only, the scheme to be described next allows for the determination of the shock location. The assumption will be justified by evidence offered by comparison with experimental data which will be discussed later.

The summed effects of the source panels on the wing are computed again at points along the same axial traverse discussed previously. However, the Mach number used in this calculation is M_ℓ calculated above instead of the free-stream value. The result is a velocity component profile similar in shape to the profile obtained on the basis of the free-stream Mach number but shifted in the upstream direction. In other words, the point on the x_W traverse where the first wing thickness effects are felt now lies ahead of the point shown in the previous sketch.

Different local Mach numbers, M_ℓ, can be calculated for additional traverses parallel to the x_W traverse and located in the same y_W plane using the method described in the previous section. After recomputing the flow field due to wing thickness along the traverses with the appropriate local Mach numbers, M_ℓ, the points where the first influence is felt describe a locus which is taken as the shock shape. A typical result is indicated in the sketch below. Thus, points 1, 2, and 3 are the locations where wing thickness effects are first calculated on the basis of local Mach numbers, M_{ℓ_1}, M_{ℓ_2}, and M_{ℓ_3}, respectively. The
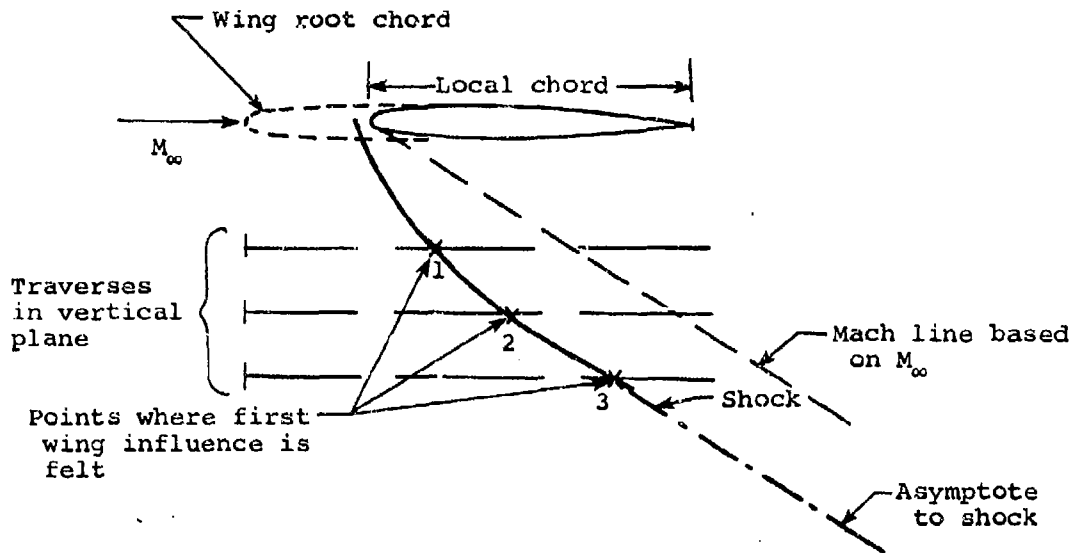
asymptote of the locus determined this way runs parallel to the Mach line based on the free-stream Mach number.

The flow field at a field point under the wing including the non-linear effects of the shock and the rest of the configuration is determined as follows. For the given field point the local Mach number, M_ℓ, is calculated based on wing thickness only for the traverse corresponding to the lateral coordinates y_W, z_W of the point in accordance with equation (28). The singularities used to flow model the entire airframe subject to the flight conditions at hand include the constant u-velocity panels on the wing, pylon (if present), and interference shell. Their strengths have been calculated based on the free-stream Mach number from the set of simultaneous equations generated by the flow tangency conditions, equations (9), (10), and (11). The strengths of the source panels used to model wing and pylon thickness are related to the streamwise thickness slopes, not Mach number. Assuming that the shock location is not altered by the effects of the constant u-velocity panels, their contribution to the flow field is then calculated on the basis of the local Mach number, M_ℓ. To this is added the effects of the wing source panels also based on M_ℓ. Finally, the contribution from the line sources, sinks and line doublets computed using the free-stream Mach number, M_∞, are added.

28

If a pylon is present and if the field point is positioned below the pylon, the contribution to the flow field from the constant u-velocity and source panels on the pylon are calculated using the free-stream Mach number. This is motivated by the evidence offered by the schlieren pictures taken during the test program. They did not show traces of shocks from the pylon leading edge extending in the downward direction even though the downwash data show significant effects. A shock can emanate from the pylon leading edge and extend on either side of the pylon but its effects are probably weak in the region below the tip of the pylon.

If flow field properties are to be calculated at a series of points along an axial traverse under the wing, all contributions except those due to the pylon are calculated using the method described above. The resulting calculated flow field may display a certain amount of scatter which is due to the discrete paneling method used. This behavior is especially pronounced when the wing has a supersonic leading edge. In this case, the major contribution to the flow field under the wing is associated with the panels directly above the traverse. Increasing the number of panels in a chordwise row reduces the amount of scatter somewhat but increases computer storage and time requirements. The axial loading distributions on a store calculated using velocity profiles with scatter are characterized by rapid oscillations with large magnitude. This is caused by the fact that the present loading calculation method is based on slender-body theory and requires rates of change with axial distance of the upwash and sidewash velocity components. These rates of change can be very large if the calculated axial profiles of the velocity components exhibit scatter and can alternate sign. In order to alleviate this problem, the calculated flow field is conditioned in the manner described next.

Over a finite length within the region of influence associated with wing thickness, a smoothing procedure is applied to the calculated flow field. First, the finite length is determined. At points along the traverse under consideration, the effects of the source panels on the wing are computed on the basis of the local Mach number, M_ℓ, given by equation (28). The desired length or smoothing range is bracketed by the point immediately behind the first influence and the point immediately in front of the expansion cone associated with the trailing edge. Over the range, the velocities due to all aircraft components except the pylon

are calculated. This is the velocity field to be smoothed. The smoothing function is a cubic polynomial and the coefficients are determined by an application of the least-squares method.

Ahead of the smoothing range (in front of the predicted shock) and at points behind, the flow field is calculated in the usual manner as the sum of the effects induced by all singularities. Inside the range, the function representing the smoothed velocity profile accounts for the effects induced by the constant u-velocity on the wing and interference shell, source panels on the wing, and the line sources, sinks and line doublets modeling the fuselage. Pylon effects are then calculated separately with the free-stream Mach number and added to the smoothed profile.

The effect of the smoothing procedure is shown in figure 5(a) which shows the upwash at the one-third semispan and 1.47 inches below the wing of the configuration shown in figure 6. The upwash is calculated for 5° angle of attack and Mach number equal to 2.0 at points along the centerline of the store 0.1 inch below the attached condition. The nose of the store, $x_s = 0$, is 17.65 inches behind the fuselage nose. Behind the shock, the unsmoothed upwash (solid symbols) displays a considerable amount of scatter. The cubic polynomial is applied to the smoothing range which in this case starts at $x_s/\ell_s = 0.3$ and ends at some distance behind the store. The smoothing function produces the solid line representing the smoothed upwash over the range of interest. Figure 5(b) shows the corresponding calculated normal-force distributions. The solid symbols represent the results calculated using the upwash indicated in figure 5(a) by the solid symbols. The result obtained with the smoothed upwash profile is given by the solid line. The former is seen to oscillate wildly. The latter generates only one pronounced peak at $x_s/\ell_s = 0.275$ and removes the oscillations towards the aft end of the store.

4. STORE FORCE, MOMENT, AND TRAJECTORY CALCULATION METHODS

The methods and equations used to calculate the aerodynamic forces and moments acting on the separated store at each point in its trajectory are unchanged from those presented in section 5 of reference 2. The only changes to the discussion presented there are with regard to the calculation of the perturbation velocity field and the flow separation

location. Also, all references made in that discussion to incompressible and compressible velocities or planes should be disregarded in the application of the loading calculation methods to this work.

In order to calculate forces and moments acting on a store during its trajectory, the nonuniform velocity field in which the store is immersed must be determined at each point in time. The velocity distribution along the body axis is required for the purpose of calculating forces and moments acting on the body. The method used to calculate the flow field is described in the preceding section. In calculating the velocity field for the case of a store released from under the fuselage, the procedure used is the same as for the under-wing case. All airframe components are accounted for in contrast with the corresponding procedure described in section 5 of reference 2. If an empennage is present, the velocities also need to be calculated at points on the tail fin surfaces for the empennage force and moment calculation.

In this supersonic store trajectory program, the store force and moment methods are still based on slender-body theory. As will be seen later, slender-body theory is not sufficiently accurate for calculating loading distributions on stores in supersonic nonuniform flow fields under the wing even though the overall forces and moments are predicted fairly well. The loading calculation methods presently implemented in the computer program can be upgraded by means of a three-dimensional calculation method. Such a refined method was developed during the subsonic work and improved certain subsonic results appreciably. It is described in detail in Appendix III of reference 2.

The computer program contains an input for the axial location along the store where boundary-layer separation occurs. For the subsonic work, it is based on empirically obtained correlations performed on bodies of revolution at low Mach numbers. As such, equation (50) in reference 2 is no longer valid for the supersonic speed regime of this work and should be updated as the program is developed further.

The method used to compute empennage forces is unchanged. It is based on slender-body theory with a correction for aspect ratio and includes an application of reverse-flow theorems. If a shock intersects the empennage, strong chordwise variations in the flow field can occur. The present method may need to be upgraded to a three-dimensional lifting-surface method to handle such a situation. In most cases, the empennage is not subjected to such a flow field.

31

The trajectory is calculated using the six-degree-of-freedom equations of motion used in the subsonic work. The underlying theory is given in full detail in section 6 and Appendix II of reference 2.

5. COMPARISONS WITH EXPERIMENTAL DATA

This section will present comparisons between results predicted with the present computer program and experimental data. The comparisons serve to assess the accuracy of the supersonic flow models as well as the flow field and loading calculation methods described in sections 3 and 4 of this report.

Comparisons are made with flow field data, store body load distributions, and store body forces and moments. The aircraft configuration consists of a wing-fuselage combination with and without a pylon attached.

5.1 Wind-Tunnel Model Description

For the purpose of providing systematic data with which to assess the accuracy of the present theory, a wind-tunnel test program was conducted in the supersonic Tunnel A at the Arnold Engineering Development Center. The basic model used in the supersonic tests was also used in the subsonic work reported in references 1, 2, and 5. This model is shown in figure 6(a). For some of the test results reported here a pylon was attached to either the wing or fuselage. Figure 6(b) shows the double-wedge shape of the pylons. One pylon could be attached to the lower wing surface at the one-third or two-third semispan position and another could be attached to the bottom of the fuselage. On the wing, the pylon centerline is at 40.0 percent of the wing chord. Below the fuselage, the pylon leading edge is 18.1 inches behind the fuselage nose.

The store used in the test program is shown in figure 6(c). The version of the store used in the majority of the tests was without the cruciform tail fins shown in the figure. The pressure distribution model does not have cruciform tail fins but is instrumented with 19 pressure orifices equally spaced in a meridian plane over the length of the store body. By rolling the model through 360°, a complete pressure distribution was obtained. The load distributions were then determined by a numerical integration of the pressures.

Some flow field comparisons will be shown which are associated with a sharp-edged trapezoidal wing attached to an axisymmetric fuselage above the midwing position. This model is described in reference 13.

32

5.2 Shock Shapes

In the section concerned with the flow field calculation method, it is mentioned that linear theory by itself does not account for shock strength, location, and curvature. However, in the same section a method is described which can be viewed as partially accounting for these shock phenomena in calculating supersonic flow fields under the wing. As a first test of the method, the predicted locus of points where effects of the wing are first felt (on the basis of the calculated local Mach number, M_ℓ) can be compared with the shape deduced from the experimental data.

Comparisons between predicted shock shapes and the shock shapes obtained from the flow field measurements are shown in figure 7 for free-stream Mach numbers of 1.5, 2.0, and 2.5. Data and predicted results are plotted for the one-third semispan location under the wing. A Mach line is shown which is based on the free-stream Mach number and drawn from the leading edge of the local wing chord. The experimental data and the pre-dicted shock shapes are seen to be displaced forward from the Mach line. All predictions generated by the present computer program are designated present method. For all Mach numbers the left wing is covered with a constant u-velocity panel layout consisting of 8 chordwise rows with 12 panels in each row. In addition, there are 8 chordwise rows with 20 source panels in each row to account for thickness. The maximum values used for the thickness slope are determined as described in section 3.4.1, and the results are $\tan \theta_{max} = 0.209$, 0.084, and 0.186 for $M_\infty = 1.5$, 2.0, and 2.5, respectively. On the fuselage, the interference shell is laid out over the length of the wing-fuselage junction and is covered over its left half with 12 half rings each with 4 constant u-velocity panels above and below the wing-fuselage junction. The fuselage is modeled by 53 line sources, sinks and line doublets. The coordinates (x_B, z_B) shown in figure 7 correspond to the fuselage coordinate system of figure 1 with the origin at the nose tip.

The experimentally obtained points correspond to the axial location of the data point immediately after the first peak in the measured flow fields. Some of the flow fields are shown in the next section. Two sets of points are plotted, one set for zero angle of attack and the other for 5°. It is seen that the shock location is not influenced greatly by angle of attack effects. This fact is used as an assumption

33

in the prediction method for calculating flow fields under the wing. Note that the wing features a blunt leading edge for all three cases considered here.

Figure 7(a) for $M_\infty = 1.5$ corresponds to an almost sonic wing leading edge (component of M_∞ normal to the edge is about 1). The shock appears to stand ahead of the local wing chord shown at the top of the figure. In fact, the shock originates at the leading edge of the wing-fuselage junction for this case. A slight dependence on angle of attack is indicated. The predicted shock shape indicated by the solid line matches the shock shape obtained from experiment well.

The case for $M_\infty = 2$ is shown in figure 7(b) and corresponds to a supersonic wing leading edge (component of M_∞ normal to the edge is greater than 1). Except for the data point at the lowest position ($z_B = 4.37$ inches), the experimental shock shapes for $\alpha_f = 0°$ and $5°$ coincide. The present method predicts a shock shape which lies slightly aft of the experimental one. The agreement is considered good. An additional theoretical curve is given by the dashed line. It represents a hybrid shock-shape calculation approach described in Appendix III. In short, this calculation combines a simple concept and curve fitting procedure of Love described in reference 14 with input for shock standoff distance generated by the numerical approach of Rizzi discussed in reference 15. The hybrid theory indicates a shock shape slightly ahead of the experimental one and definitely ahead of the shape predicted by the present method. As an approximate indication of the difference between pure linear theory and the present method, the Mach line based on M_∞ and with its origin on the wing leading edge is shown.

Figure 7(c) shows the same set of results for $M_\infty = 2.5$. The leading edge of the wing is supersonic again, and the shock has greater sweepback than that for the $M_\infty = 2$ results. This trend is also indicated by the prediction from the present method. For this flow condition the present method is represented by the solid line on the figure faired through five calculation points, the highest of which is at $z_B = 1.37$ inches. As it stands, agreement with experiment is good and the result from the hybrid theory now lies behind the data and the present method. The shock shape indicated by experiment shows a small effect due to angle of attack.

34

5.3 Flow Fields

The capability of the present method for predicting shock shapes in the vertical plane is discussed above. It remains to be seen how well the present method can predict the flow field accounting for the nonlinear shock behavior. To assess this, extensive comparisons with experimental flow field data from the test program will be shown. The wind-tunnel model is the wing-fuselage combination of figure 6(a). The effects of the pylon, shown in figure 6(b), will also be discussed. Comparison with data from a configuration equipped with a sharp leading-edge wing is also shown. All predictions shown are based on the same panel layout used for the determination of the shock shape as discussed previously including the specification for maximum thickness slope. When a pylon is attached, a layout of 2 chordwise rows with 4 constant u-velocity panels in each row is used. To model thickness, the source panel layout on the pylon consists of 2 chordwise rows with 9 panels in each row. The thickness slopes are either constant or zero. If the chordwise length of the source panels could be varied, only 3 source panels would be required to model pylon thickness. At present, the computer program allows only for equally spaced panels in the chordwise direction. Along the span, the number of source panels must equal the number of constant u-velocity panels. For this type of thickness distribution it would be advantageous to be able to specify the source panels layout independently.

5.3.1 Results for Mach number 1.5

The effects of vertical distance from the wing are shown in figures 8 through 10 for zero angle of attack and free-stream Mach number equal to 1.5. The coordinates (x_B, y_B, z_B) shown on the sets of figures pertain to the fuselage coordinate system with the origin at the nose tip as shown in figure 1. The flow field is characterized by the following set of velocity components. Backwash u is positive in the negative x_B direction. Sidewash v is positive in the inboard direction under the left wing and upwash w is positive upwards. The vertical location of the traverse and the local wing chord are indicated at the top in each figure. Wing thickness is not drawn to scale. For all vertical locations, the leading-edge shock and trailing-edge Mach cone associated with the wing are indicated by the sudden jump in magnitude of the measured backwash, sidewash, and upwash. For $z_B = 4.37$ inches (fig. 10), the trailing-edge Mach cone effect is beyond

35

the range of the traverse shown here. The present method predicts the jumps well for all vertical locations although the wing trailing-edge effect is shifted forward slightly. It is interesting to note that the upwash and to a lesser extent the backwash are still strongly felt at the lowest ($z_B = 4.37$ inches) position, figures 10(a) and 10(c), whereas the sidewash is almost completely attenuated in figure 10(b). This confirms the fact that the main effect of the shock wave is to impart a strong downward change in momentum of the flow. The present method predicts the characteristics of the flow field very well except immediately behind the shock. The theory tends to overpredict the magnitudes of the downwash immediately behind the forward jump or shock wave. According to the observations reported in reference 16, shock waves tend to soften sharp peaks in static pressure signatures when theoretical discontinuities in the slopes are indicated.

Only the sidewash and upwash velocity profiles are used in the loading calculation method based on slender-body theory mentioned in section 4. Therefore, in the following comparisons the backwash will not be shown and discussed. Generally, the agreement between theory and experiment in backwash is similar to the agreement indicated for upwash.

Figures 11, 12, and 13 show the variation of the sidewash and upwash with vertical distance for 5° angle of attack and a free-stream Mach number 1.5. The figures show the same trends as shown in figures 8, 9, and 10. As observed for the zero angle of attack case, the measured sidewash attenuates more rapidly than the measured upwash. For $z_B = 4.37$ inches, the latter has a jump in magnitude equal to about 70 percent of the jump for $z_B = 1.37$ inches. This behavior is well predicted. For the two higher locations ($z_B = 1.37$ and 2.12 inches), the present method calculates the upwash better than the sidewash. The location of the shock wave is predicted about 1/2 inch behind the location indicated by the data for $z_B = 2.12$ inches. This fact is also indicated on figure 7(a).

It is now of interest to study the capability of the present method to account for the addition of the pylon shown on figure 6(b) to the basic wing-fuselage configuration of figure 6(a). The results are shown in figure 14 for 0° angle of attack and in figure 15 for 5°. At the top of these figures, the wing local chord and pylon are indicated. Also shown are two Mach lines, based on the free-stream Mach number, extending

36

from the pylon leading and trailing edge. These lines serve to indicate the region of pylon influence, especially the onset of pylon effects. If the assumption under which pylon effects are accounted for is correct, the pylon effects should be first felt at the intersection of the forward Mach line and the traverse. The assumption refers to the region of influence of the pylon being determined by the free-stream Mach number. In both cases, the upwash is affected strongly by the addition of the sharp-edged pylon. The present method predicts the levels well although the predicted onset of pylon effect is slightly behind the experimental results for the 5° angle of attack case. It is interesting to compare these data with that obtained during the subsonic work with a pylon with shorter chord and blunt leading and trailing edges. Such data are given in figure 14 of reference 2. In comparison, the subsonic pylon effects are similar in nature but much more subdued notwithstanding the blunt edges. In general, for supersonic flow the flow features tend to be more peaked.

The pylon trailing edge is at $x_B = -22.2$ inches and for axial locations beyond $x_B = -24.5$ inches, the predicted effect of the pylon on sidewash does not occur, and the effect of the pylon washes out experimentally. This result is believed due to flow separation on the aft portion of the pylon. It was found that in this region the dominant contribution to the predicted results is generated by the constant u-velocity panels on the wing in the chordwise rows adjacent to the pylon. In particular, the aft panels were heavily influenced by the pylon source panels modeling thickness. Thus, if complete or partial flow separation occurred on the back portion of the pylon, the pylon thickness interference on the wing panels would be reduced or possibly completely cancelled. As a result, only the wing source panels would contribute and the prediction would fall on the pylon-off (dashed) line. The downwash does not appear to be influenced this way. The overall agreement between predicted and measured pylon effect on upwash is good.

For $\alpha_f = 0°$, the measured rear peak in upwash shown in figure 14(b) lies slightly aft of the predicted peak while for $\alpha_f = 5°$ the reverse is true. In this region of the flow field, the flow is accelerated for the zero angle of attack case causing the local Mach number to be higher than M_f calculated behind the shock and possibly even higher than the free-stream value, M_∞. Thus, the direct pylon effects may travel along

37

Mach lines swept back more than the ones shown at the top of the figure. The present method computes the pylon influence on the basis of free-stream Mach number, M_∞. For $\alpha_f = 5°$, the local Mach number in the region where the rear peak occurs may not be as high as M_∞ since the flow is compressed below the lifting wing. Therefore, the pylon effects may travel along Mach lines with less sweep than the lines shown at the top of figure 15(b). To account for this nonlinearity requires a further correction to the one presently employed for the wing leading-edge shock but may not be worth the additional effort it entails. Increasing the number of constant u-velocity panels on the pylon may influence the results. All results presented here are based on a total of 200 constant u-velocity panels and the present computer program is limited to 200 panels.

The effects of the pylon on the downwash under the fuselage are shown in figure 16 for 0° and 5° angle of attack. Compared to the experimental data under the wing, these data exhibit an appreciable amount of scatter especially with the pylon removed. In part, this is suspected to be due to a flat surface to which the pylon can be mounted which is recessed slightly into the curved underside of the fuselage. For $\alpha_f = 0$, agreement between present method and experiment is considered good. The measured pylon effects are of the same magnitude as for the under-wing case and are predicted well by the present method. In figure 16(b), the present method predicts the minimum value of the pylon-on upwash profile in part only but in general the agreement is considered good.

5.3.2 Results for trapezoidal wing-fuselage combination for Mach number 1.61

For the purpose of testing the capability of the present method for predicting flow fields under a sharp-edged wing, experimental data were taken from reference 13. The configuration with pertinent specifications is shown in the following sketch taken from that reference. All dimensions

38
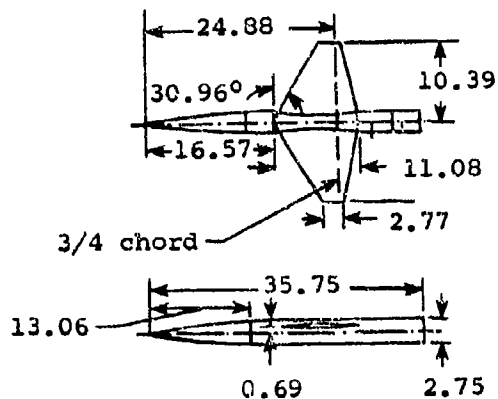
Trapezoidal Wing-Fuselage Configuration

Aspect ratio   3.0

Taper ratio   0.25

Section   4-percent circular arc

Area   1.00 square foot

shown are in inches. The plane of the wing is about one-half of the fuselage radius above the fuselage midplane.

For the free-stream Mach number of 1.61, the wing leading edge is supersonic. The maximum streamwise thickness slope occurs at the leading and trailing edges and its magnitude is 0.076. This slope corresponds to an angle of 4.36° measured in the streamwise direction. In the direction normal to the wing leading edge, equation (21) gives an angle of about 5.1°. The same equation also gives the Mach number normal to the leading edge, M_N, to be equal to 1.38. After consulting figure 4 in reference 11 or the more precise chart 2 in the same reference, the maximum wedge semi-vertex angle for an attached shock is 7.8°. Thus, the shock is attached to the wing leading edge.

Figures 17 and 18 are comparisons between the results of the present method and experimental data drawn from reference 13. The results are expressed as local upwash angle, α_ℓ, and sidewash angle, σ_ℓ. In terms of the perturbation velocities u_W, v_W, w_W in the wing coordinate system of figure 1, the angles are expressed as follows.

39

$$\alpha_\ell = \tan^{-1} \frac{-\dfrac{w_W}{V_\infty} + \sin \alpha_f}{1 - \dfrac{u_W}{V_\infty}}$$

$$\sigma_\ell = \tan^{-1} \frac{\dfrac{v_W}{V_\infty}}{1 - \dfrac{u_W}{V_\infty}}$$

(29)

At the top of both figures, the local wing chord and vertical location of the traverse are indicated. Wing thickness is not drawn to scale. Mach lines based on M_∞ are also shown to indicate approximately the linear region of influence.

The results for zero angle of attack are given in figure 17. Overall, the present method predicts the sidewash and upwash well, and the systematic differences in the neighborhood of the leading-edge shock formerly seen are exhibited here also. However, the measured shock location lies about 1/2 inch forward of the predicted shock location. The reason for this discrepancy is presently not known. The wing leading edge may not be aerodynamically sharp; that is, it may be blunt enough to cause the shock to be slightly detached. On the other hand, the calculation of the local Mach number in accordance with equation (28) can be sensitive to the spanwise number of source panels laid out on the wing. The shock location is determined by the local Mach number. The present method results are based on the same panel layout as specified in an earlier section concerned with shock shapes. Consequently, the results generated by the present method are based on 8 chordwise rows with 20 source panels in each row. A better local Mach number may result with more chordwise rows, but this has not been ascertained as yet.

Figure 18 shows the results for $\alpha_f = 4^\circ$. The trend of sidewash and upwash with angle of attack are predicted well. For example, the measured sidewash is definitely increased in the outboard direction as the angle of attack is increased to 4°. The present method also indicates this behavior. Otherwise, the same remarks made above for the zero angle of attack case apply.

40

5.3.3 Results for Mach number 2

The effects of the pylon on the flow field under the wing are shown
in figures 19 and 20 for 0° and 5° angles of attack respectively. At
the top of the figures, the local wing chord and the vertical location
of the traverse are indicated. Wing thickness is not drawn to scale.
The pylon is also outlined and free-stream Mach lines are drawn from
the leading and trailing edges of the pylon tip.

For both angles of attack, the predicted shock location lies behind
the experimentally deduced location by about 1/2 inch. With the pylon
removed, the upwash is predicted better than the sidewash. Generally,
speaking, the pylon-off velocity profiles are predicted reasonably well,
except for the measured sidewash and downwash values at the leading-edge
shock.

In comparison with the experimental data for Mach number 1.5 shown
in figure 14, the effects of the pylon, shown in figure 19, are somewhat
less pronounced for Mach number 2. The backwards shift of the location
of the shock is also evident. The present method for $\alpha_f = 0°$ predicts
these trends fairly well. An increase in sidewash due to the pylon of
about 1° is indicated by the present method at points behind $x_B = -23$
inches whereas the measurements only show a fractional increase.
Comparing the measured upwash profile of figure 14(b) for Mach number
1.5 to the profile for Mach number 2 in figure 19(b) indicates very
little shift in the location where the pylon influence is first felt.
The theory indicates a similar result. Otherwise, the remarks made in
connection with the Mach number 1.5 comparison applies here as well.

When the angle of attack is changed to 5°, the pylon exhibits loading
due to outboard sidewash induced by the lifting wing. Below the pylon,
the sidewash must then accelerate around the pylon tip in the outboard
direction. This increment in sidewash with angle of attack is indicated
by both experimental data and present method in figure 20(a). This
increment is larger than the increment shown for Mach number 1.5 in
figure 15(a). The trends shown by the upwash are predicted fairly well.
The data with the pylon on do not go back far enough to show if the pylon
effect washes out behind its trailing-edge location as a result of
separation. Such separation effects would be greatly reduced at full-
scale Reynolds number.

41

5.3.4 Results for Mach number 2.5

This is the highest Mach number for which data were taken on the
basic wing-fuselage model shown in figure 6(a). Only the pylon-off data
will be discussed. The sidewash and upwash comparisons are shown in
figure 21 for zero angle of attack, $\alpha_f = 0°$, and in figure 22 for
$\alpha_f = 5°$. At the top of the figure, the local wing chord and the vertical
location of the traverse are shown. The indicated wing thickness is not
drawn to scale. Mach lines based on free-stream Mach number, M_∞, are
drawn from the wing leading and trailing edges.

Considering the forward peak in sidewash in figures 8(b), 19(a),
and 21(a), it is interesting to note that the actual measured peak value
is almost constant for $M_\infty = 1.5$, 2.0, and 2.5. At the highest Mach number,
the measured and predicted axial location of the peak are still ahead
of the axial location of the intersection of the Mach line based on M_∞
and the traverse as would be expected and the shock wave is bent back
with increasing Mach number. The predictions generated by the present
method are based on the same panel layout specified in the section
describing the shock shapes. The maximum thickness slope for this Mach
number is $\tan \theta_{max} = 0.186$. Immediately following the shock, the
present method overestimates the magnitude of the sidewash in a way which
tends to become more pronounced as M_∞ or α_f increase. In terms of
upwash, the effect of higher Mach number is to deepen the forward peak
and to shift back the axial location of the peak as can be seen on fig-
ures 8(c), 19(b), and 21(b). This is also indicated by the present
method. For the highest Mach number, the present method overpredicts
the magnitudes of the upwash in the region immediately following the
shock. In general, the velocity profiles are predicted fairly well.

Figure 22 shows comparisons for $\alpha_f = 5°$. The magnitudes of side-
wash immediately behind the shock is overestimated by the present method.
This effect can also be discerned for the predictions of sidewash in
figures 15(a) and 20(a) for $M_\infty = 1.5$ and 2, respectively, for the pylon-
off case. In fact, the measured sidewash profiles show a systematic
change with M_∞ for reasons which are not known. The measured upwash
profile changes its shape behind the shock from a dish to a ramp. This
result is predicted by the present method as can be seen on figures 15(b),
20(b), and 22(b). For $M_\infty = 2.5$, agreement between the present method
and measurement is not so good as for the lower Mach numbers.

42

5.4 Loadings on the Store

A few comparisons between measurements and results from the present method in terms of store force distributions and overall forces and moments will now be shown. These comparisons point out the limitations associated with determining the load distribution at supersonic speeds with the present method taken from the subsonic work of reference 2 and also suggest the means for overcoming these limitations. (Nevertheless, the total forces will be seen to be good enough for preliminary design purposes.) A few pressure distributions along the length of the store body calculated by the present theory are compared with measurements for the finless store in uniform flow.

5.4.1 Force distributions along the store

The results generated by the present method are based on the panel layout and other specifications listed in an earlier section dealing with shock shapes. As formulated for use at subsonic speeds, the present method calculates store loads on the basis of slender-body theory with a two-dimensional approach for the buoyancy forces.

The side-force and normal-force distribution along the axis of the attached store are shown in figure 23 for zero angle of attack, $\alpha_f = 0^\circ$, and for free-stream Mach number 1.5. These data are obtained from the pressure distribution model by an integration of the pressures. The effect of the pylon on the measured normal-force distribution is to enlarge and slightly shift back the peaks for the pylon-off case. The side-force distribution is only slightly affected by addition of the pylon. For comparison with earlier figures, the body axis coordinate x_B is also shown in figure 23.

In connection with the side-force distribution, the calculated velocity profile from which the necessary gradients are computed is almost identical to the calculated sidewash distribution shown in figure 14(a). Apparently, the inclusion of store effects in the wing-pylon boundary condition has little effect on the sidewash. The store nose is at the location of the shock wave from the wing leading edge. The comparison between the prediction and data on the store nose illustrates the shortcoming of slender-body theory which is based on small axial gradients and as such it cannot cope with the large gradients behind the shock even though they are smoothed. The sudden change in the experimental side-force data at x_s/ℓ_s approximately equal to 0.6 is definitely a

43

flow field effect not accounted for by the present method and is thought to be an extraneous disturbance due to some unknown cause. It can also be seen in figure 14(a) at $x_B = -22.25$ inches. This effect is not caused by the pylon.

The normal-force distribution shown in figure 23(b) is strongly influenced by the pylon. From $x_s/\ell_s = 0.2$ to 0.32, both pylon-off and pylon-on experimental data show the effect of the store nose shock reflected from the wing. Beyond this range, the pylon-on data are strongly influenced by the pylon effects. For the prediction of the pylon-off case, it was found that the calculated but unsmoothed velocity profile exhibited a negative peak at $x_B = -20.3$ inches which was due to reflection of the store nose wave. This location corresponds to about $x_s/\ell_s = 0.35$ which is slightly behind the experimental negative peak. The pylon-off prediction for normal-force distribution does not show any effect of the reflected shock at $x_s/\ell_s = 0.35$. The reason for this defect is that the smoothing procedure, presently used to condition the velocity profile for use with slender-body theory, completely washes out the effects of the reflected store nose shock. It is interesting to note that the pylon-off data resemble the pylon-on data and that the net effect of the peaks results in a small force but appreciable couple contribution. After the negative peak at $x_s/\ell_s = 0.32$, the normal-force distribution rises to a positive peak and then falls back on the prediction. The store axis is located 1.47 inches below the chordal plane of the wing. Accounting for wing thickness and the store radius leaves a distance of 0.78 inch between the under surface of the wing and the store body. Compared to the local wing chord of about 7 inches, this spacing makes the store closely coupled with the wing and multiple shocks can occur between the wing and store. Certain phenomena which can take place in this region will now be examined.

Consider the following sketch. In accordance with reference 17, the parameters governing the reflection of shock waves from solid boundaries are boundary-layer character and thickness, shock strength

44
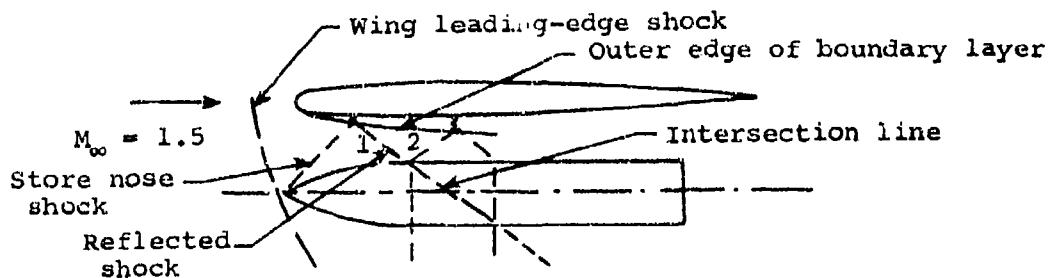
and the geometry of the three-dimensional, shock-body configuration.
Assume for now that the shock from the wing leading edge does not inter-
act with the store nose and that the boundary layer on the under-wing
surface is laminar near the leading edge. The boundary layer may then
separate at or near the point of impingement of the shock from the store
nose. This shock is then actually reflected as an expansion wave. But
the outward compression waves generated by the thickening, separation,
and the reattachment of the boundary layer on the wing tend to coalesce
with the expansion wave to form a compression shock marked 1. Shock 1
can now be considered as the store nose shock reflected from the wing.

In inviscid flow terms, as this shock impinges on the store body,
flow is induced into the upper surface of the body. Since this surface
is a solid boundary, the required cancellation (outward flow) brings
about another reflected shock 2. As the shock marked 1 intersects the
body on its way to the leeward side, the flow may leave the surface. The
cancellation of the outward component of the flow on the leeward side
causes an expansion wave to originate along the intersection line. It
can weaken shock 1 to the point where shock 1 is broken up. Viscous
effects tend to distort the flow further and in fact a very strong
boundary-layer crossflow occurs approximately in the direction of the
intersection line. The accumulation of boundary layer on the leeward
side regenerates a compression shock some distance away from the body
surface.

The crossflow boundary layer has the effect of relieving the over
pressures on the incident side by allowing it to bleed off to the leeward
side. In the absence of other shocks impinging on the body, the over
pressures fall back to the body-alone pressures within a short distance
downstream from the inpingement location. Thus, the reflected shock
definitely causes a down force on the body locally. Downstream, the
local down force should disappear and the loading distribution should
be determined by the flow field as seen by the store. The pylon-off
data shown in figure 23(b) exhibit a definite positive peak, however.
It is possible that the increasing upwash, shown in figure 14(b),
together with the downward crossflow effects discussed above, can
generate a complete reversal in the pressure field across the body.
Instead of this phenomenon or in addition to it, shock 2 can reflect
off the boundary layer on the wing. If the boundary layer is separated
due to the action of the store nose shock, shock 2 can be reflected from

45

the wing as an expansion wave towards the store body. On the incident side of the store body, under pressures are induced due to impingement of the expansion wave and a positive normal-force peak would result. The effects of the multiple shock system eventually die out over the aft portion of the store. This trend is indicated by the experimental data and the present method predicts the level of the normal-force distribution well. Thus, over the part of the store influenced by the shocks, the forces acting on the store body are dominated by the shocks.

The pylon-on data appear to be in phase with the pylon-off (multiple shock) data. The forward negative peak with the pylon on at $x_B/\ell_B = 0.37$ is believed to be caused by the pylon and is predicted well. The pylon-on prediction does not contain effects of the reflected store nose shock because of the present velocity smoothing scheme as mentioned earlier. The pronounced negative peak predicted by the present method for the pylon-on condition over the aft position of the store is due to the calculated pylon induced flow field. The calculated upwash profile shown in figure 14(b) shows a sharp positive peak at $x_B = -22.5$ inches which lies slightly ahead of the experimental one. Beyond this location, the prediction drops sharply thereby generating a very large negative gradient. Again, the magnitude of this axial gradient is not compatible with the assumptions of slender-body theory. Besides, the experimental flow field shows a less drastic drop off in upwash. Thus, the slender-body load prediction is also affected by the inaccuracy in the predicted upwash distribution.

The comparisons exhibited by this figure suggest that better account must be taken of the effect of the store nose shock reflection from the wing under surface. For stores close to the wing where a number of reflections can take place, it is difficult to obtain the necessary resolution to account for the phenomena without using very large numbers of wing constant u-velocity panels on the wing near the store. However, by using an image store technique, it is possible to account for wing reflection effects very conveniently for those cases where the store nose shock is reflected from the under-wing surface and does not pass upward in front of the leading edge. Furthermore, this technique can be combined with a three-dimensional store loading calculation method instead of the slender-body method and can be carried out independently of solving the airframe modeling problem. Accordingly, it can probably be carried out at various points in the store trajectory without using

46

excessive computer time. The refined, three-dimensional store loading
method was developed for subsonic speeds in reference 2. In general,
the same type of behavior of both prediction and measurement exist for
the other Mach numbers.

5.4.2 Store forces and moments

The forces and moments acting on the finless store of figure 6(c)
are shown in figure 24 for 5° angle of attack and Mach number 1.5.
Vertical location $\Delta z = 0$ corresponds to the attached store position.
The results shown are obtained with the present method which is based
on slender-body theory. Note that the measured side force shows a
pylon effect for the first inch of vertical distance, but the present
method does not predict this trend. Predicted side force and yawing
moment for the pylon-off case indicate the trends shown by the experi-
mental data. The normal force and pitching moment show larger influence
from the pylon than do the side force and yawing moment which is also
indicated by the present method for distances larger than 1.5 inches
below the attached position. On an overall basis, experiment and
prediction show the same trends.

The behavior for Mach number 2 is shown in figure 25. Agreement be-
tween the present method and experiment is similar to the $M_\infty = 1.5$ case
and actually slightly better for the normal force and pitching moment
except just below the attached position. The prediction at $\Delta z = 3$ inches
for the side force and yawing moment is excessive. The smoothed sidewash
velocities calculated at the rear of the store resulted in large axial
changes which in conjunction with the slender-body load calculation method
generated unrealistically high side force and yawing moment. Otherwise,
the present method indicates the measured trends.

5.4.3 Finless store in uniform flow

The purpose of the following discussion is to compare loading
distributions for the finless version of the store shown in figure 6(c)
at incidence in uniform subsonic and supersonic flow. Consider figure 26
showing the measured normal-force distribution for various angles of
attack for Mach number 2. It can be seen that considerable loading
exists on the cylindrical portion of the store. Also shown is a solid
line which is the force distribution prediction based on the slender-body
theory for 4° angle of attack. This result can be obtained from equa-
tion (46) of reference 2. The dark symbols indicate subsonic

47

experimental data taken from figure 30 in reference 2 for Mach number 0.4. The loading carryover onto the cylindrical portion appears to be more pronounced for supersonic flow than for subsonic flow. Thus, for the store in subsonic uniform flow, the calculation method based on slender-body theory is adequate. This is not the case for a store in supersonic uniform flow.

The pressure distributions along the windward and leeward meridians of the store are shown in figure 27 as a function of orifice number for 5° angle of attack and Mach number 2. The following sketch serves to relate orifice number to distance along the pressure distribution model which has the same shape and dimensions as the finless store under consideration. Orifice number 6 lies very close to the shoulder. The
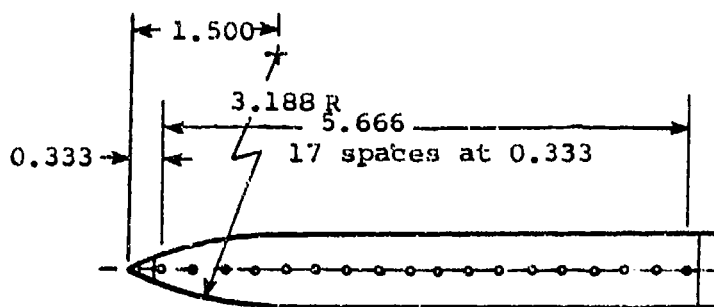
All dimensions in inches
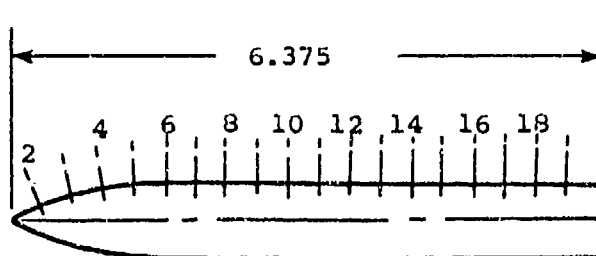
measurements show loading carryover onto the cylindrical part of the store, especially on the leeward side. Theoretical results were obtained with a special version of the axisymmetric, supersonic body modeling program and are seen to overshoot the measured pressures at the shoulder. Agreement between theory and experiment at all other locations is good. Thus, at least for the case of uniform flow, the three-dimensional flow model presently used for the fuselage and store in supersonic flow is quite capable of predicting pressures on the store surface.

48

6. CONCLUDING REMARKS

This report presents the results of an effort to extend the sub-
sonic store separation prediction method of reference 1 to supersonic
speeds. The results reported herein were obtained during a combined
theoretical/experimental research program. In order to isolate and
identify problem areas in the flow modeling and store load calculation
methods, the configurations of interest are simple ones which utilize
wings without dihedral or incidence attached to axisymmetric fuselages.
A pylon can be attached to the wing or fuselage and the wing-fuselage
junction can be located above or below the midplane. Both pylon and
wing may have thickness. As one of the results of this effort, a
computer program for this class of configurations was written with a
view towards building it up to the general capabilities of the subsonic
store separation program of reference 1.

The primary purpose of this effort was to apply linear, potential
flow modeling methods to the aircraft components and to develop methods
for predicting the flow fields in which the store would be immersed.
The existing store loading calculation methods developed in reference 2
would then be employed. Shortcomings of either the flow field or
loading calculation methods were to be determined by comparing with
experimental data. Necessary corrections to the theoretical methods
were to be made to improve agreement, especially to the flow field
calculation methods.

The flow models for the aircraft components and the methods used to
account for mutual interference between the components are based on
linear, potential theory for supersonic flow. Line sources, sinks and
line doublets are distributed along the fuselage centerline to represent
volume and angle of attack effects. A layout of constant u-velocity
panels on the wing and pylon (if present) model lift including upwash
induced by the fuselage, and an additional layout of source panels model
wing and pylon thickness effects. Wing-pylon mutual interference is
fully accounted for. Wing-to-fuselage interference is handled by constant
u-velocity panels in an interference shell placed over that part of the
fuselage influenced by the wing.

In conjunction with the analytical work, an extensive and systematic
wind-tunnel test program was carried out to provide flow field data for
checking and improving the accuracy of the flow models and the flow field

49

calculation methods. In addition, force distributions and overall force
and moment data were obtained for the store in order to assess the adequacy
at supersonic speeds of the present store load calculation methods.

After the computer program based on linear, potential flow theory
was written, it was necessary to make corrections to the method. The
corrections account for the fact that the disturbance from the wing
leading or wing root leading edge (the shock) does not coincide with the
Mach lines associated with linear theory. Also, simple shock theory was
used to develop a limit on the streamwise thickness slope permissible
with blunt leading edges. Fair to very good agreement was obtained
between experiment and prediction for flow fields. It was found necessary
to smooth the predicted flow field because the calculated flow field is
basically not smooth. The salient features of supersonic flow under the
wing and fuselage were reproduced. With a pylon attached, the flow is
influenced heavily, and the present flow calculation method predicts the
pylon effects well. The only systematic deviation occurred in the region
directly behind the shock and it became more pronounced as the free-stream
Mach number and angle of attack increased.

When the store is introduced into the flow field, additional pertur-
bations are added to the flow caused by multiple shock reflections taking
place between the store and the wing. A better method is needed to
determine the effects of this type of wing-store interference. The
present loading calculation method for the store body needs to be made
three dimensional since the axial velocity gradients occurring in the
flow are basically too large to obtain accurate results with slender-
body theory. This is in contrast with subsonic flow where flow features
are much more softened and the velocity gradients are much smaller in
magnitude. Despite its limitations regarding store loading distribu-
tions, the method predicted generally good results for total forces and
moments of the basic store. For this reason the present program can be
used for trajectory predictions.

In the following section, recommendations are described to improve
the store load calculation method and to further improve the flow field
predictions.

7. RECOMMENDATIONS

The following recommendations are made to increase the accuracy of the computer program written as part of the work performed during the present program.

7.1 Store Load Calculation Method

The present method is capable of predicting supersonic flow fields under the wing or fuselage of a basic configuration. However, the store load distribution calculation method should be improved. This can be accomplished while at the same time improving the calculation of the flow field in which the store is actually immersed by accounting better for store nose shock reflection from the wing.

A three-dimensional approach should be developed using the supersonic line sources, sinks and line doublets to compute the load distribution along the store body. Such a method was developed for the subsonic case in reference 2 and the upgraded method was successful in appreciably improving loading results predicted by the simpler, two-dimensional loading method for high angles of attack. In contrast with supersonic flow, the simpler method was sufficiently accurate in most cases encountered for subsonic flow and was therefore not implemented in the subsonic computer program. The smoothing procedure applied to the flow field in which the store is immersed can probably be eliminated if the three-dimensional approach based on imaging of the store relative to the wing is used as described below.

In addition, the three-dimensional approach should be accompanied by an upgraded buoyancy force calculation method. Buoyancy forces can be calculated on the basis of obtaining pressures (using the Bernoulli pressure/velocity relationship) at a number of points equally spaced on the body circumference in the crossflow plane without the store effects included in the flow field. The buoyancy forces can then be determined through an integration scheme.

7.2 Store-to-Aircraft Interference

The next recommendation is concerned with an improvement in the store-to-aircraft interference account. Presently, this interference is accounted for by including store effects in the flow tangency boundary condition applied at the control points of the constant u-velocity panels on the wing, pylon, and body interference shell. In order to accurately

51

model the multiple reflections of the store nose shock, a very large number of such panels must be distributed over the affected areas of the aircraft. Furthermore, it would be necessary to recalculate the singularity strengths representing the wing-pylon-fuselage as the store moves away. In the improved method the wing or the fuselage under which the store is located is treated as a reflection plane; that is, an image store is placed on the other side of the wing or inside the fuselage. As the store drops away, the singularity strengths representing the parent aircraft remain the same and the imaging system changes so that changes in the wing-store interference can be accounted for without the extensive computer time which would be required to recalculate the entire flow field at each step in the trajectory.

If the store moves longitudinally from the wing, then the imaging scheme must be modified because the wing is not infinite in extent and will act as a reflection plane only for part of the store.

7.3 Further Improvements in Flow Field Prediction Methods

As an additional improvement to the present method, it is possible to calculate the flow field with more accuracy by replacing the straight line characteristics of the linear theory with a good approximation of the exact (curved) ones. A sufficiently good approximation to the strengths of the disturbances propagated along the exact characteristics can still be determined from linear theory. It is possible to employ available theories for the purpose of relating flow properties along exact characteristics to those along approximate characteristics. Such theories are described in references 18 and 19.
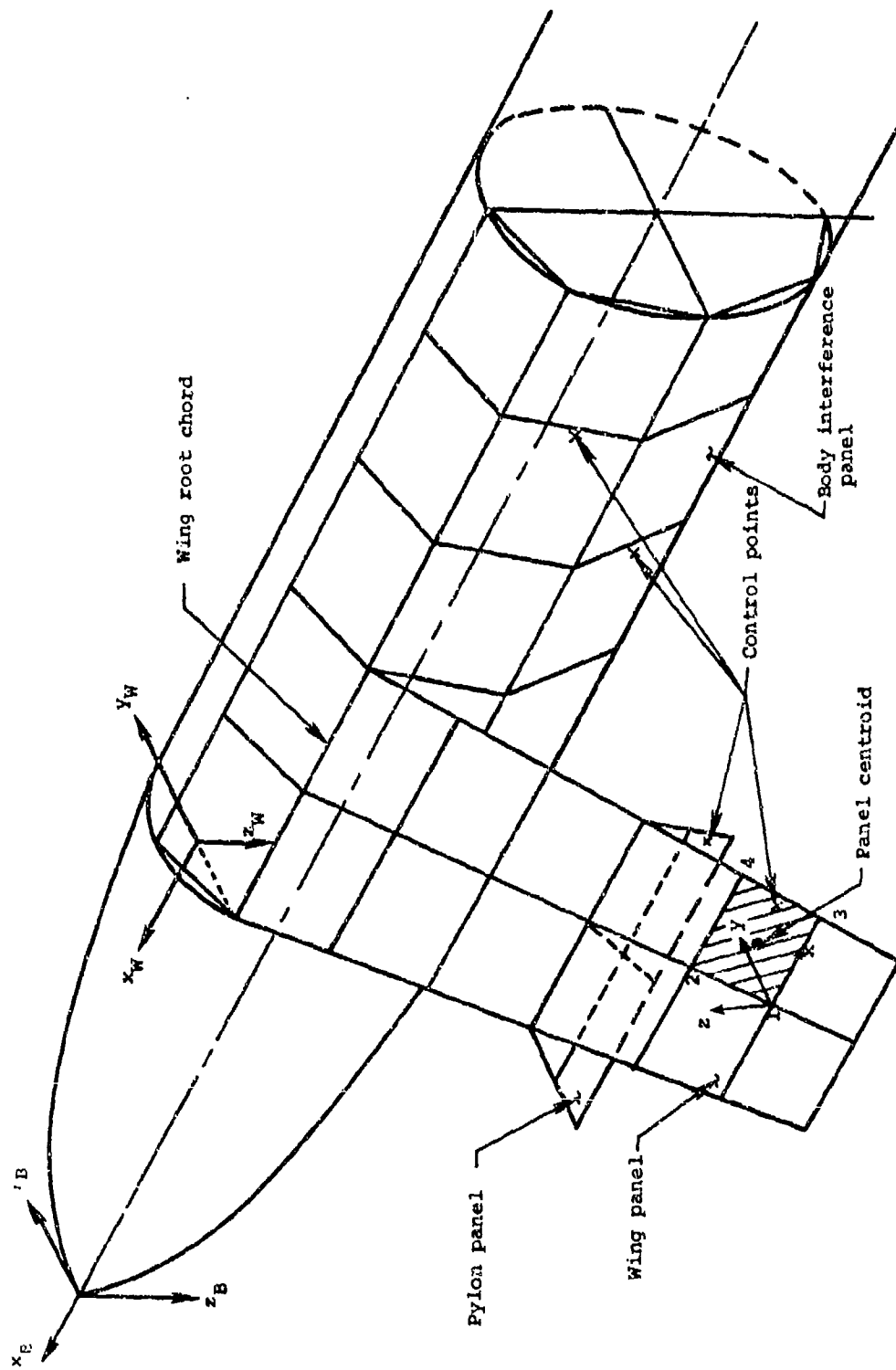
Figure 1.- Simplified layout of panels for wing-pylon-fuselage combination.

Wing root chord

Control points

Body interference panel

Panel centroid

Pylon panel

Wing panel

53
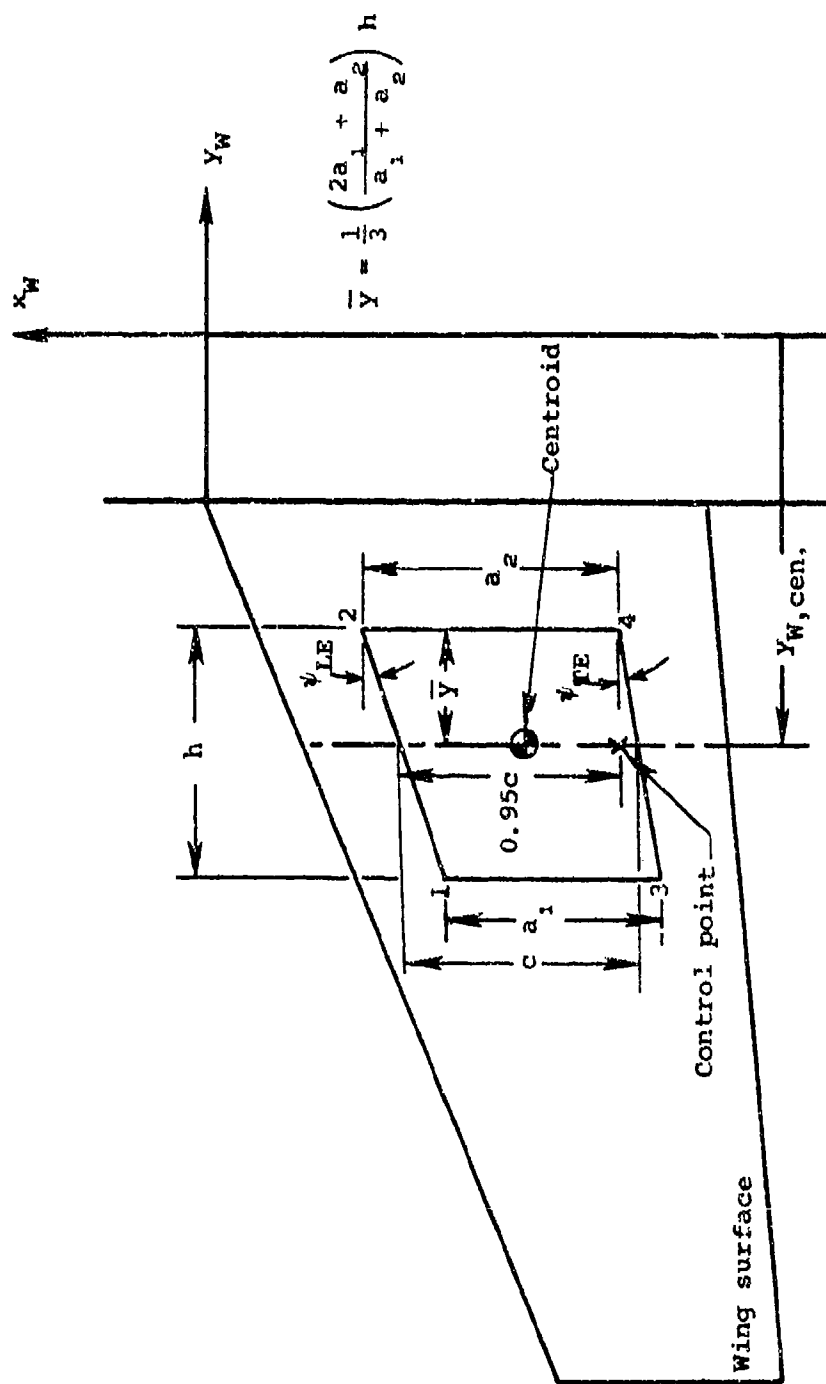
Figure 2.- Geometric characteristics of a trapezoidal panel on the wing.

54
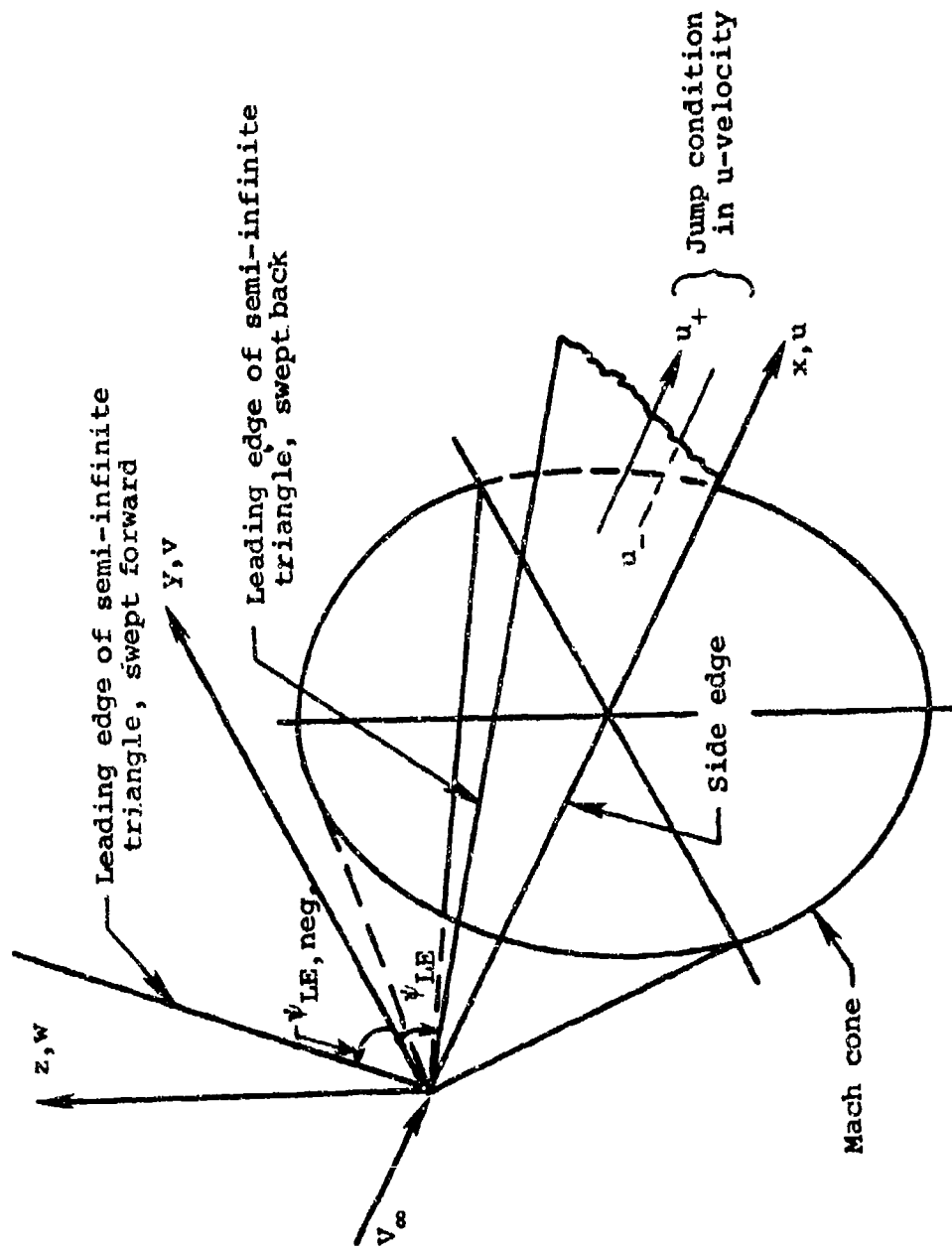
Figure 3.- Layout of semi-infinite triangular shape and associated coordinate system.
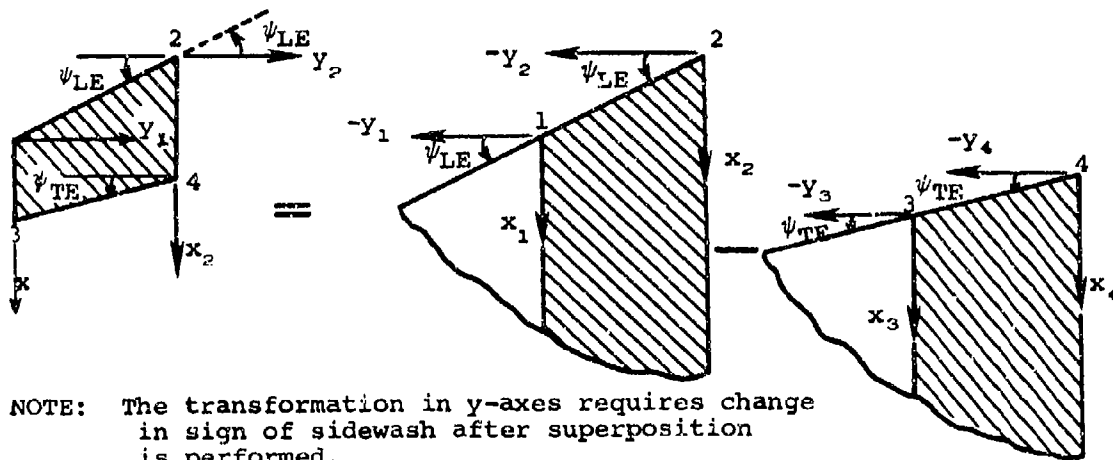
NOTE: The transformation in y-axes requires change
      in sign of sidewash after superposition
      is performed.

Trapezoidal Panel = (Triangle 2 - Triangle 1) - (Triangle 4 - Triangle 3)

(a) Panel with swept back leading and trailing edges on left wing.
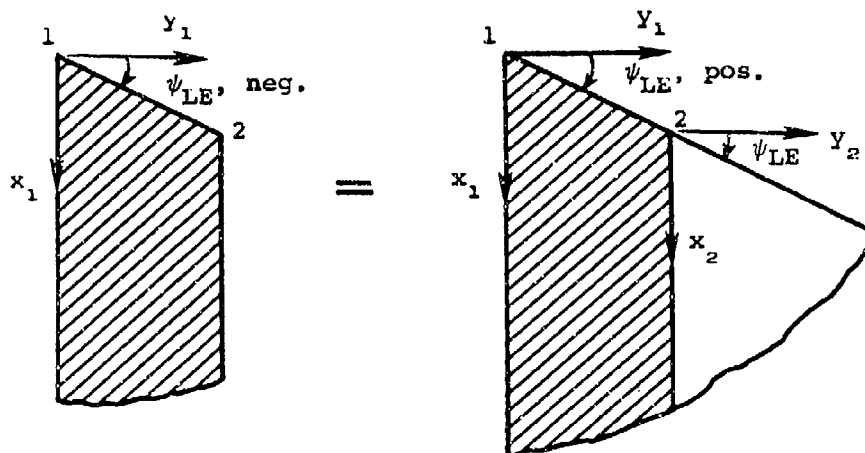
Strip with Swept Back Leading Edge = (Triangle 1 - Triangle 2).

(b) Panel edge with forward sweep for panel on left wing.

Figure 4.- Superposition scheme for panels on the left wing.

56
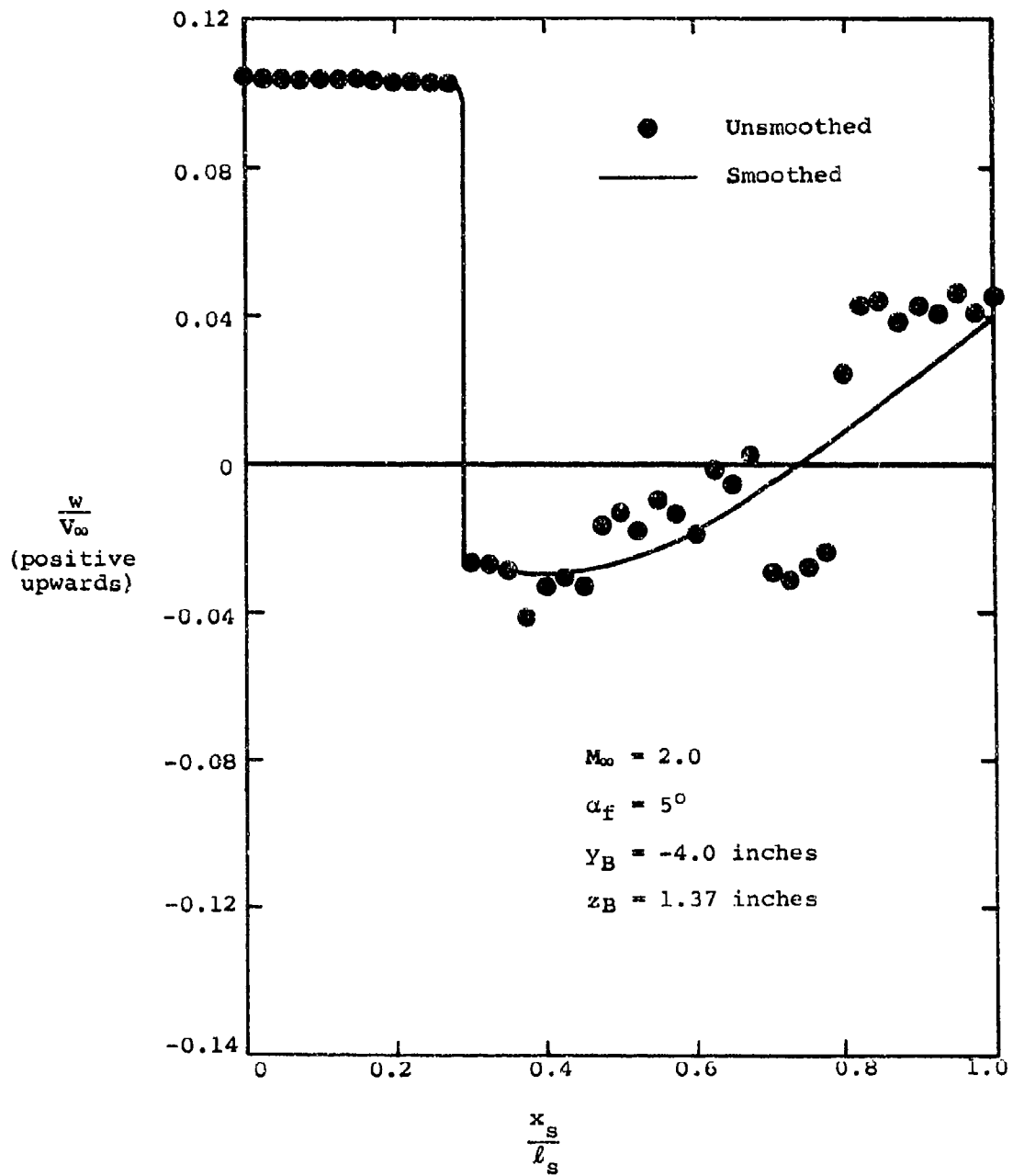
(a) Upwash.

Figure 5.- Effect of smoothing procedure on the upwash and loading distribution.

57
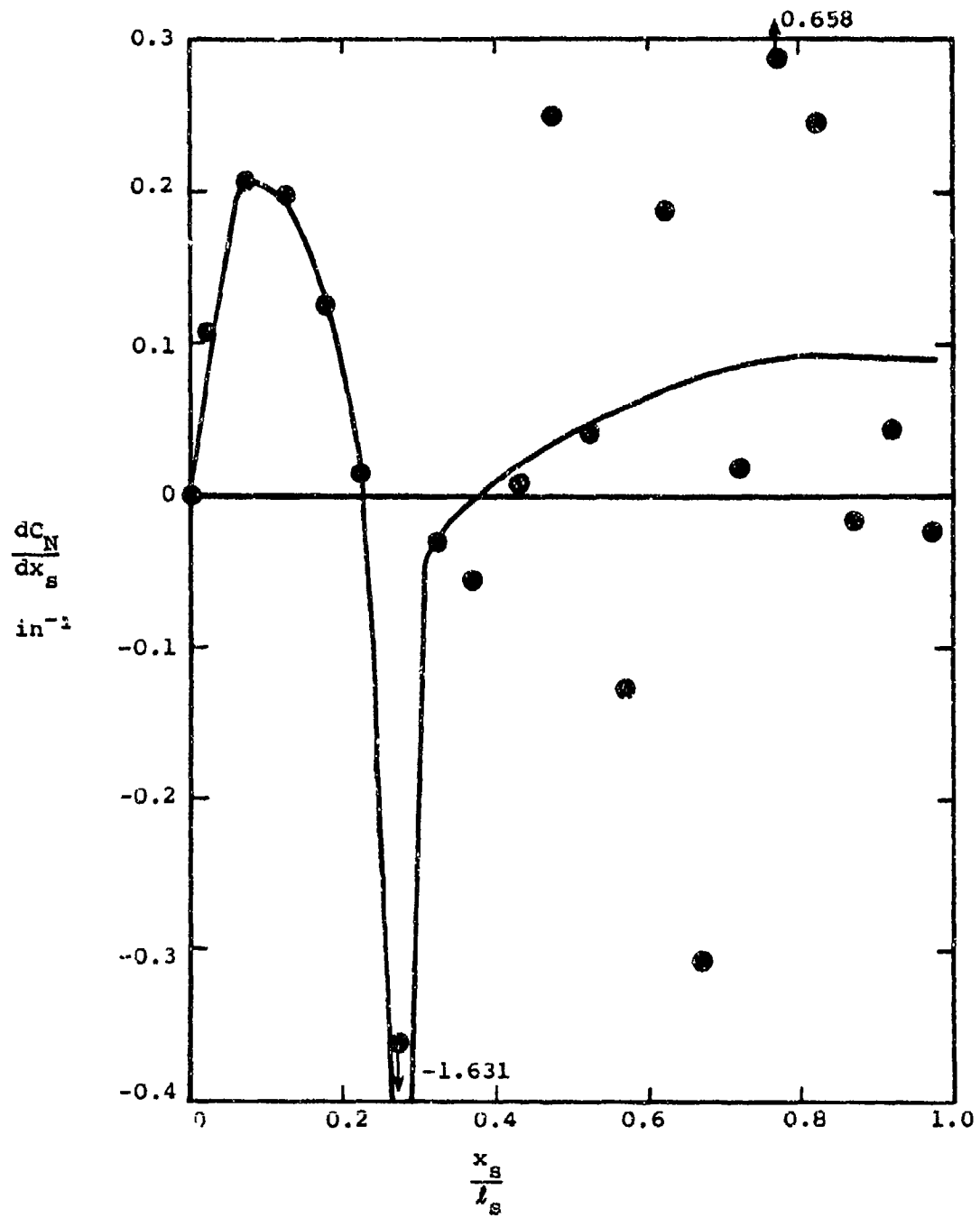
(b) Normal-force distribution.

Figure 5.- Concluded.

58

Fuselage Ordinates

x/ℓ_f	r/ℓ_f
0	0
0.0328	0.0091
0.0657	0.0171
0.0986	0.0241
0.1315	0.0300
0.1643	0.0350
0.1972	0.0390
0.2301	0.0421
0.2629	0.0443
0.2958	0.0453
0.3200	0.0457
0.7534	0.0457
0.7669	0.0454
0.7998	0.0438
0.8326	0.0418
0.8655	0.0395
0.8984	0.0372
0.9313	0.0349
0.9641	0.0326
1.0000	0.0302

Wind Airfoil
Section
NACA 65A006

All dimensions in inches
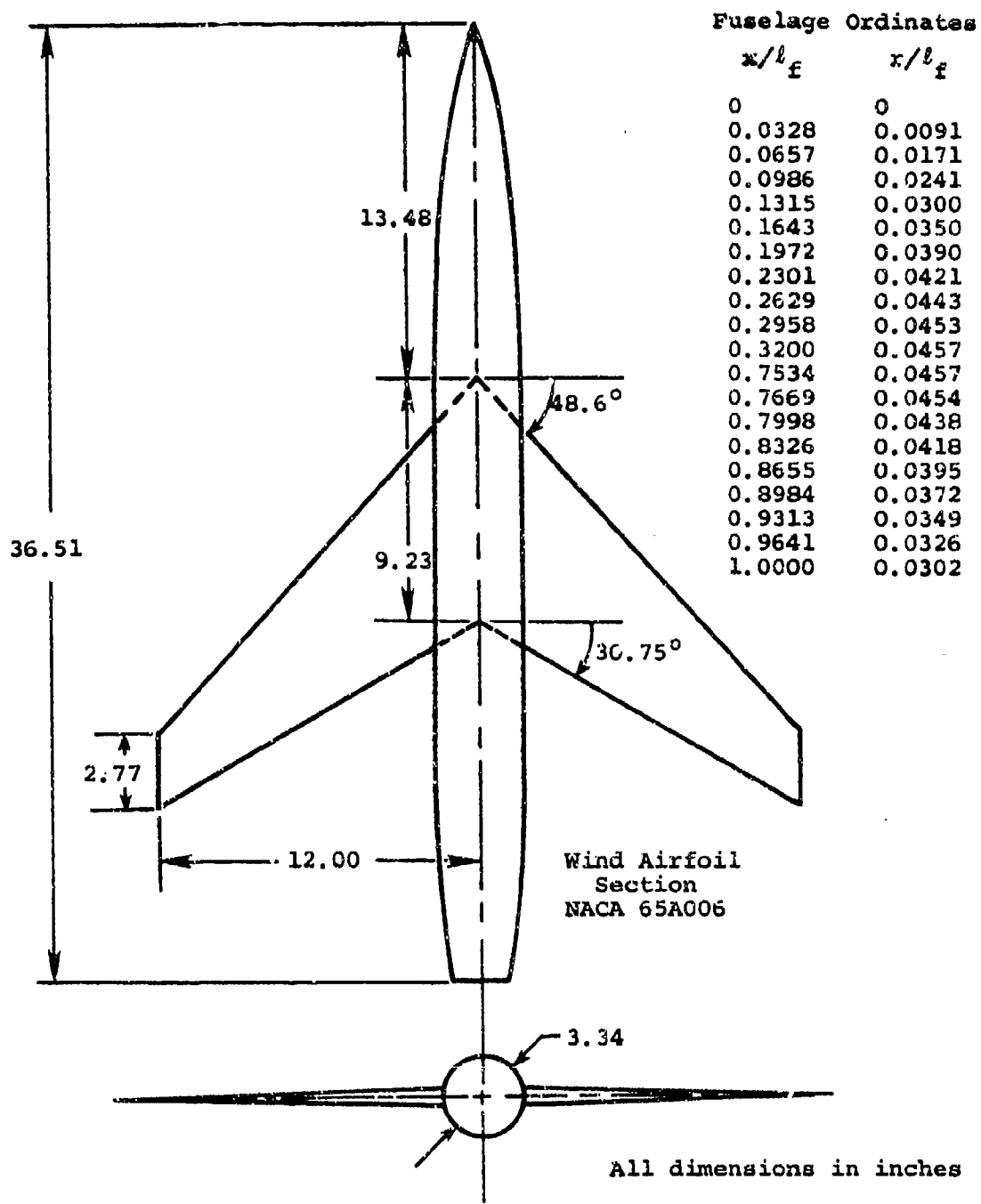
(a) Wing-fuselage combination.

Figure 6.- Wind-tunnel model.
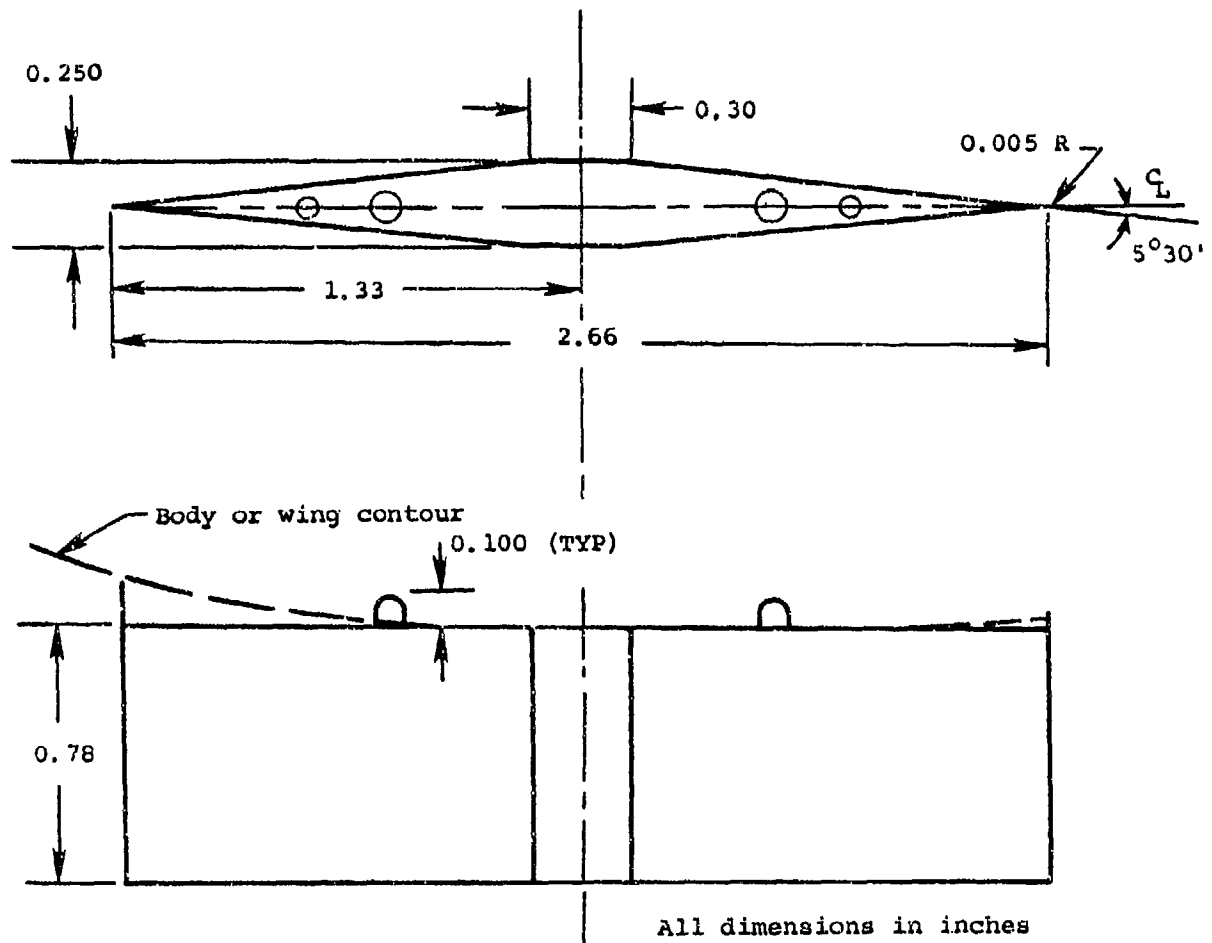
(b) Details and dimensions of the pylons.

Figure 6.- Continued.
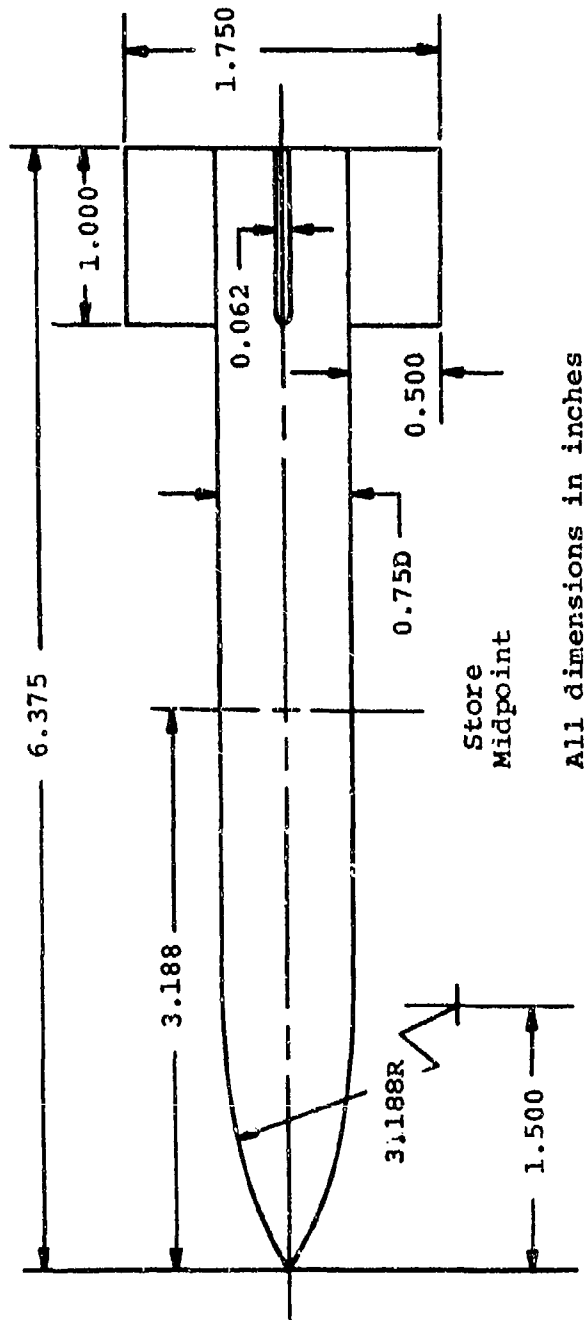
(c) Ogive-cylinder store with rectangular cruciform fins.

Figure 6.- Concluded.
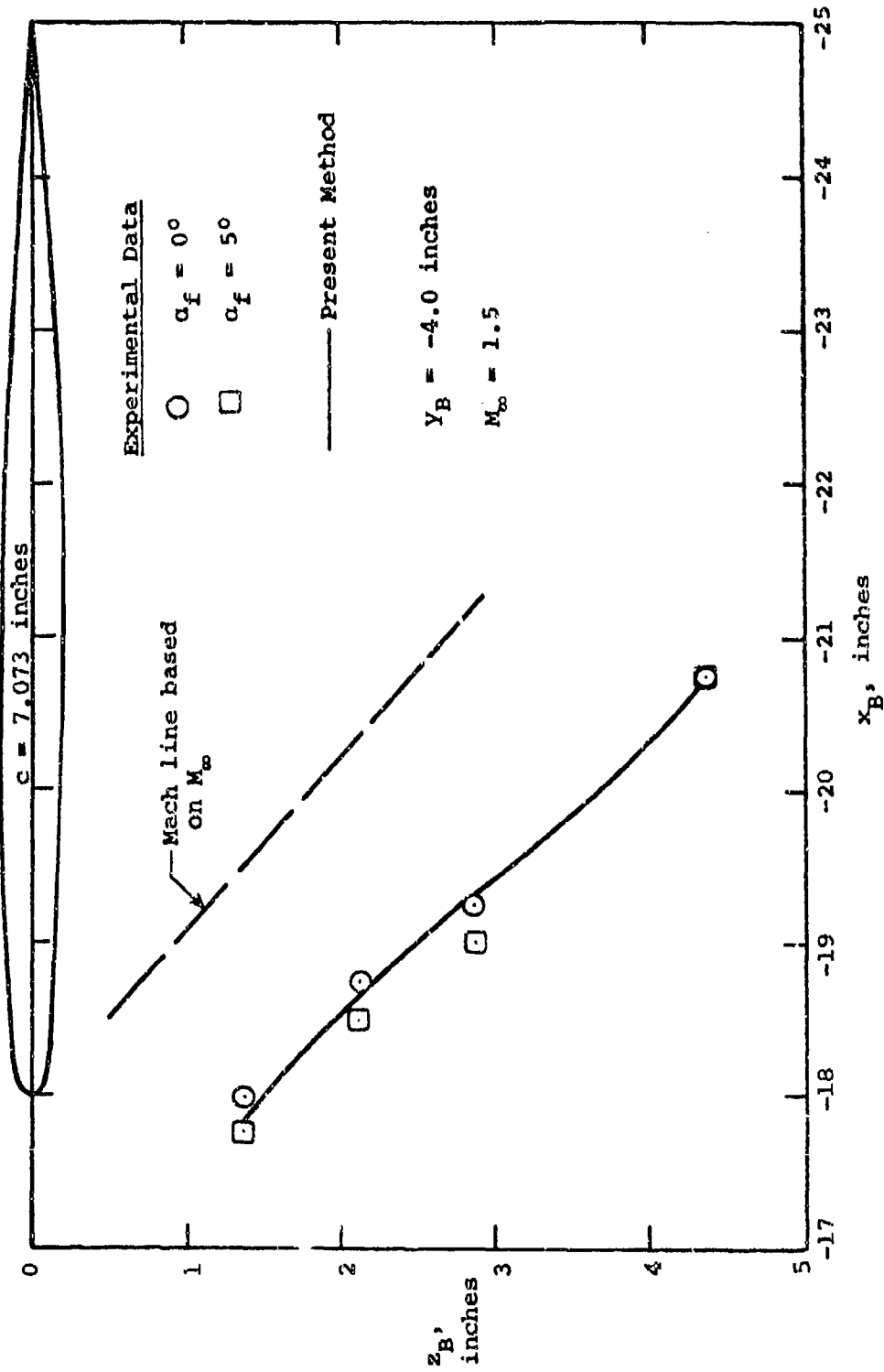
Figure 7.- Shock shape deduced from flow field properties.

(a) $M_\infty = 1.5$.

Experimental Data

○ $\alpha_f = 0°$
□ $\alpha_f = 5°$

——— Present Method
——— Love with Rizzi
      input

$Y_B = -4.0$ inches
$M_\infty = 2.0$

$c = 7.073$ inches

Mach line based
on M_∞

x_B, inches

z_B, inches

(b) $M_\infty = 2.0$.

Figure 7.- Continued.

63

Experimental Data

○ $\alpha_f = 0^\circ$
□ $\alpha_f = 5^\circ$

———●——— Present Method

—————— Love with Rizzi
            input

$y_B = -4.0$ inches

$M_\infty = 2.5$

c = 7.073 inches

Mach line based
on M_∞

(c) $M_\infty = 2.5$

Figure 7.- Concluded.

64

1.37 inches

$\frac{u}{V_\infty}$

(positive backwards)

Exp. Data   Present Method

⊙   ————

$M_\infty = 1.5$, $\alpha_f = 0^\circ$

$Y_B = -4.0$ inches
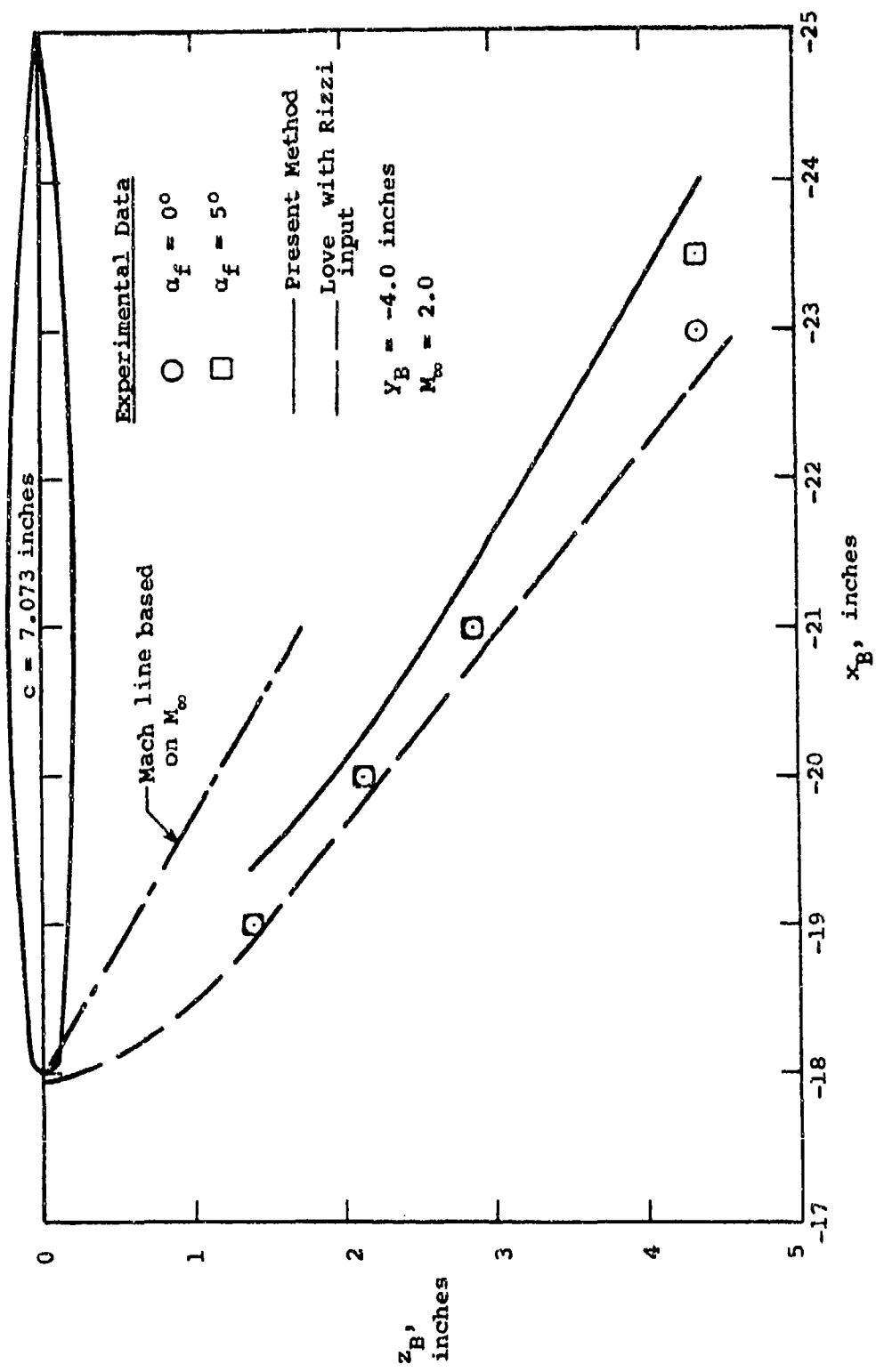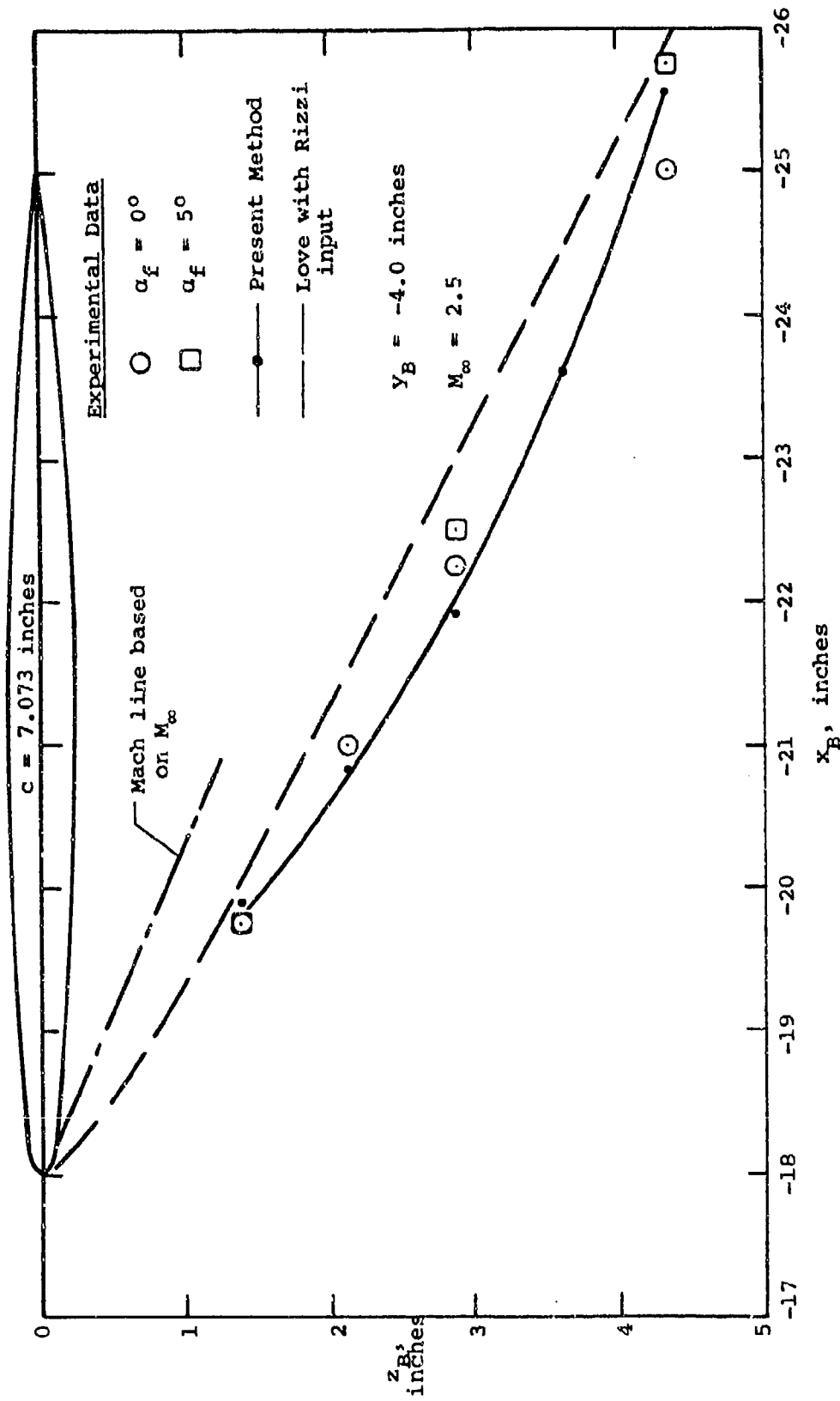
$z_B = 1.37$ inches
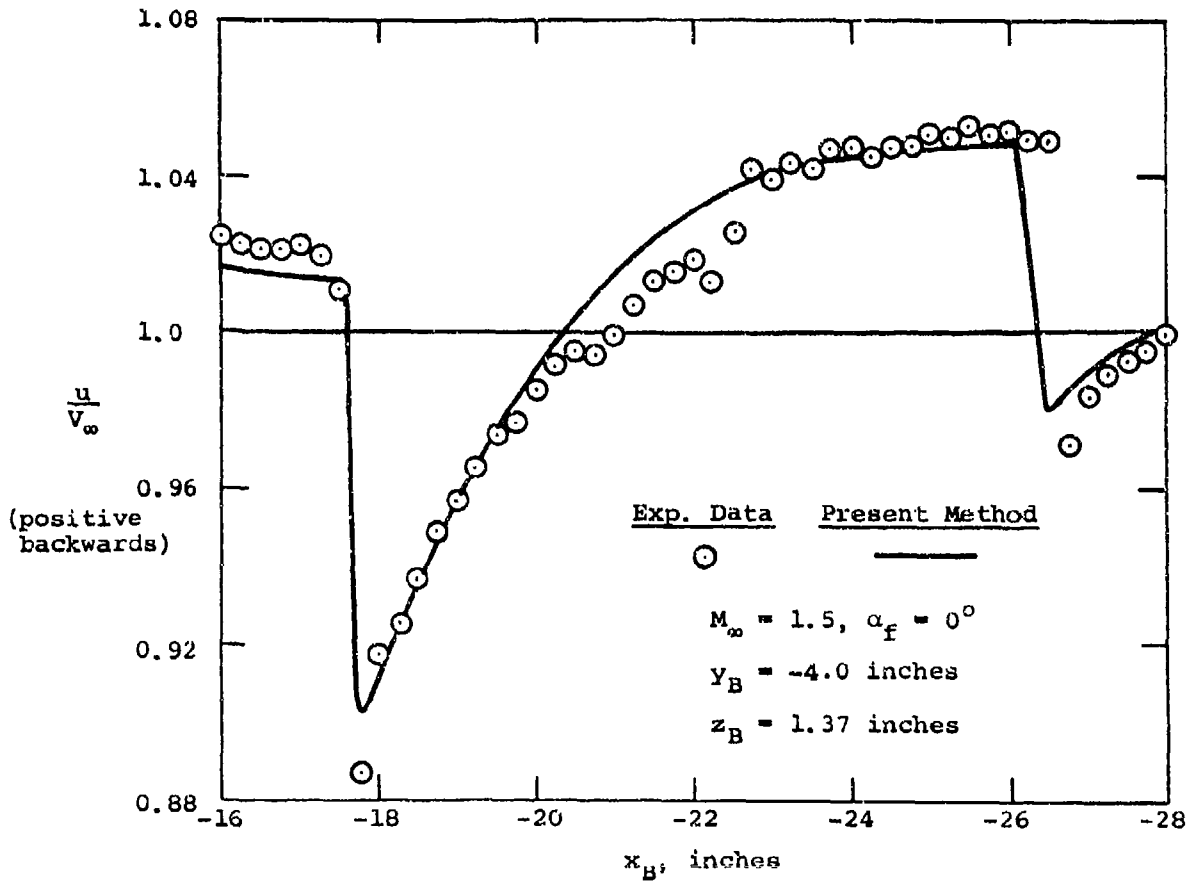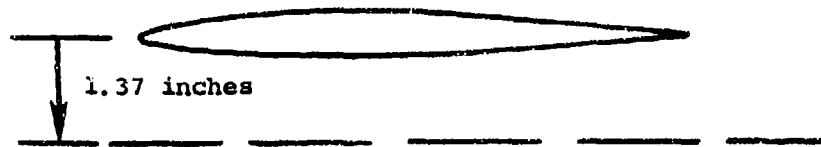
x_B, inches

(a) Backwash.

Figure 8.- Flow field under the wing at zero angle of attack at the one-third semispan location, $z_B = 1.37$ inches.

65

1.37 inches

$\dfrac{v}{V_\infty}$
(positive inboard)
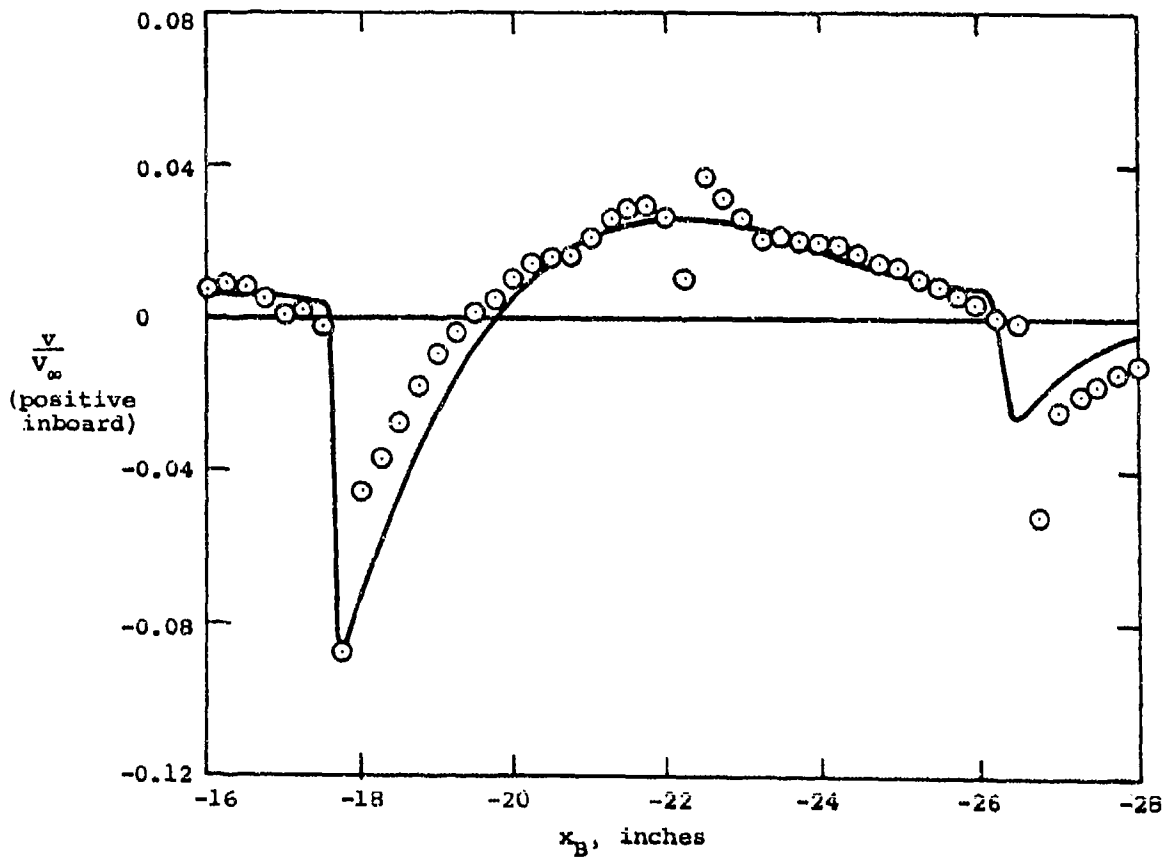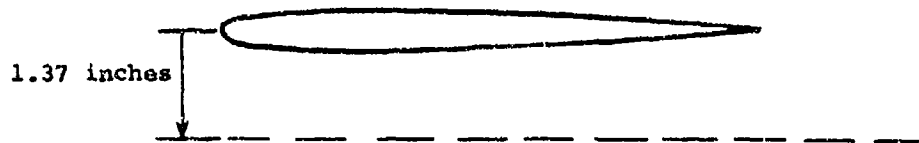
x_B, inches

(b) Sidewash.

Figure 8.- Continued.

66

1.37 inches
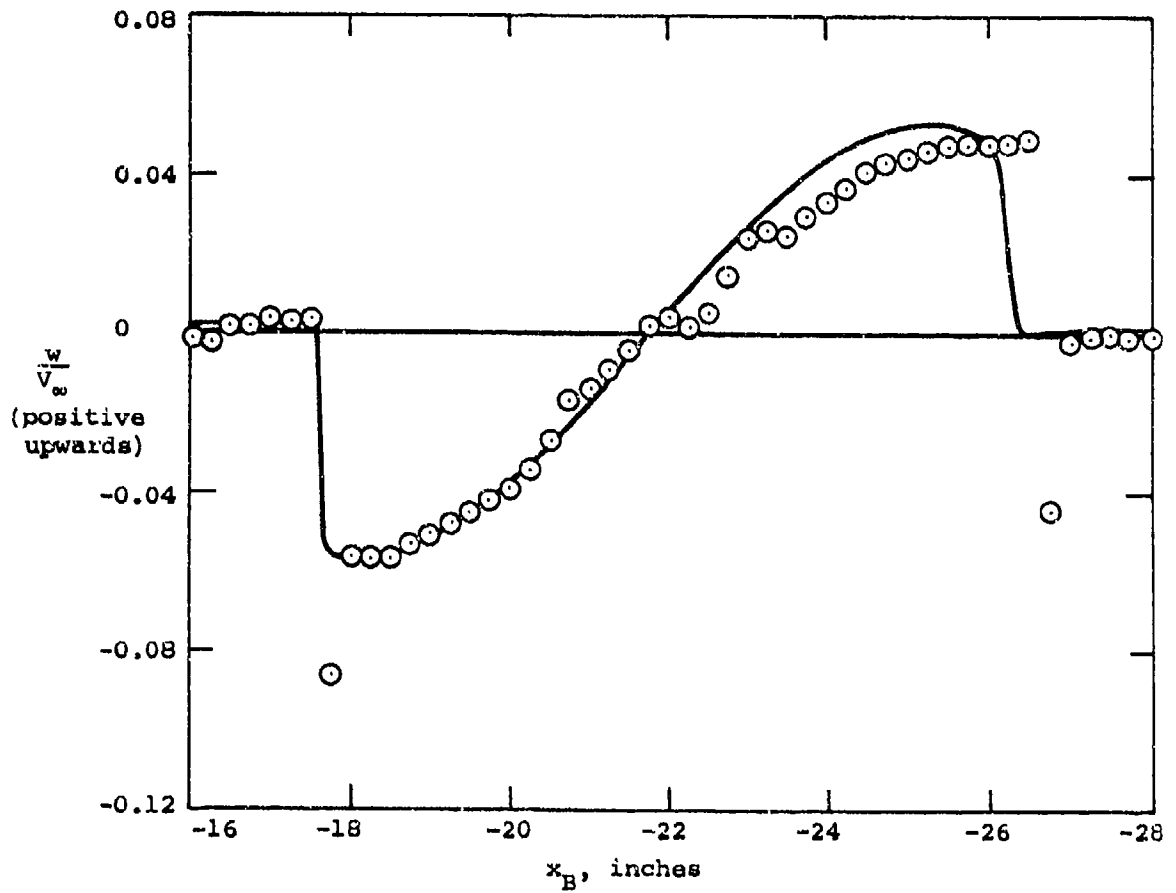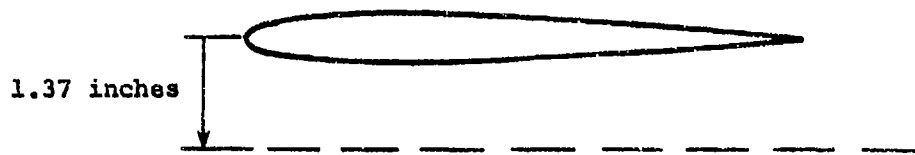
(c) Upwash.

Figure 8 .- Concluded.

67
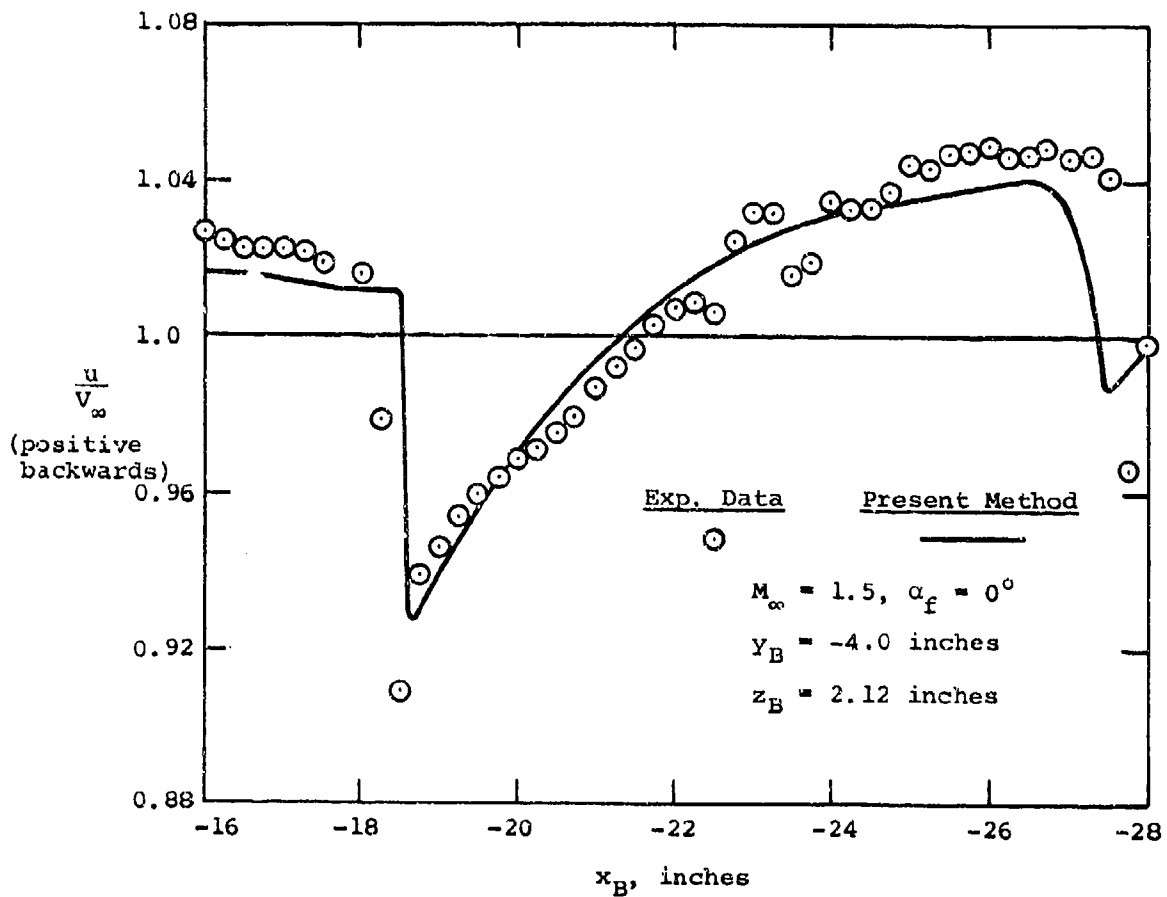
(a) Backwash.

Figure 9.- Flow field under the wing at zero angle of attack at the one-third semispan location, $z_B = 2.12$ inches.

68

2.12 inches

$\frac{v}{V_\infty}$

(positive inboard)
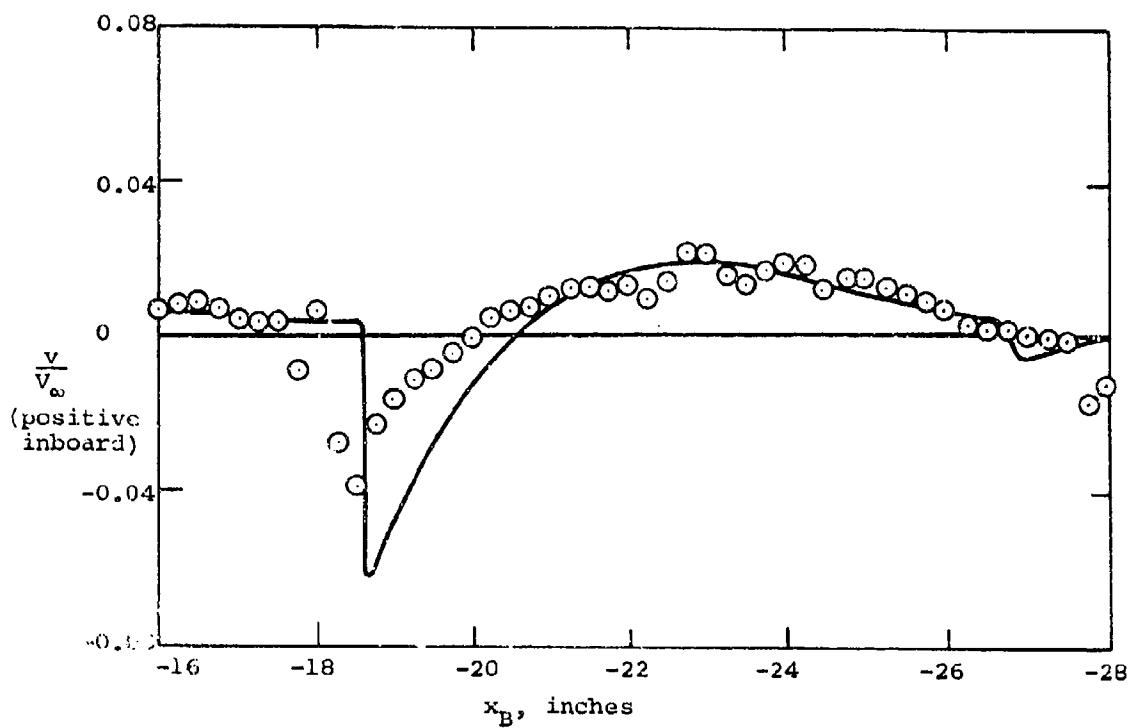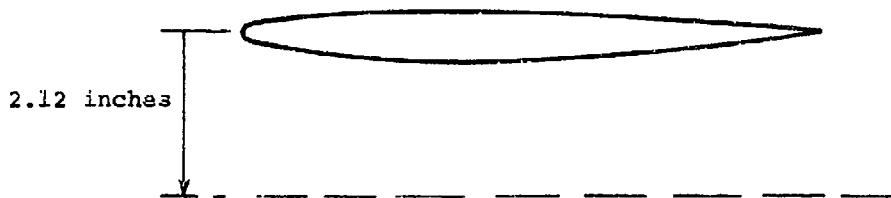
x_B, inches

(b) Sidewash.

Figure 9.- Continued.

69

2.12 inches

$\frac{w}{V_\infty}$

(positive upwards)
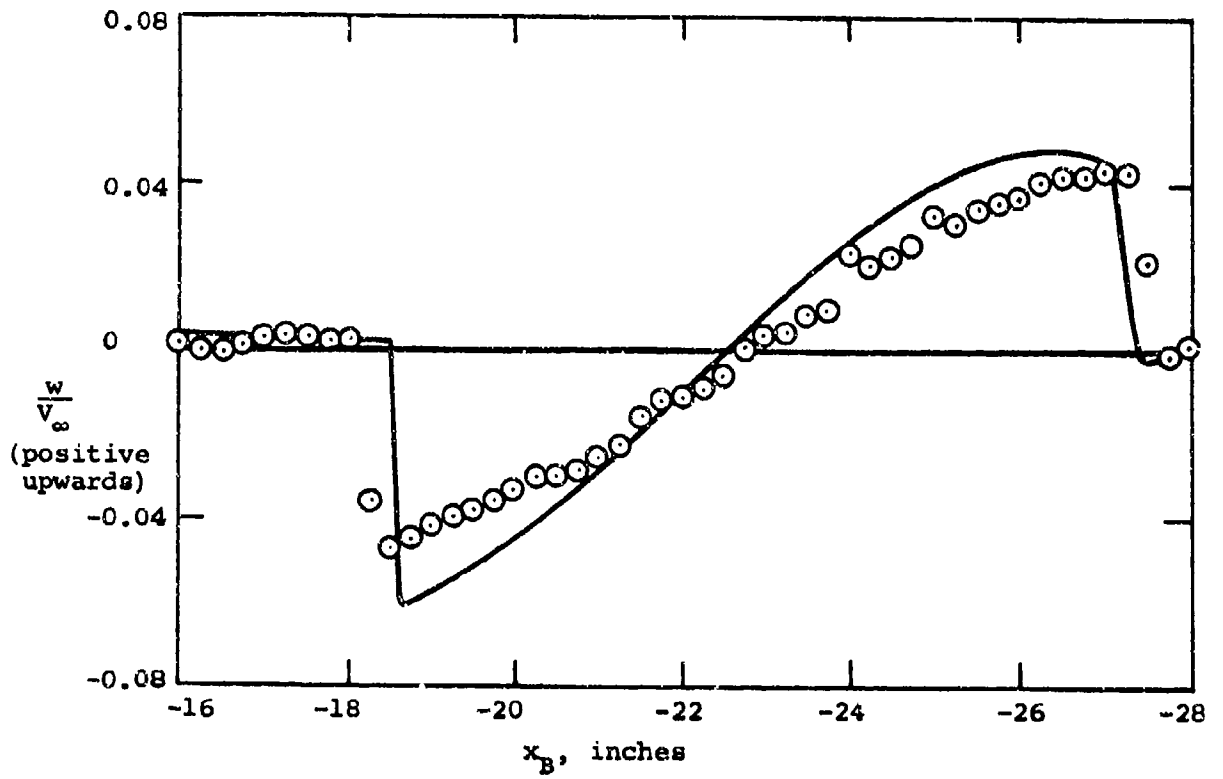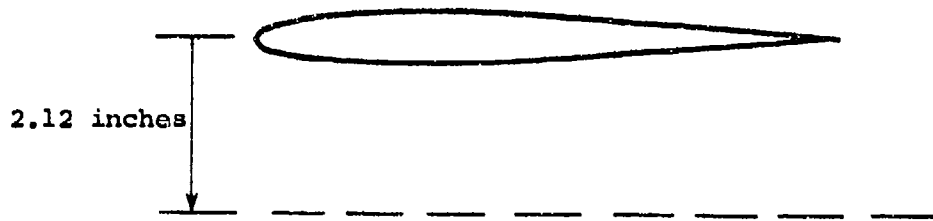
x_B, inches

(c)   Upwash.

Figure 9.- Concluded.

70
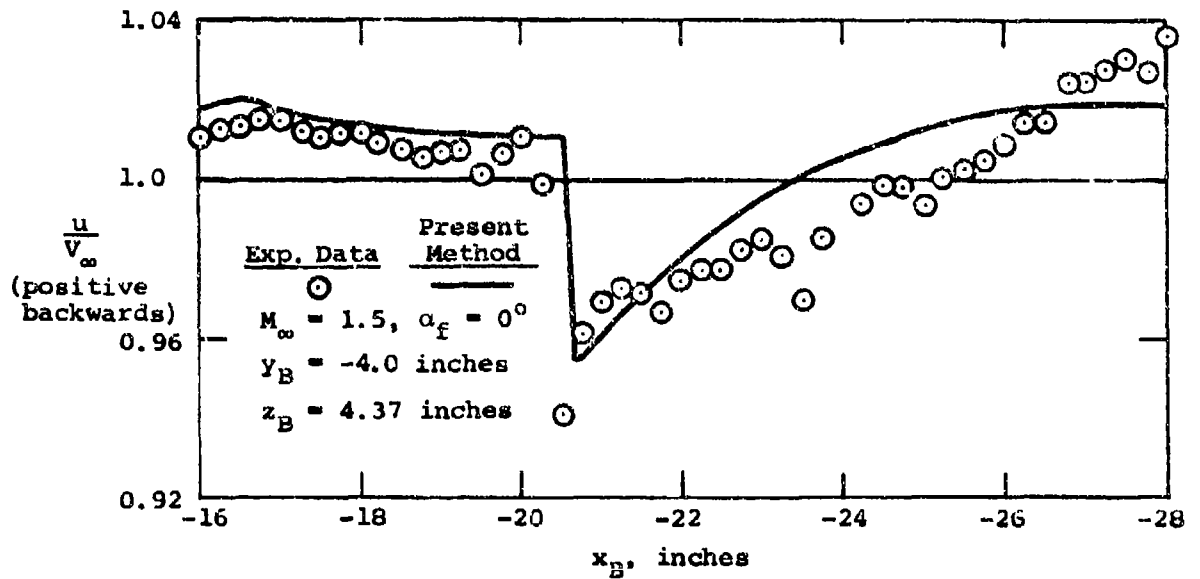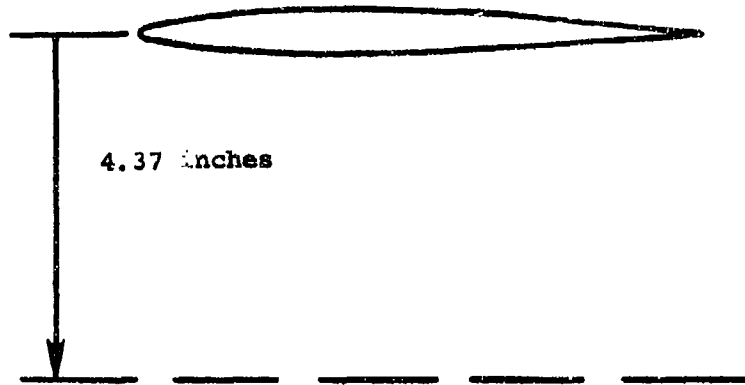
(a) Backwash.

Figure 10.- Flow field under the wing at zero angle of attack at the one-third semispan location, $z_B = 4.37$ inches.

71

4.37 inches

$\frac{v}{V_\infty}$
(positive inboard)
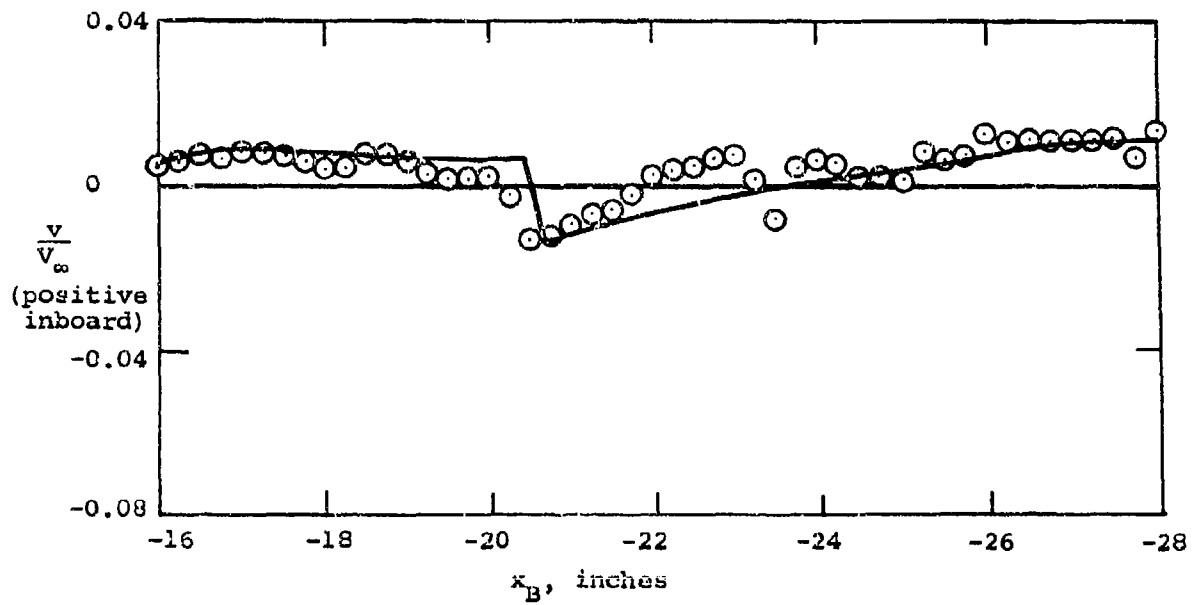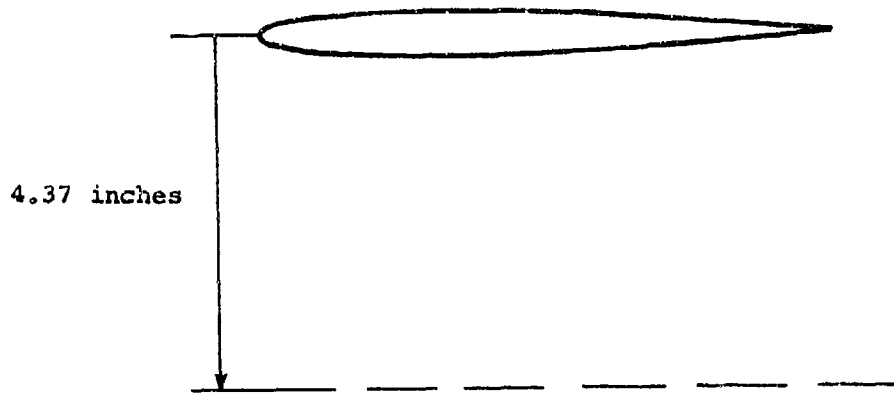
x_B, inches

(b) Sidewash.

Figure 10.- Continued.

72

4.37 inches

$\frac{w}{V_\infty}$
(positive upwards)

x_B, inches

(c) Upwash.

Figure 10.- Concluded.

73

1.37 inches

Exp, Data   Present Method

$M_\infty = 1.5,\ \alpha_f = 5^\circ$

$Y_B = -4.0$ inches

$z_B = 1.37$ inches

$\frac{v}{V_\infty}$

(positive inboard)
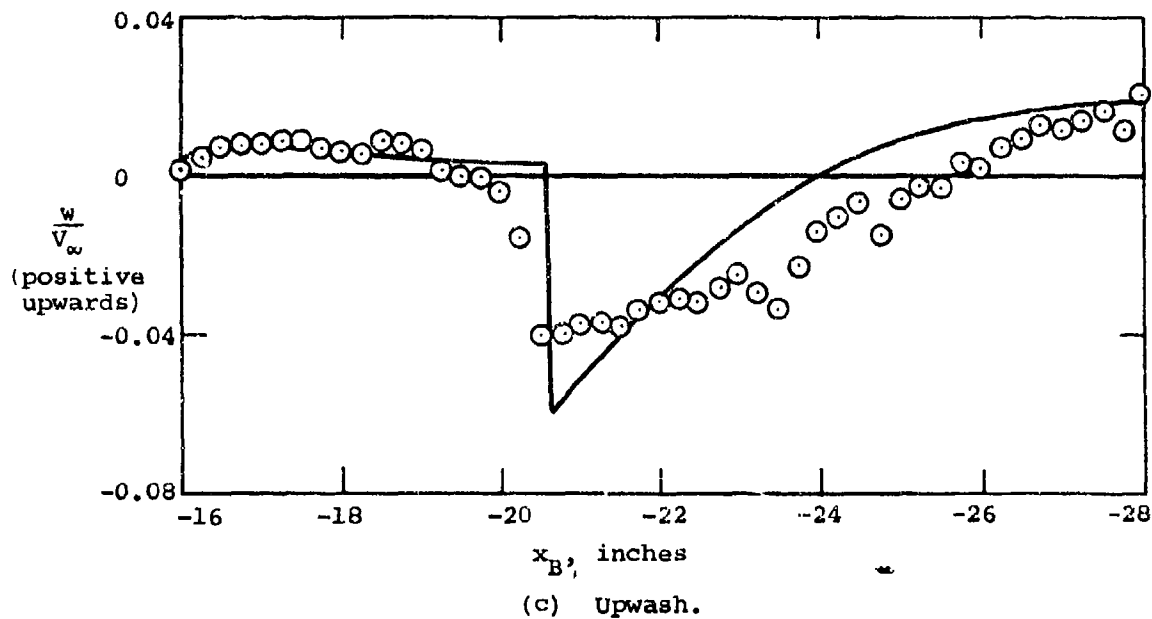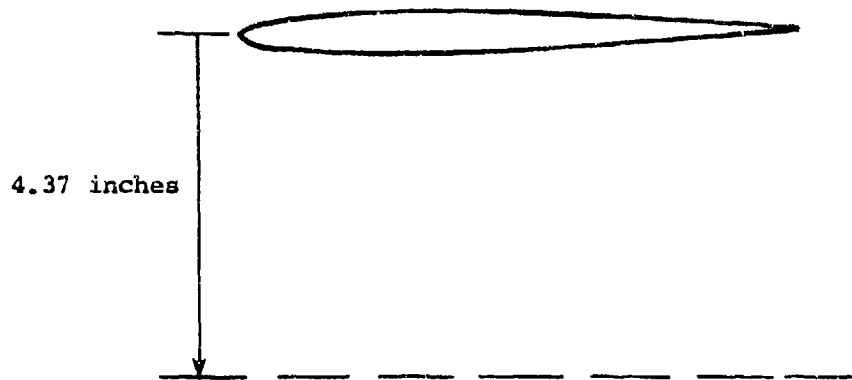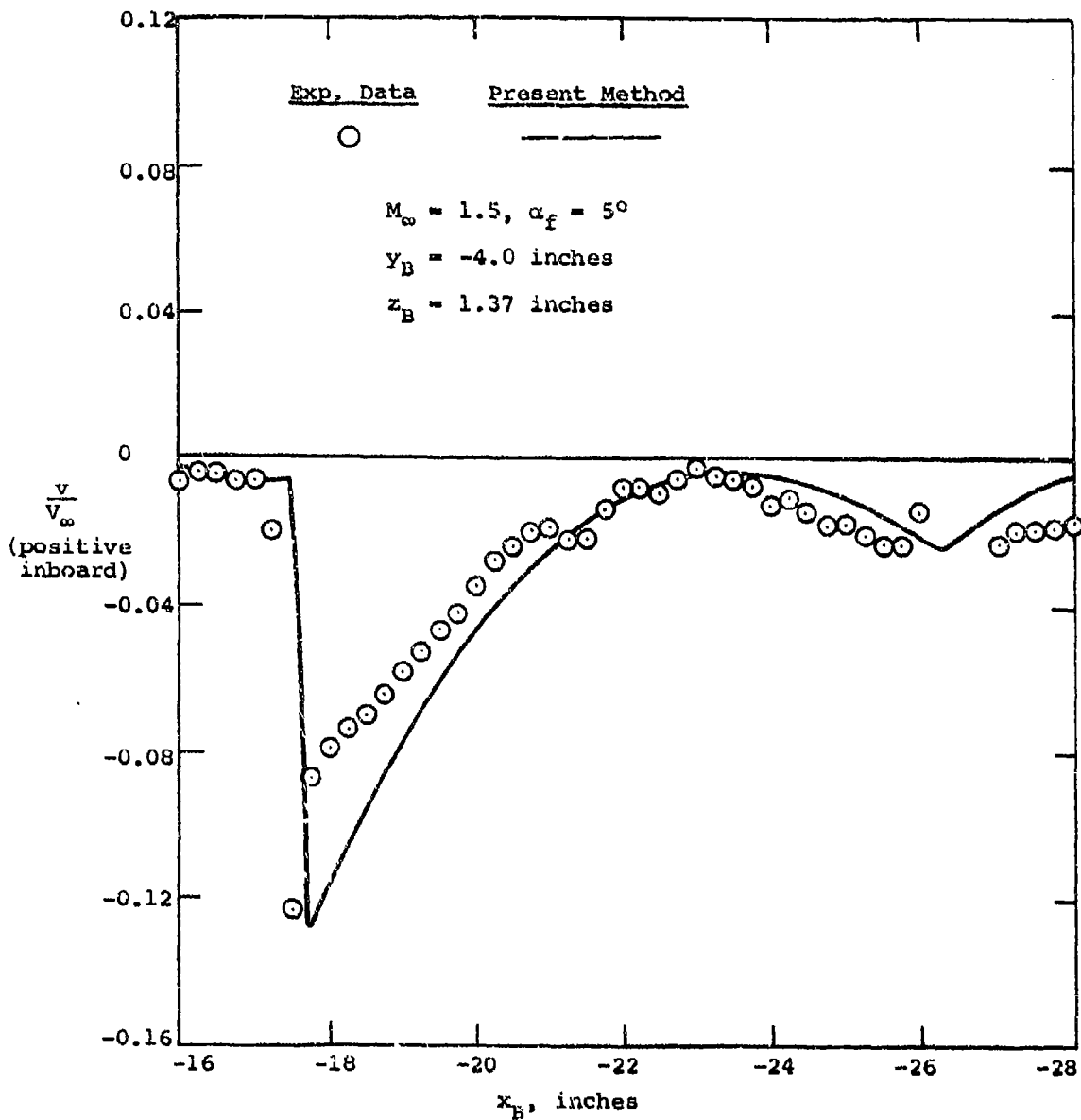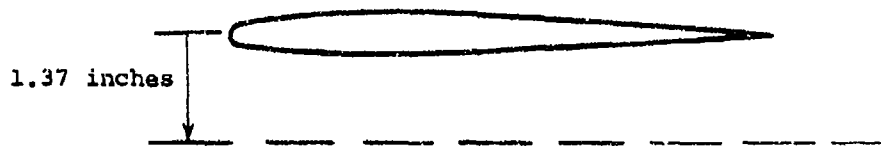
x_B, inches

(a) Sidewash.

Figure 11.- Flow field under the wing at angle of attack at the one-third semispan location, $z_B = 1.37$ inches.

74

1.37 inches

$\frac{w}{V_\infty}$

(positive upwards)
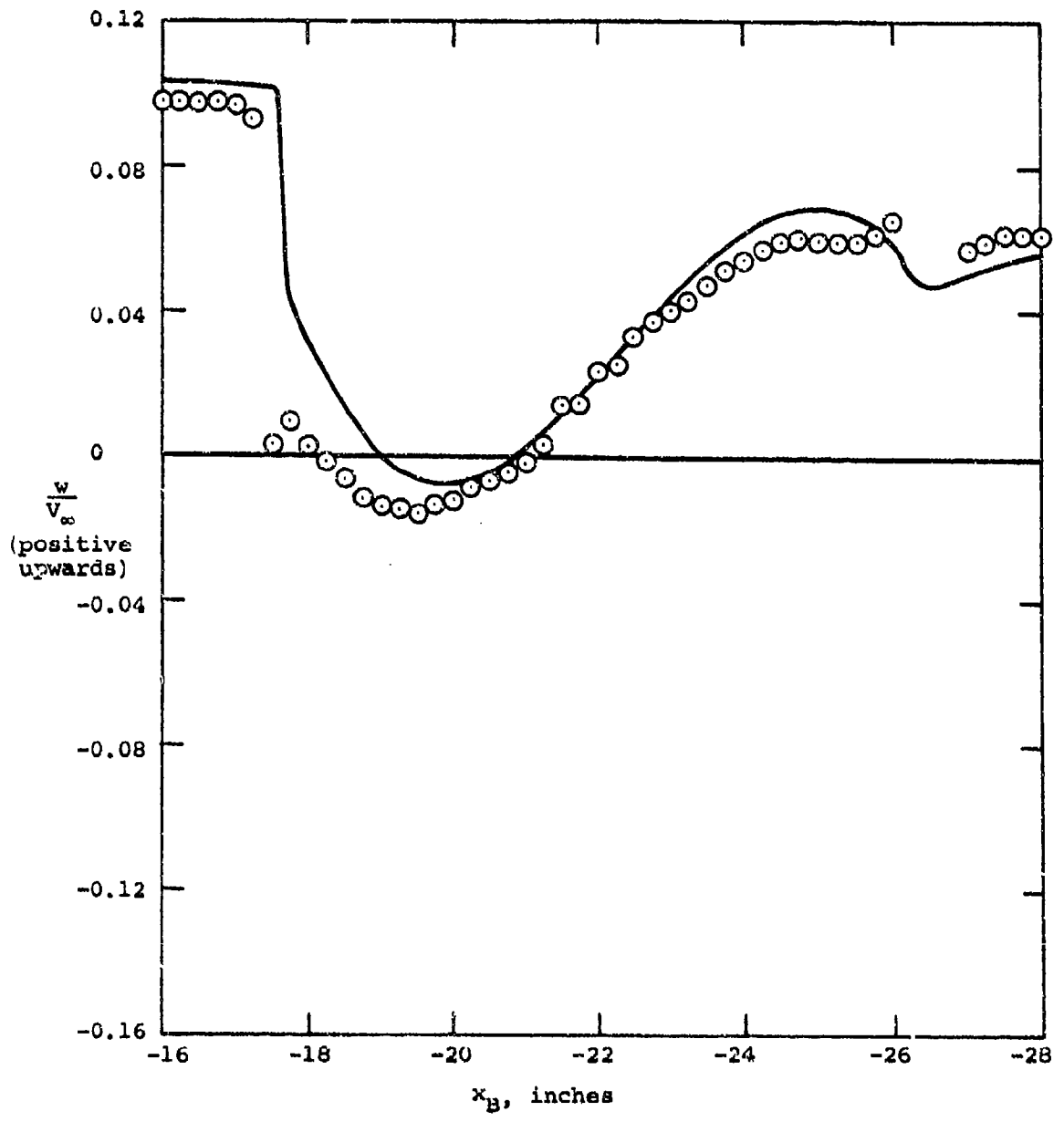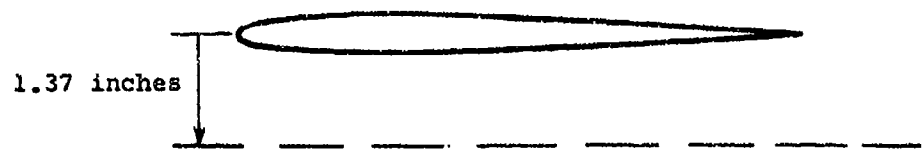
x_B, inches

(b) Upwash.

Figure 11.- Concluded.

75
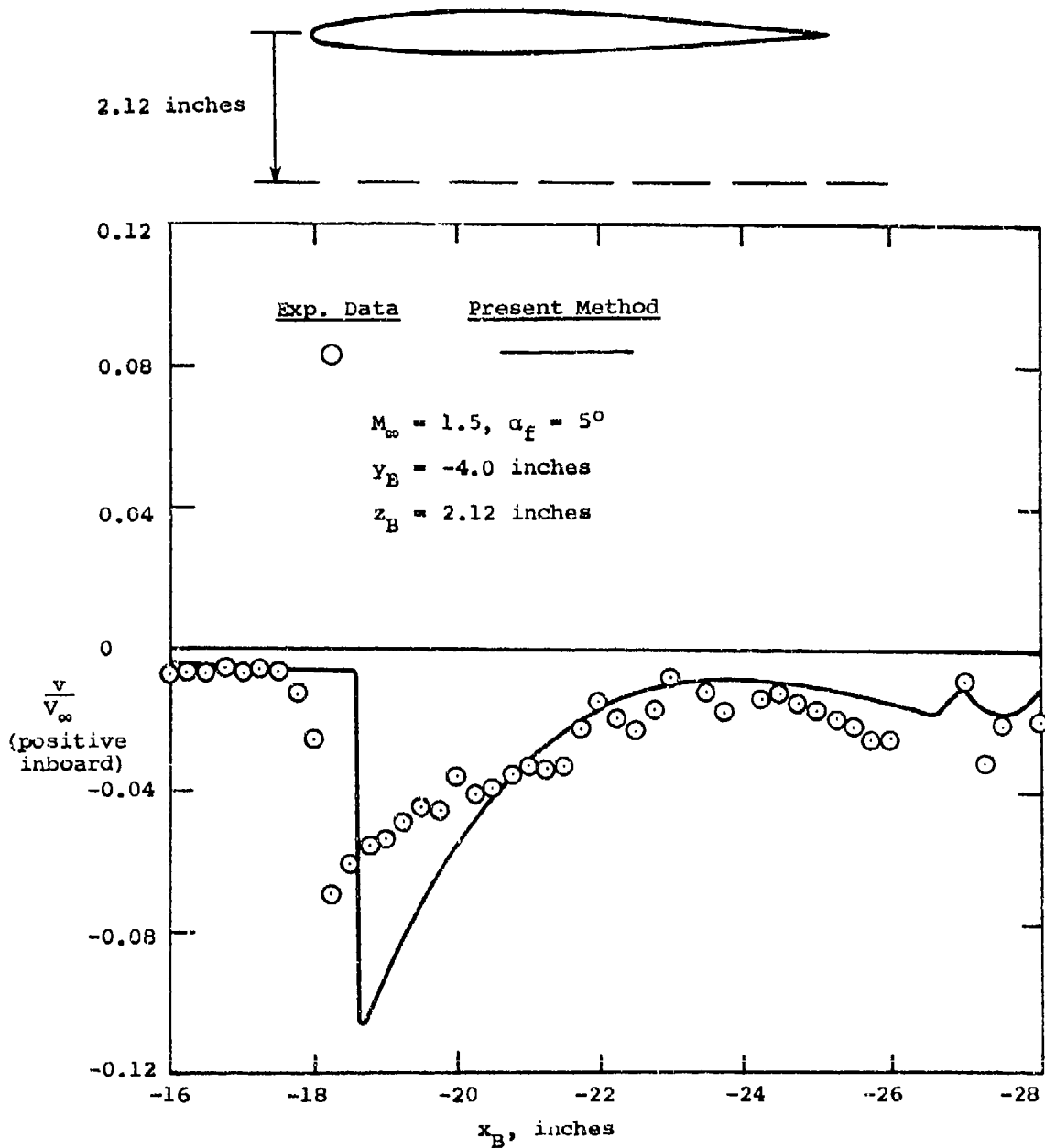
(a) Sidewash.

Figure 12.- Flow field under the wing at angle of attack at the one-third semispan location, z_B = 2.12 inches.

2.12 inches

$\frac{w}{V_\infty}$ (positive upwards)
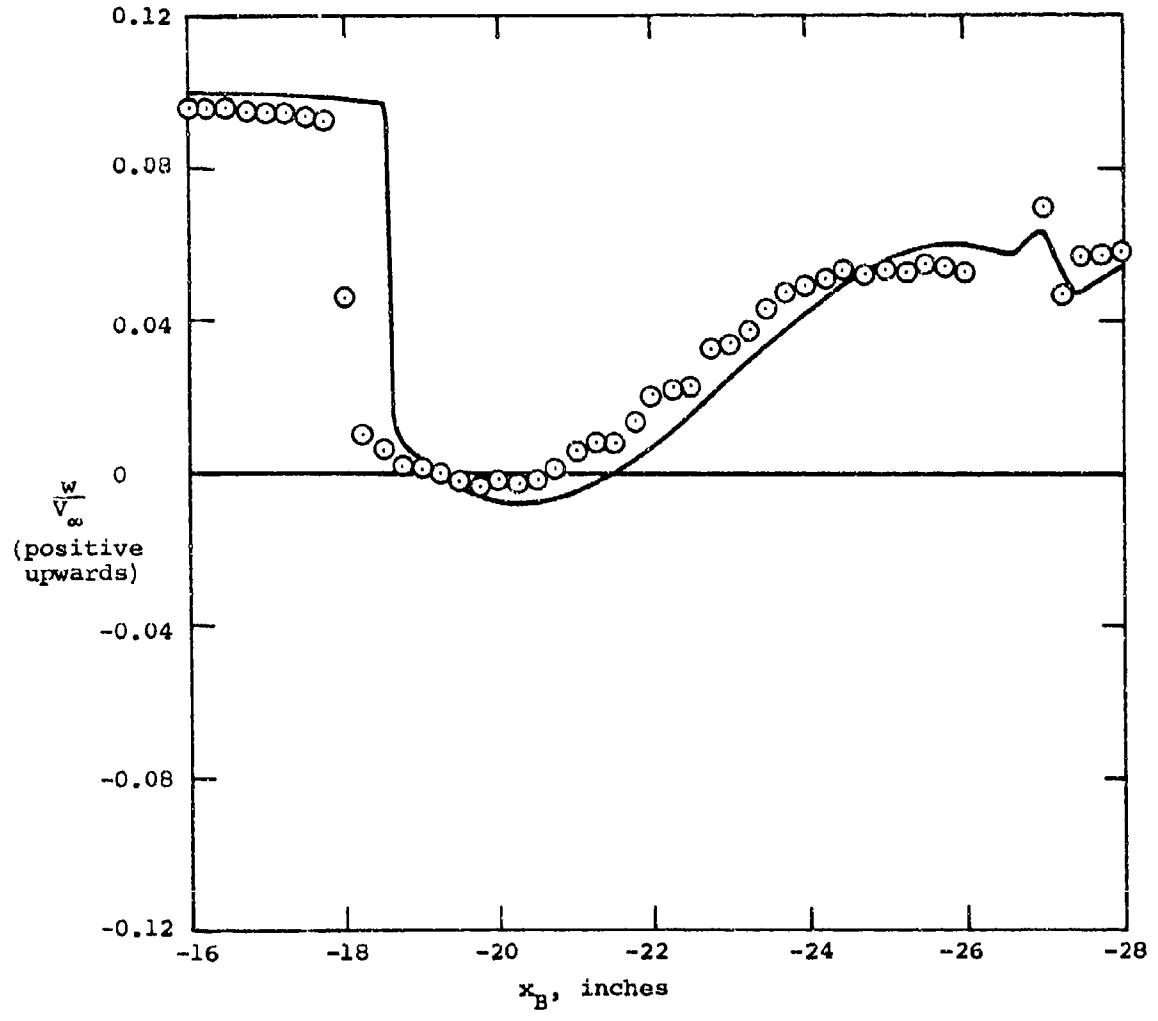
x_B, inches

(b) Upwash.

Figure 12.- Concluded.

77
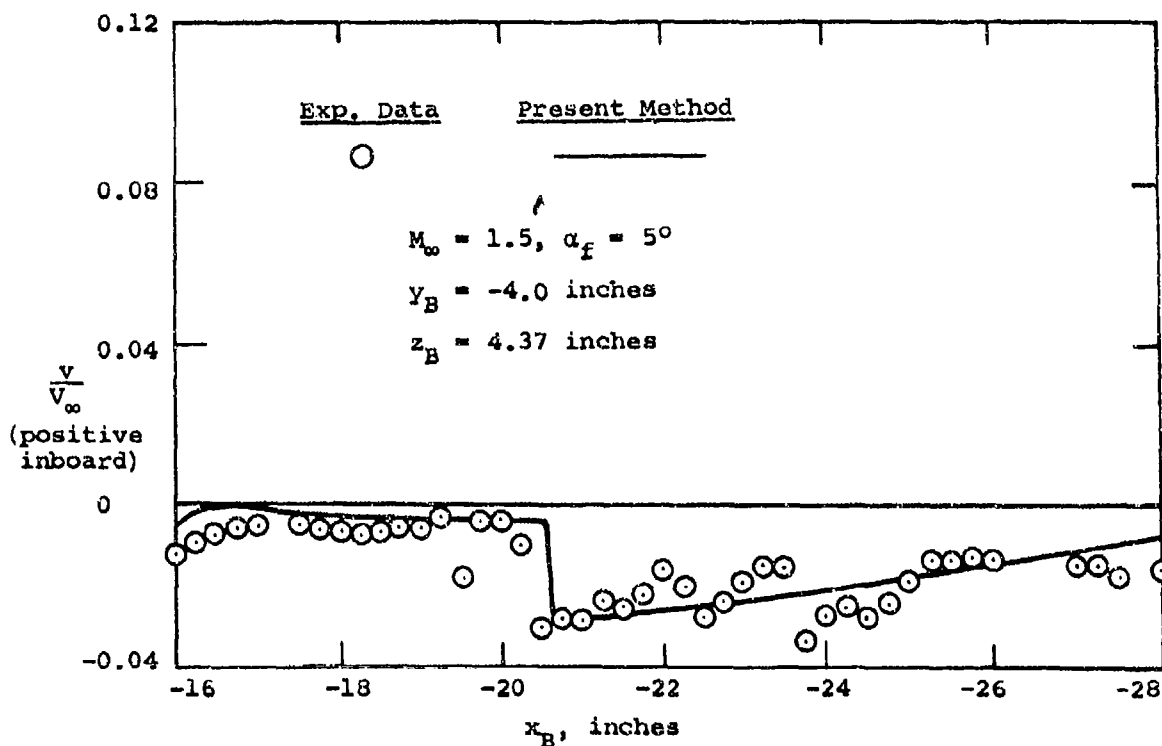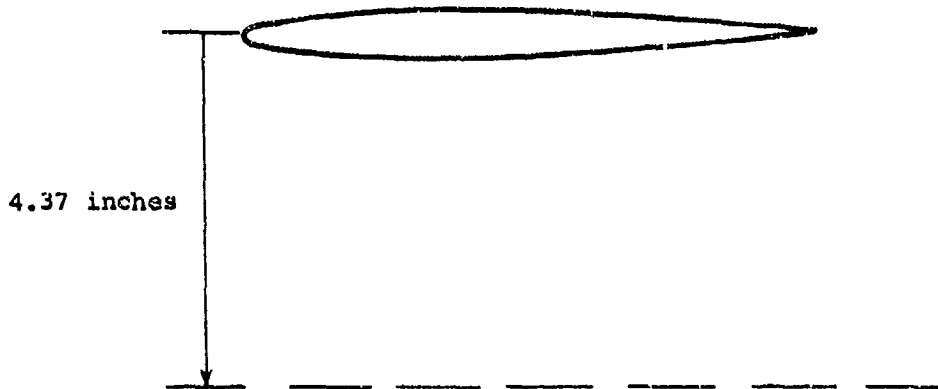
(a) Sidewash.

Figure 13.- Flow field under the wing at angle of attack at the one-third semispan location, z_B = 4.37 inches.

4.37 inches
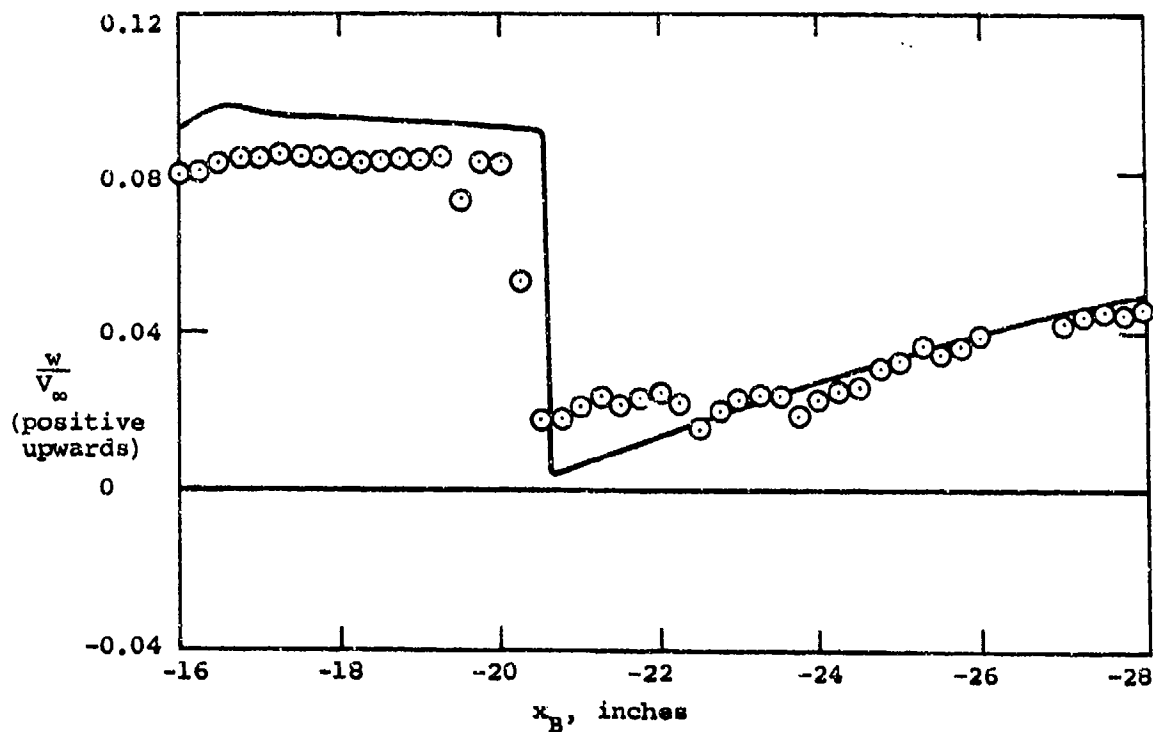
(b) Upwash.

Figure 13.- Concluded.

79
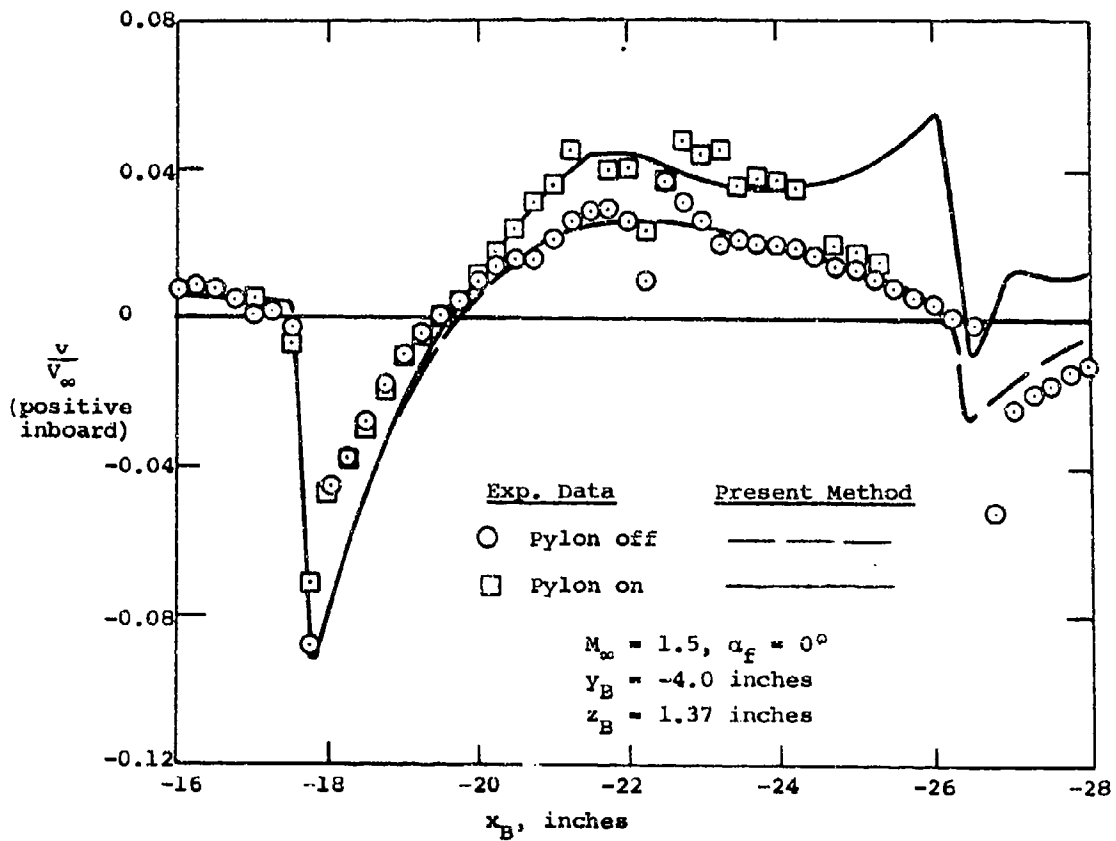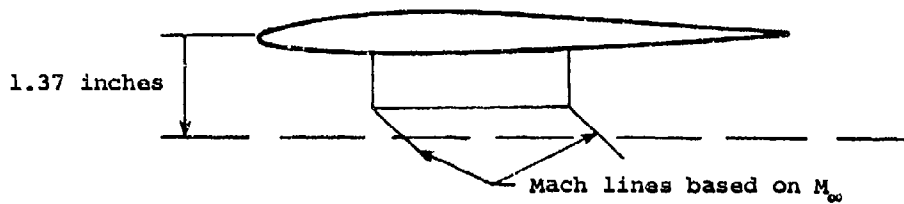
(a) Sidewash.

Figure 14.- Effect of the pylon on the flow field under the wing
at zero angle of attack at the one-third semispan location.

80

1.37 inches

Mach lines based on M_∞

$\frac{w}{V_\infty}$
(positive upwards)

x_B, inches
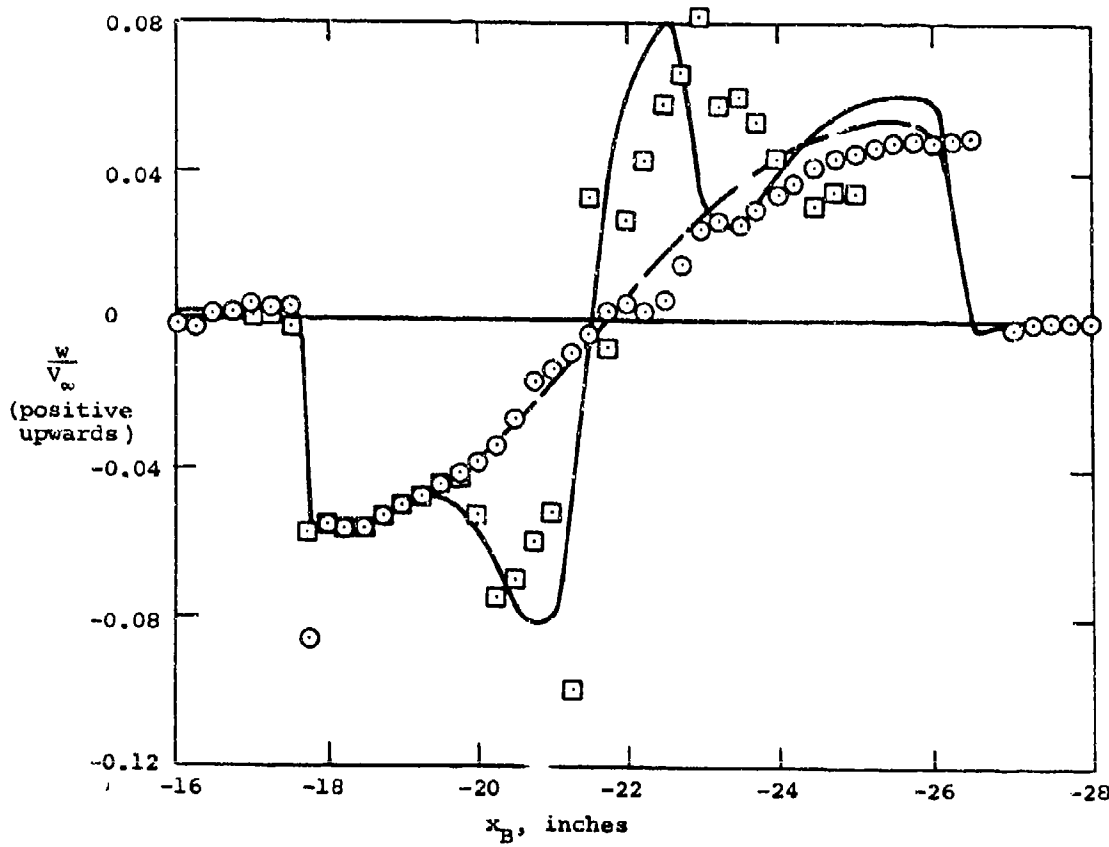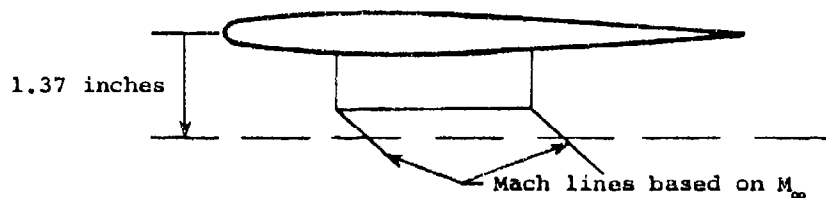
(b) Upwash.

Figure 14.- Concluded.

81

1.37 inches

Mach lines based on M_∞

Exp. Data   Present Method

○   Pylon off   — — —

□   Pylon on   ———

$M_\infty = 1.5$, $\alpha_f = 5^0$

$y_B = -4.0$ inches

$z_B = 1.37$ inches

$\dfrac{V}{V_x}$
(positive inboard)

x_B, inches
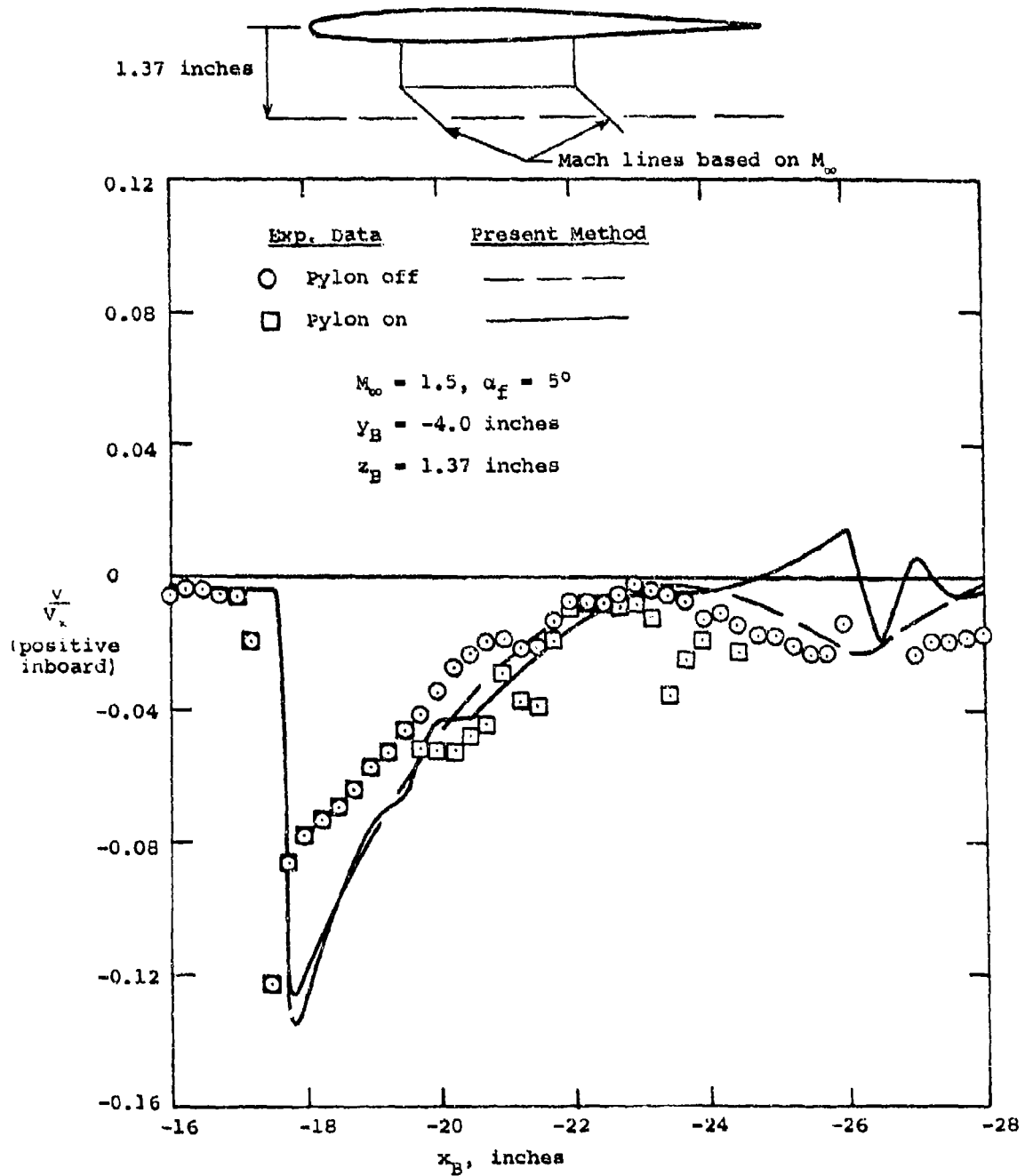
(a)   Sidewash.

Figure 15.— Effect of the pylon on the flow field under the wing at angle of attack at the one-third semispan location.

82

1.37 inches

Mach lines based on M_∞

$\dfrac{w}{V_\infty}$

(positive upwards)

x_B, inches
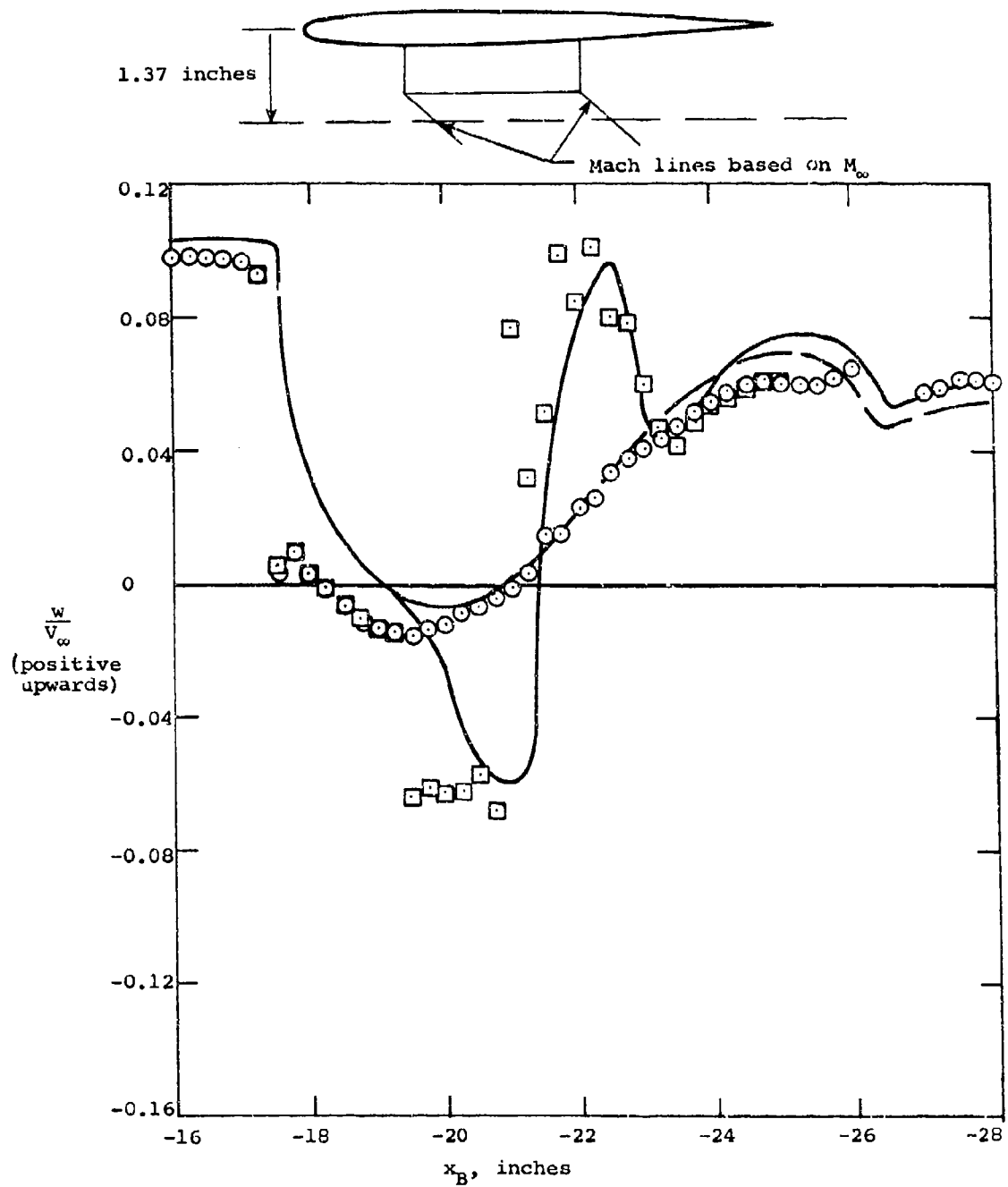
(b) Upwash.

Figure 15.- Concluded.

83
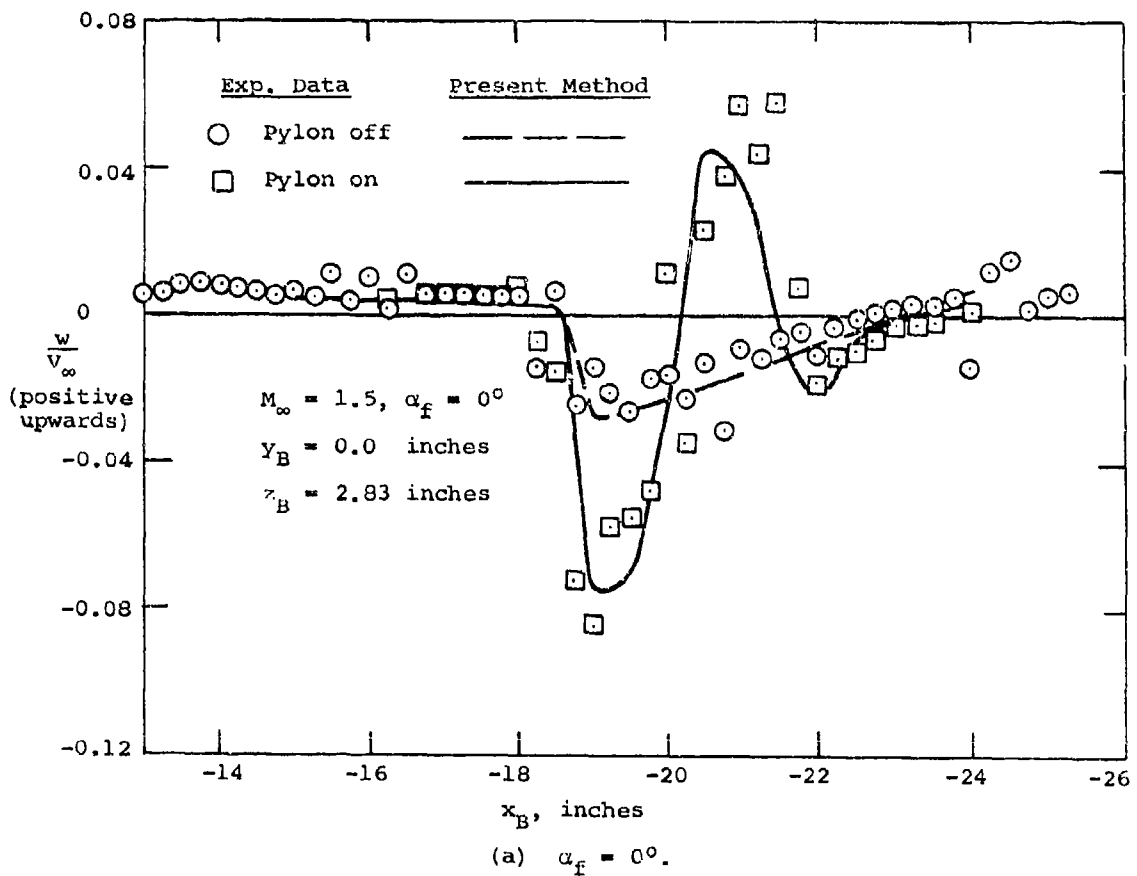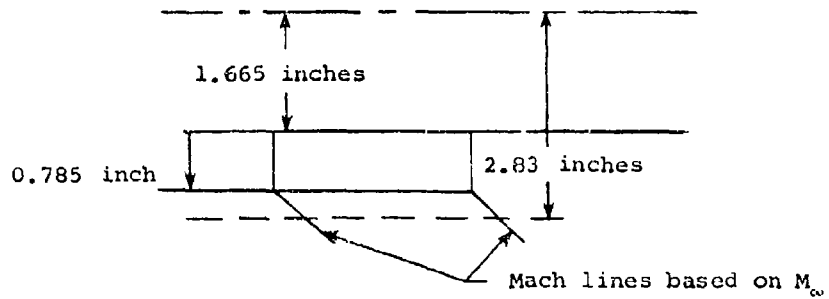
Figure 16.- Effect of the pylon on upwash below the fuselage centerline at zero angle of attack.
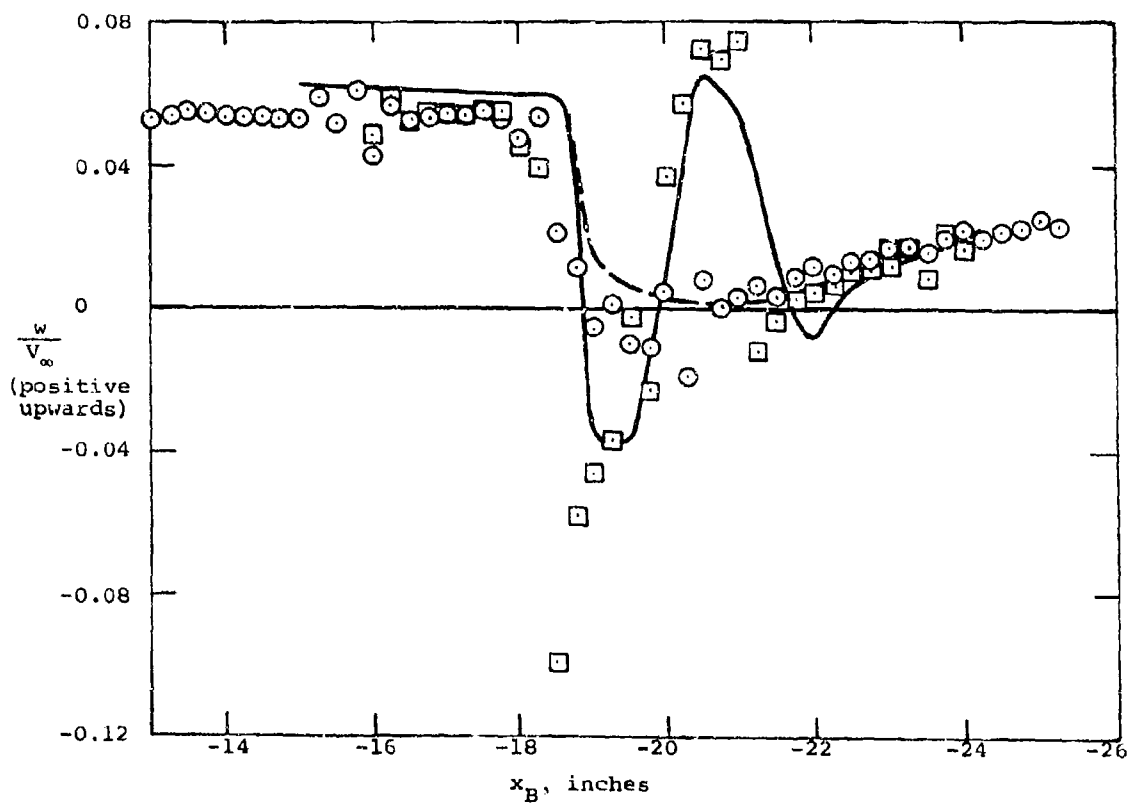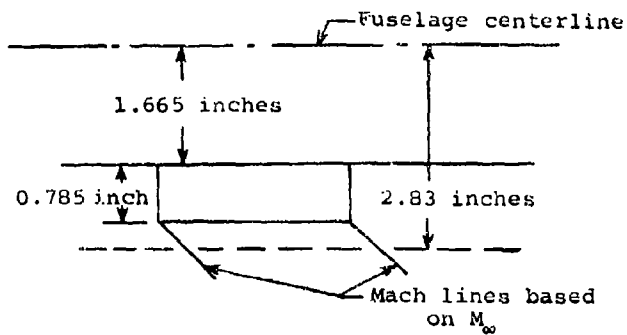
(b) $\alpha_f = 5°$.

Figure 16.- Concluded.
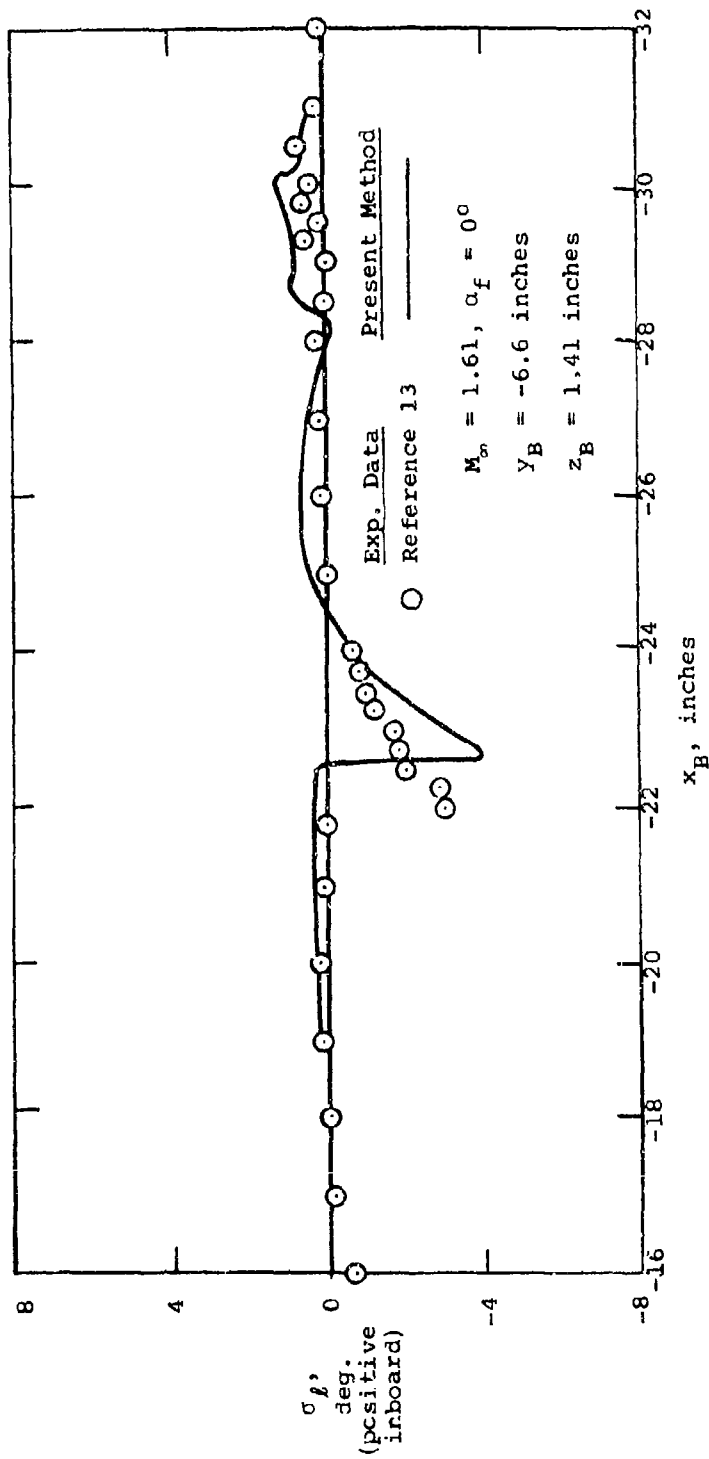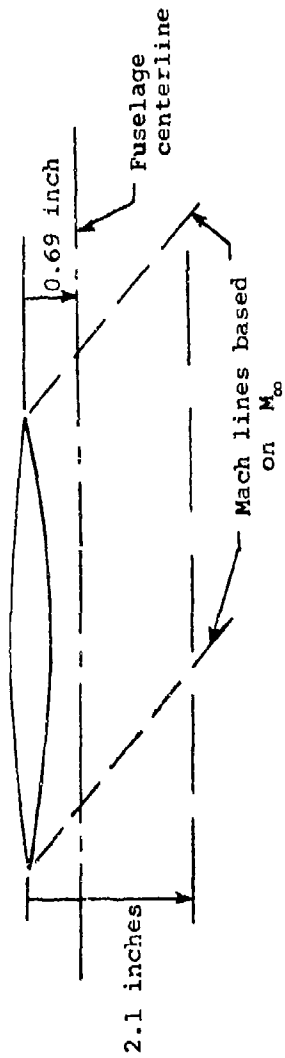
(a) Local sidewash angle.

Figure 17.- Flow field under sharp-edged trapezoidal
wing-fuselage configuration, $\alpha_f = 0°$.
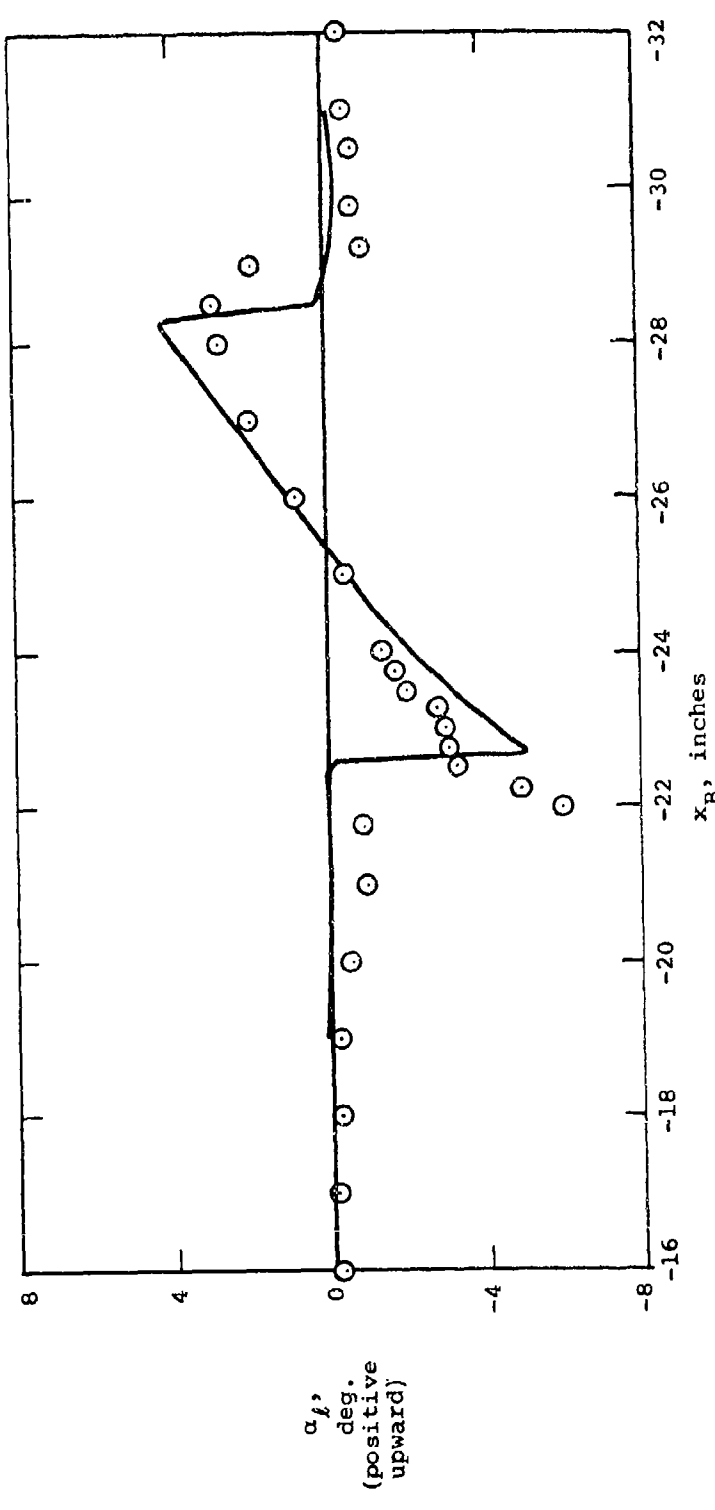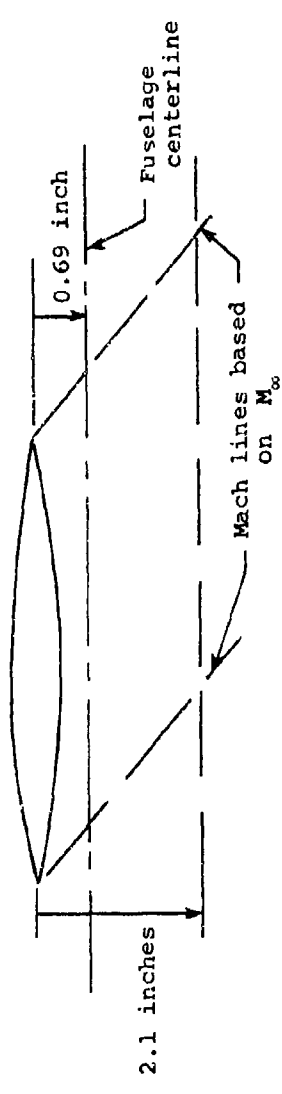
(b) Local upwash angle.

Figure 17.- Concluded.

x_B, inches

α_ℓ, deg. (positive upward)

Fuselage centerline

0.69 inch

Mach lines based on M_∞

2.1 inches

0.69 inch

Fuselage centerline

Mach lines based on M_∞

2.1 inches

Present Method

Exp. Data

$\bigcirc$ Reference 13

$M_\infty = 1.61$, $\alpha_f = 4°$

$Y_B = -6.6$ inches

$z_B = 1.41$ inches

σ_ℓ, deg. (positive inboard)

x_B, inches
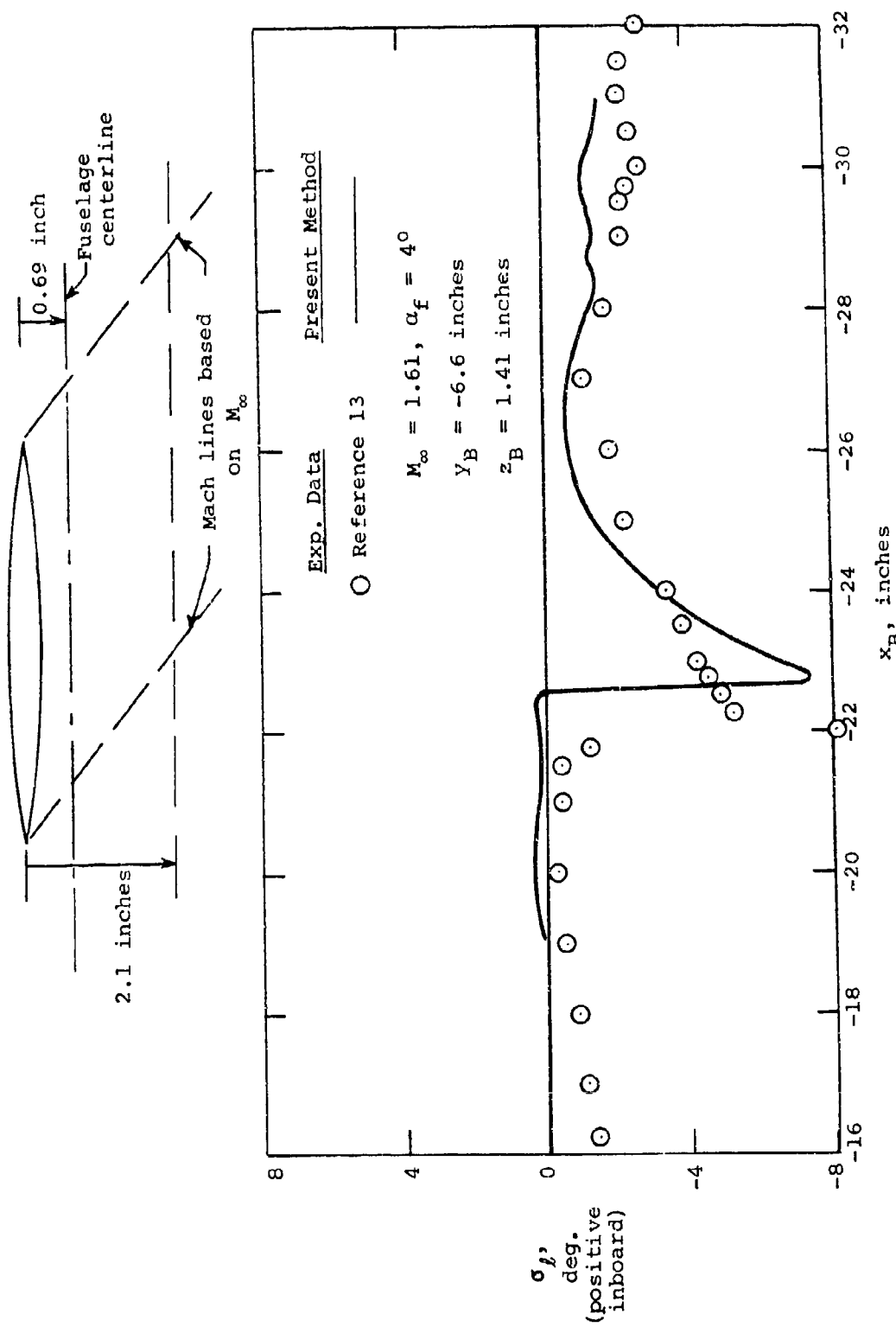
(a) Local sidewash angle.

Figure 18.- Flow field under sharp-edged trapezoidal wing-fuselage configuration, $\alpha_f = 4°$.

88
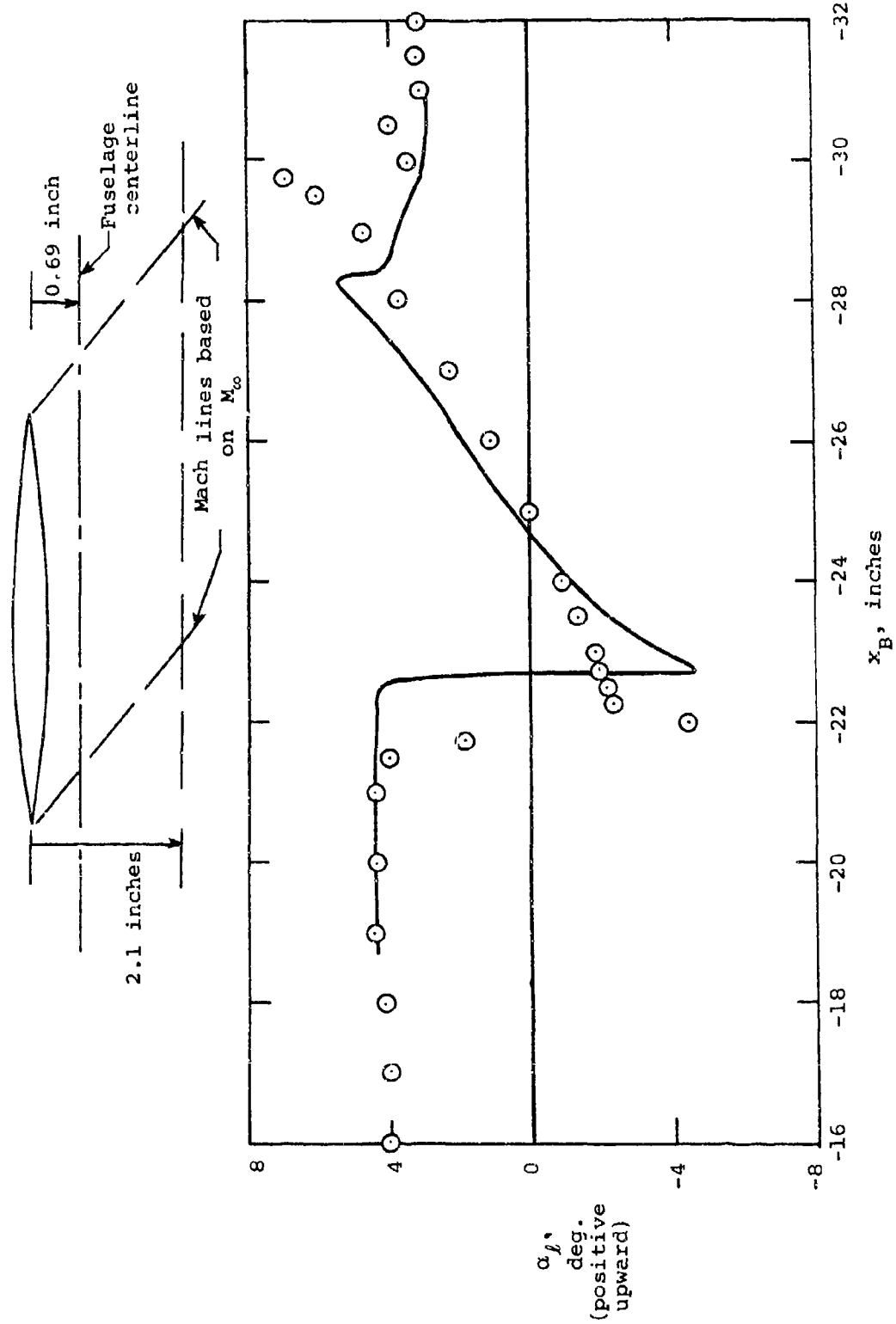
(b) Local upwash angle.

Figure 18.- Concluded.

89

Mach lines based
on M_∞

Exp. Data	Present Method
O Pylon off	— — —
□ Pylon on	———

$M_\infty = 2.0$, $\alpha_f = 0^\circ$

$y_B = -4.0$ inches

$z_B = -1.37$ inches
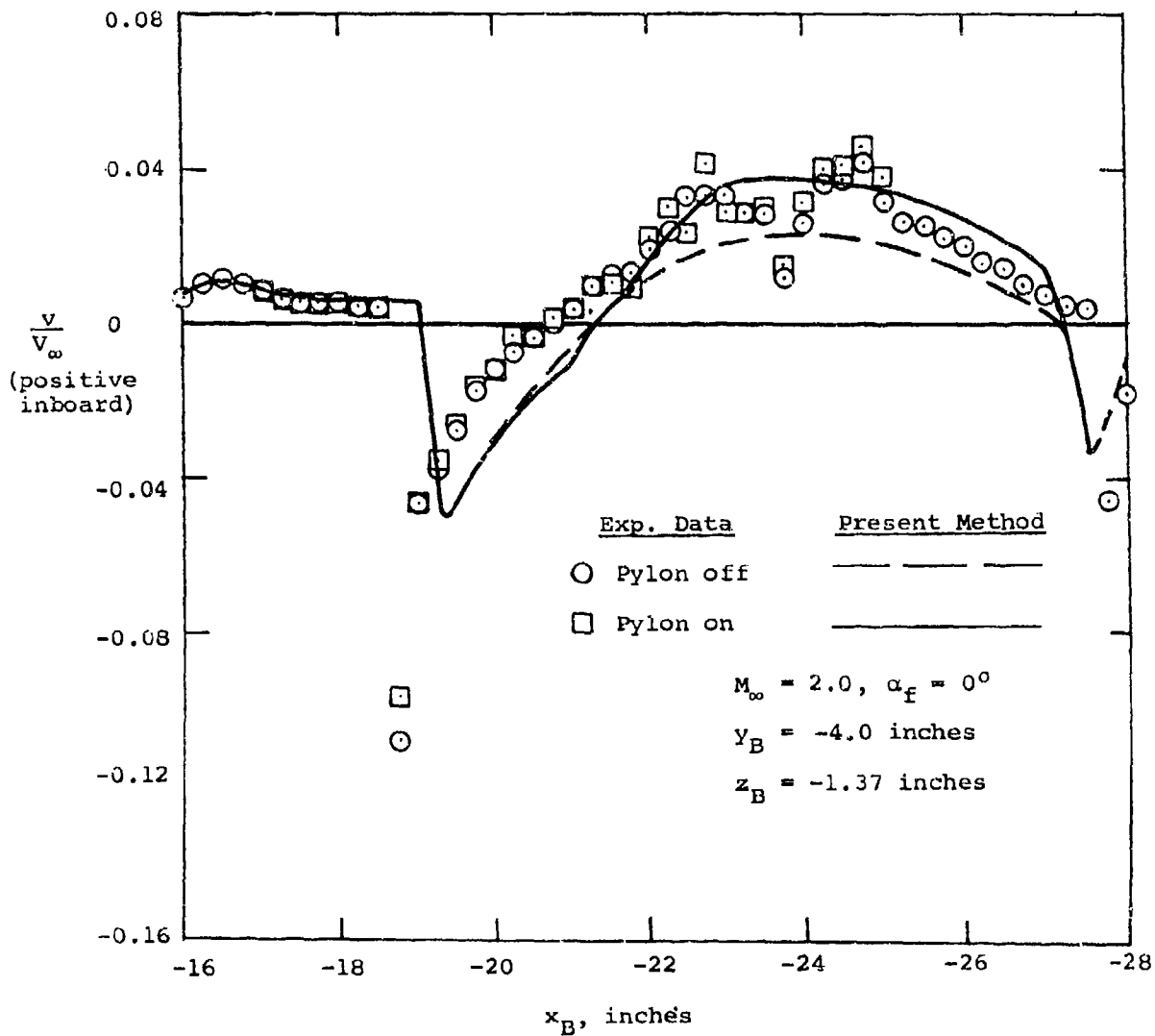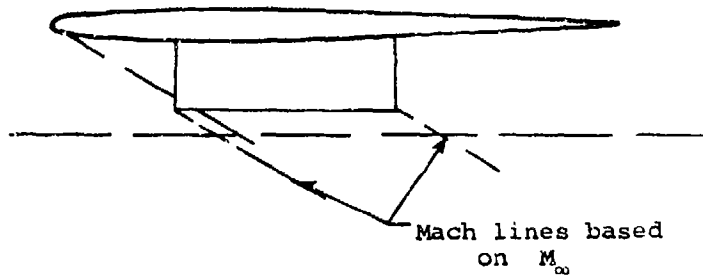
(a) Sidewash.

Figure 19.- Effect of the pylon on the flow field under the wing
at the one-third semispan location, $\alpha_f = 0^\circ$.

Mach lines based
on M_∞

$\frac{w}{V_\infty}$
(positive
upward)

x_B, inches
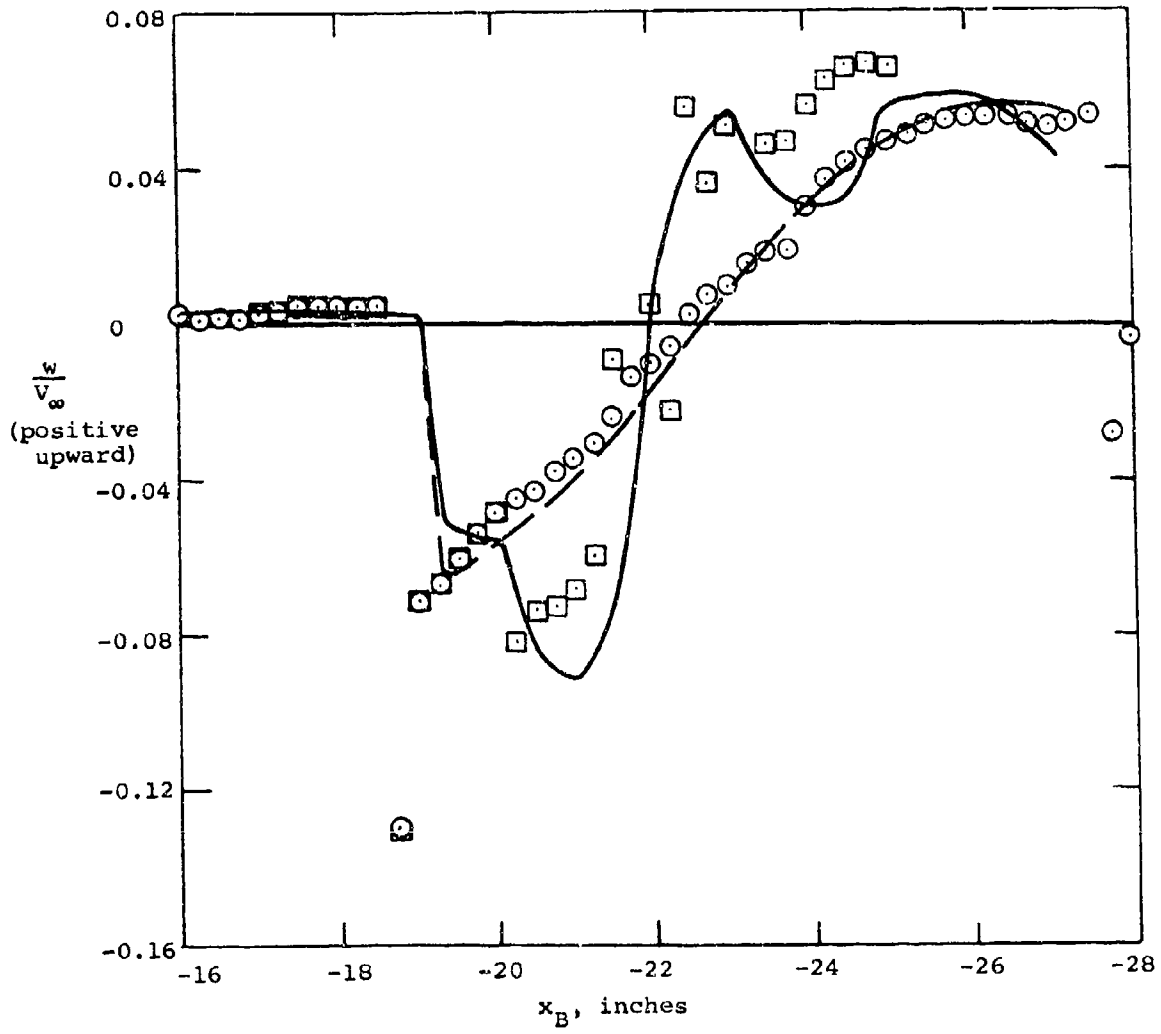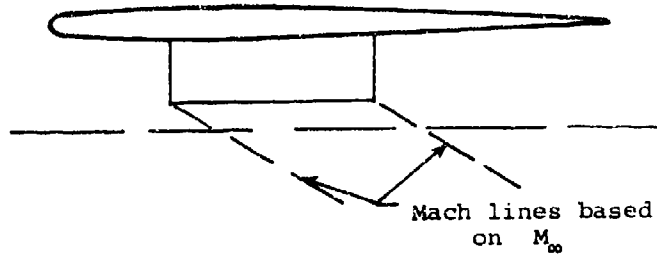
(b) Upwash.

Figure 19.- Concluded.

91

Mach lines based on M_∞

Exp. Data | Present Method
O Pylon off | — — —
□ Pylon on | ———

$M_\infty = 2.0$, $\alpha_f = 5^0$

$Y_B = -4.0$ inches

$z_B = 1.37$ inches

$\dfrac{v}{V_\infty}$ (positive inboard)

x_B, inches
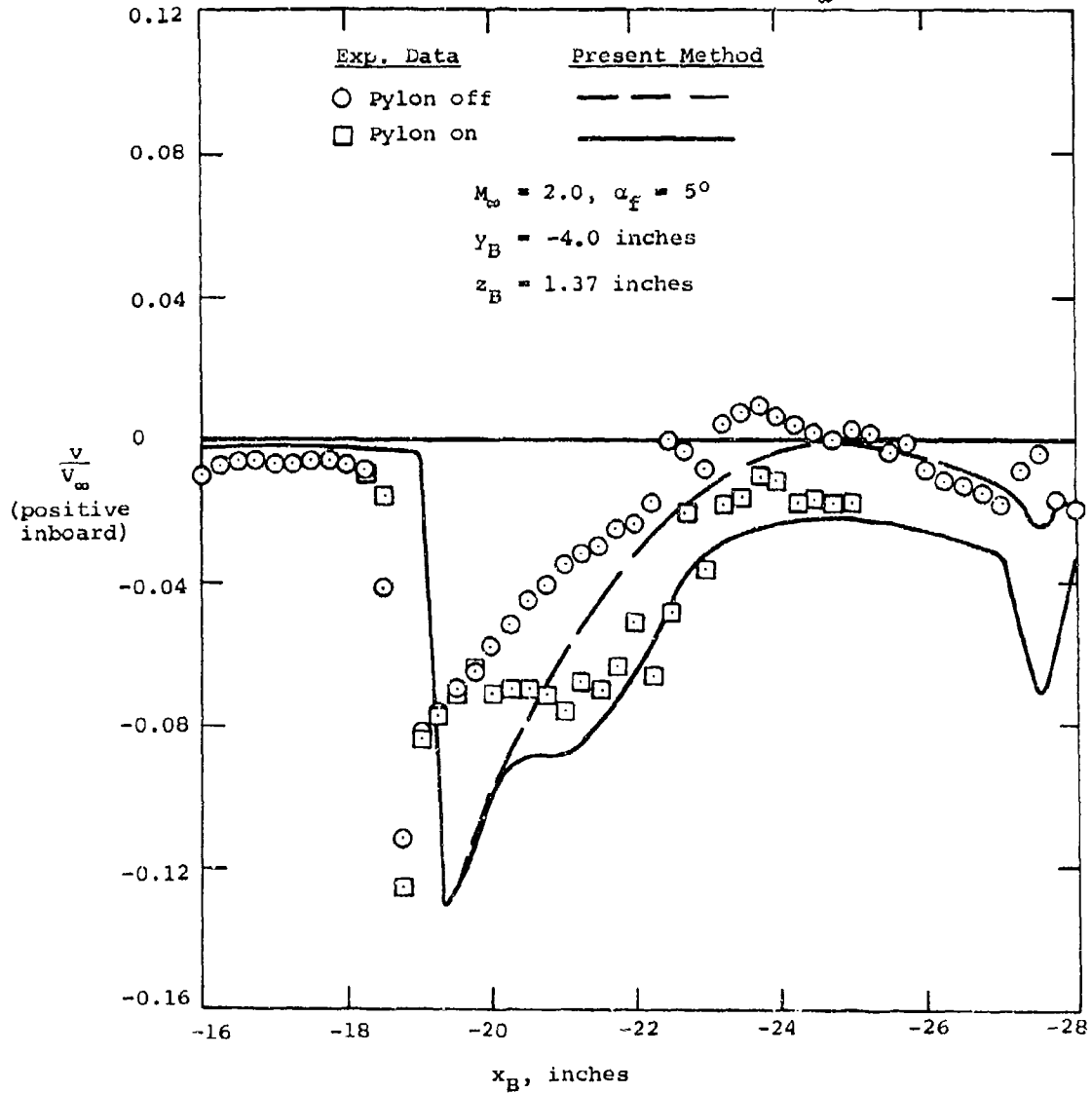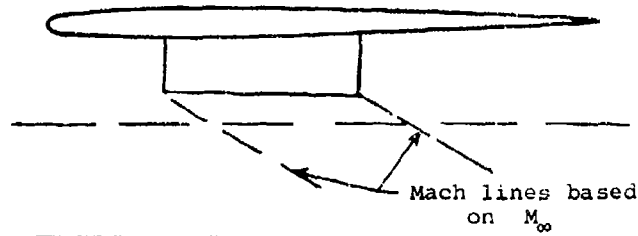
(a) Sidewash.

Figure 20.- Effect of the pylon on the flow field under the wing at the one-third semispan location, $\alpha_f = 5^0$.
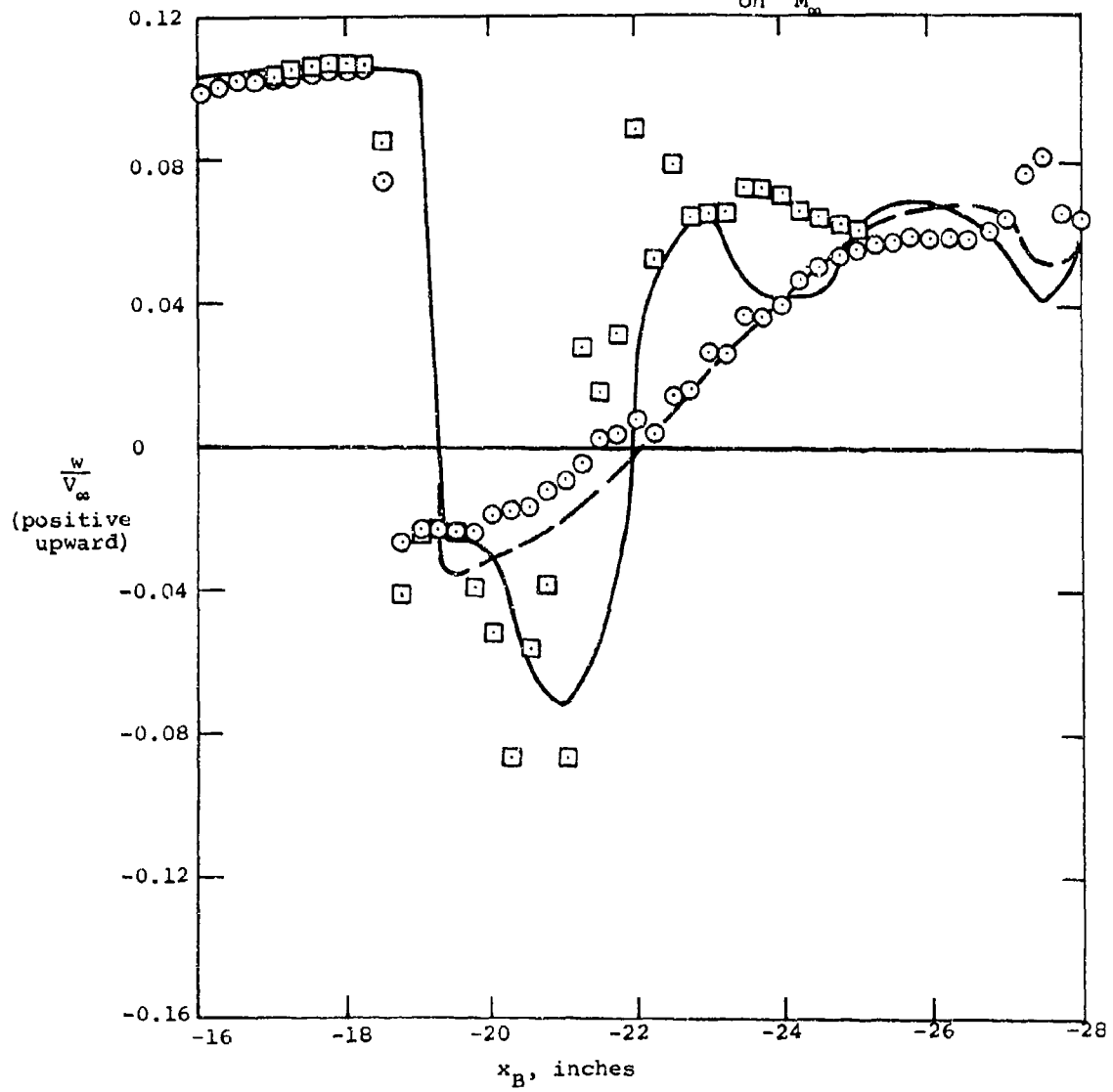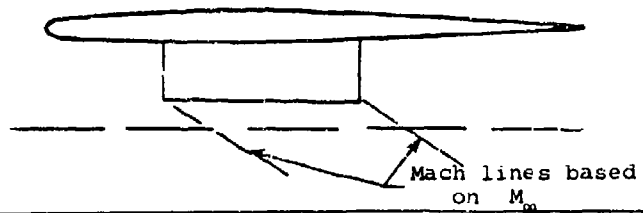
(b) Upwash.

Figure 20.- Concluded.

1.37 inches

Mach lines based
on M_∞

$\frac{v}{V_\infty}$
(positive
inboard)

Exp. Data   Present Method

O

$M_\infty = 2.5$, $\alpha_f = 0^0$

$Y_B = -4.0$ inches

$z_B = 1.37$ inches

x_B, inches
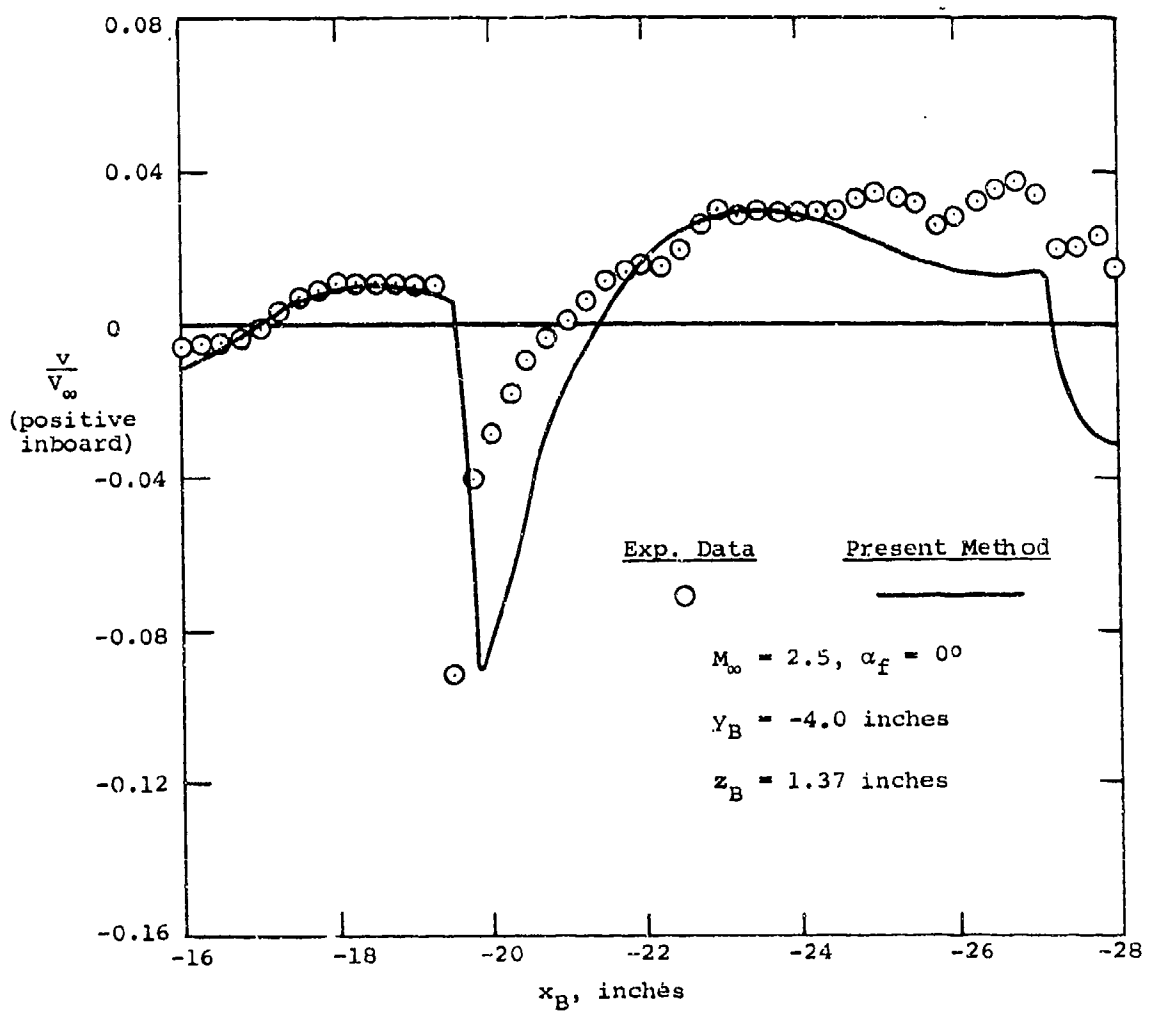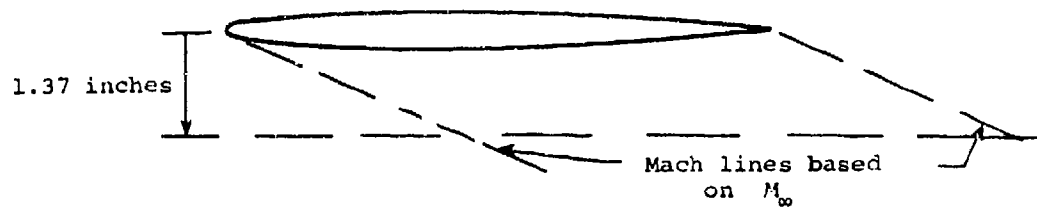
(a) Sidewash.

Figure 21.- Flow field under the wing at
the one-third semispan location, $\alpha_f = 0^0$.

94

1.37 inches

Mach lines based on M_∞
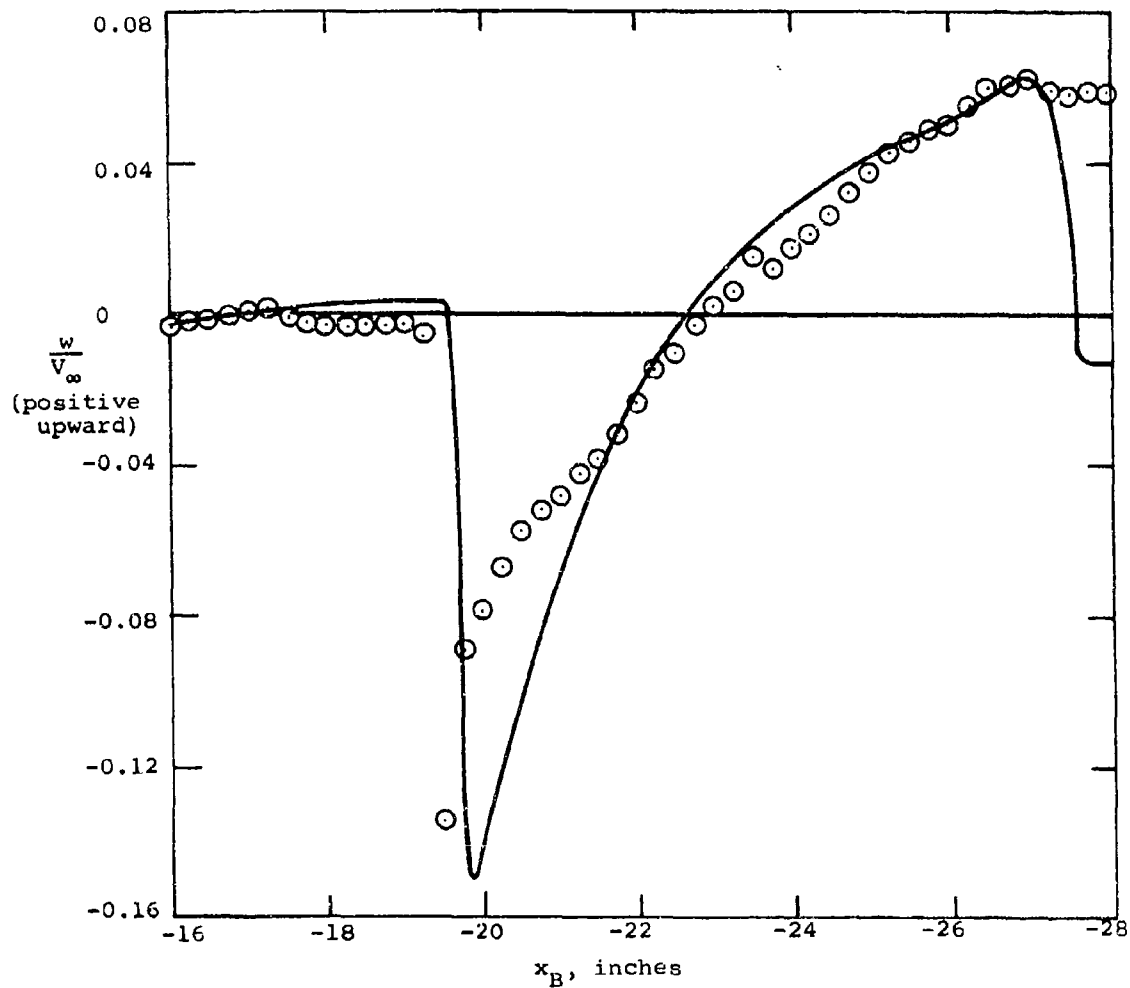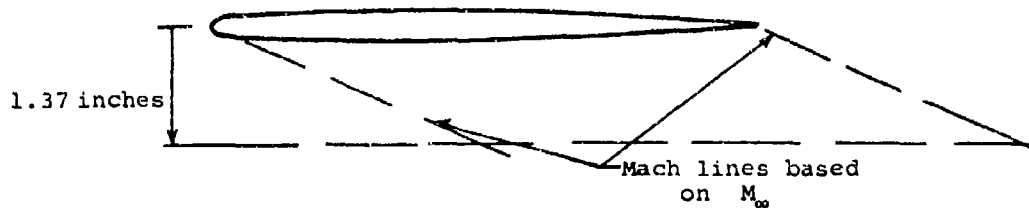
(b) Upwash.

Figure 21.- Concluded.

95

(a) Sidewash.
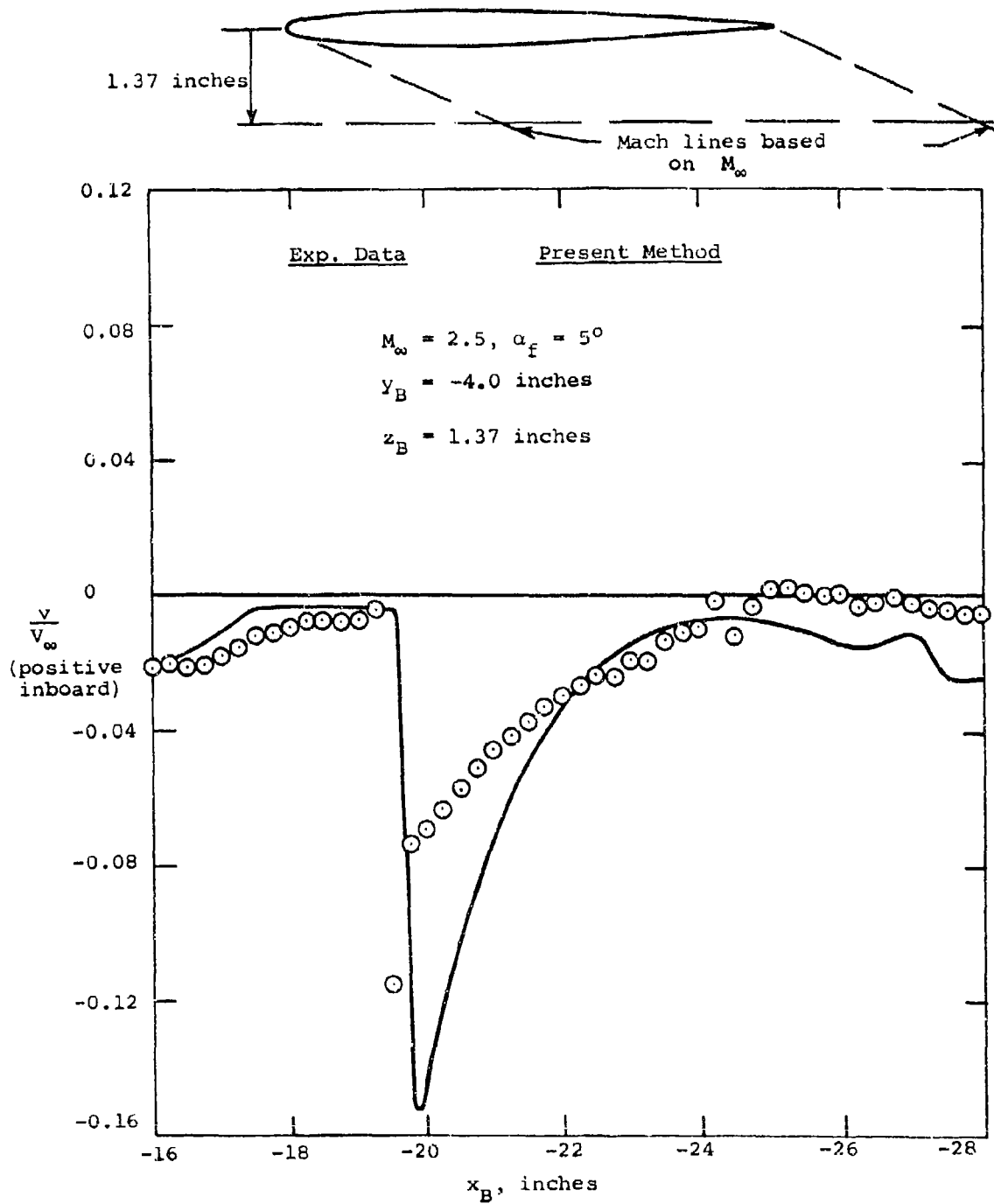
Figure 22.- Flow field under the wing at the
one-third semispan location, $\alpha_f = 5°$.

96

1.37 inches

Mach lines based on M_∞

$\frac{w}{V_\infty}$ (positive upward)

x_B, inches
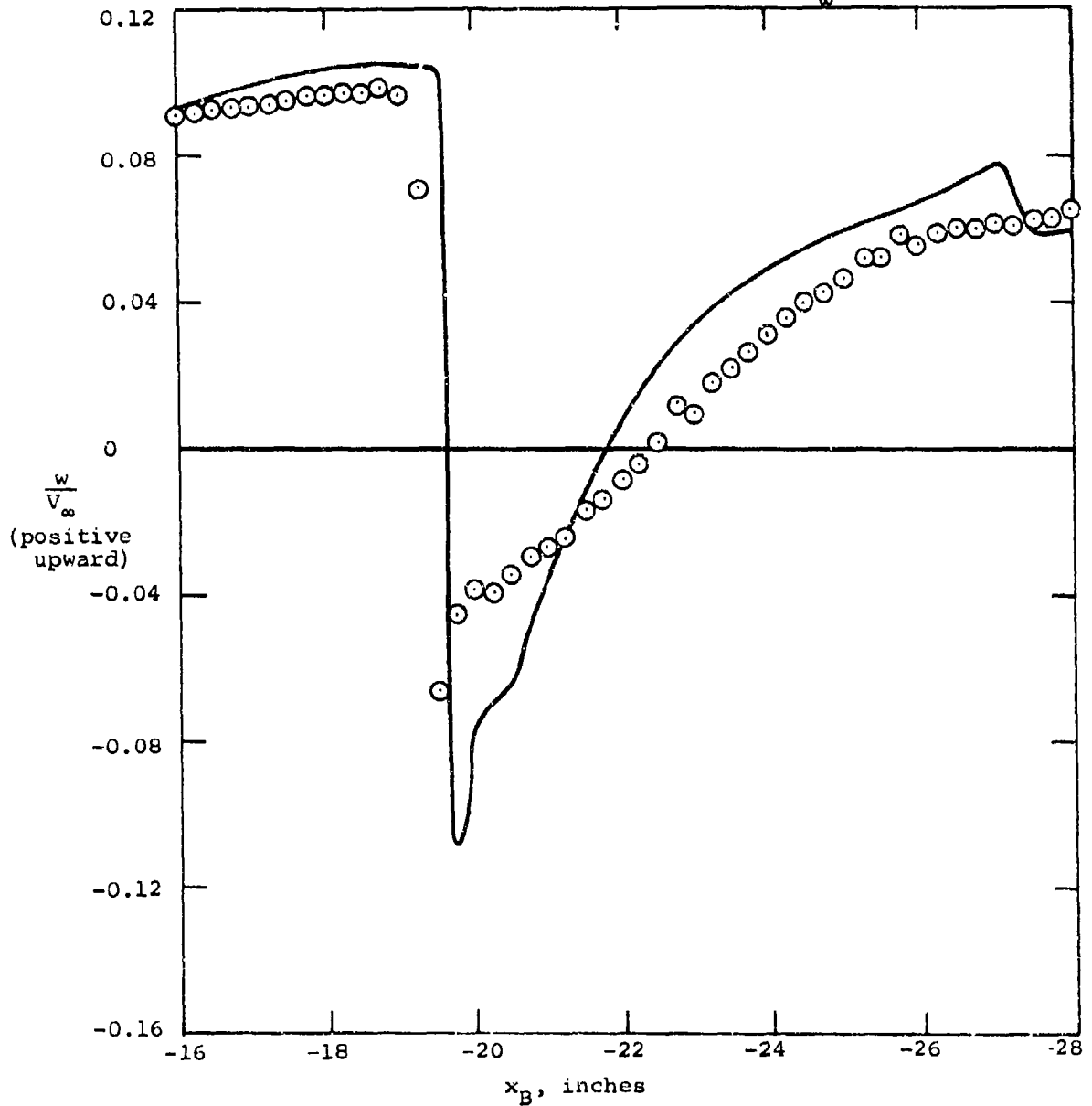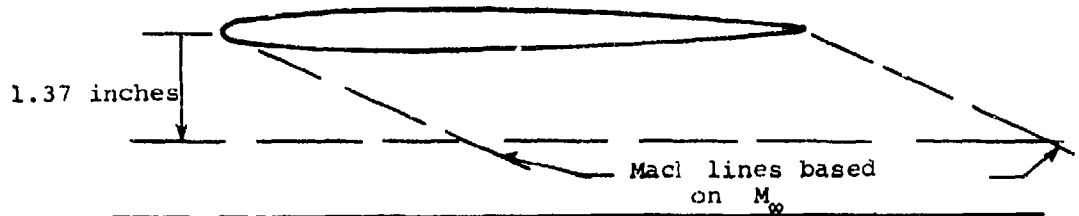
(b) Upwash.

Figure 22.- Concluded.

97
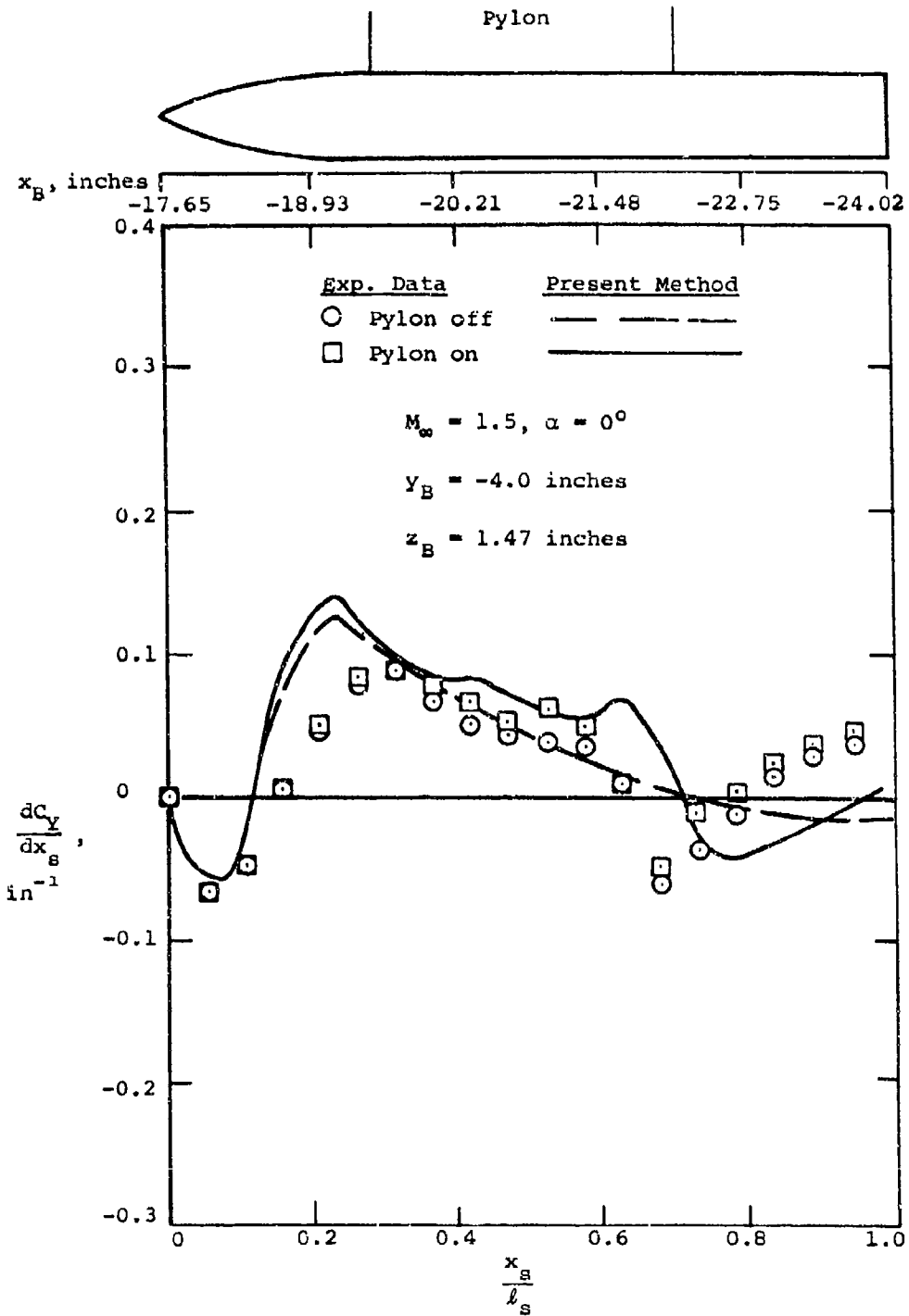
(a) Side force.

Figure 23.- Effect of the pylon on load
distribution of attached store.
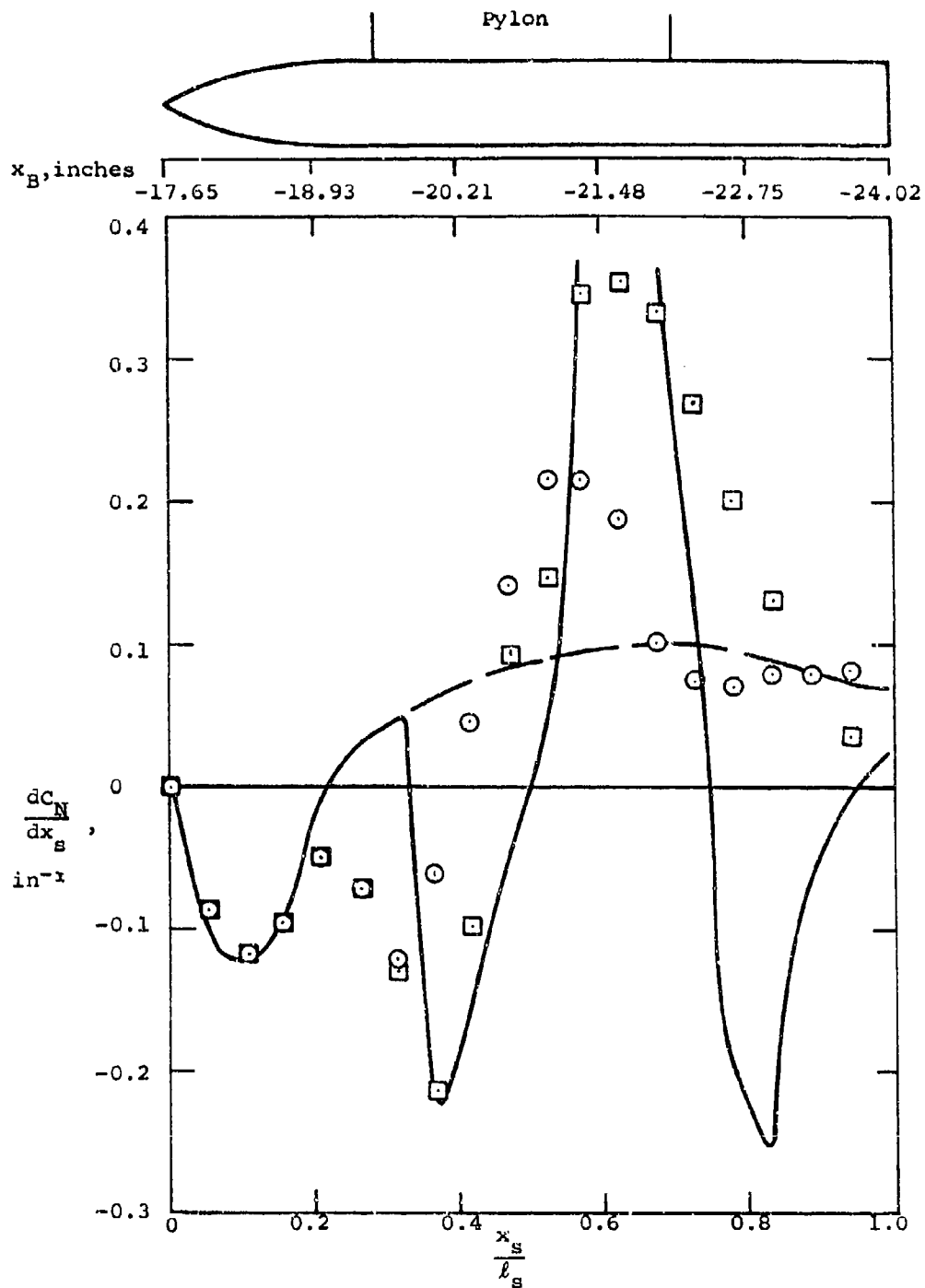
(b) Normal force.

Figure 23 - Concluded.

99
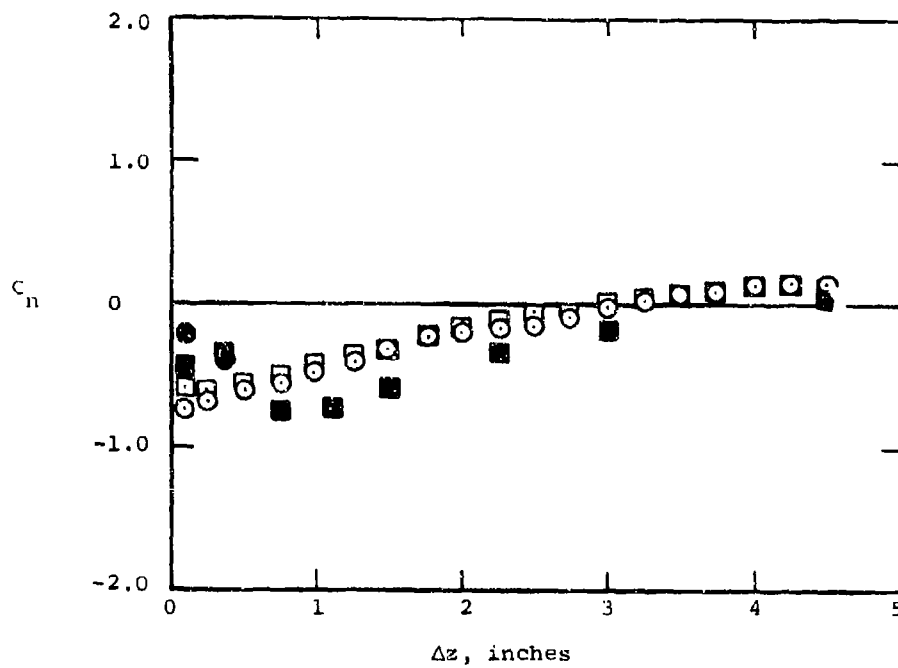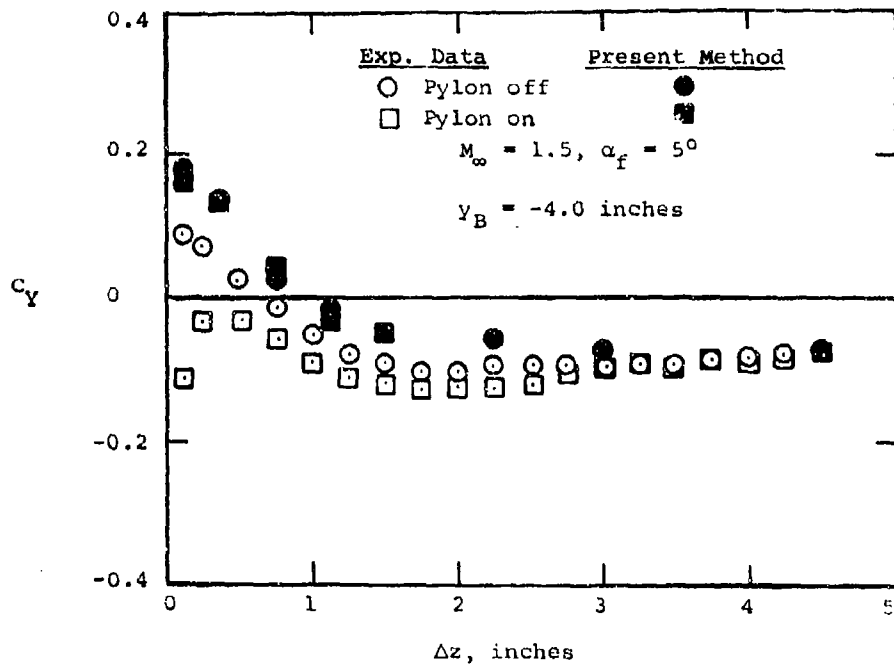
(a) Side force and yawing moment.

Figure 24.- Effect of vertical distance on store
forces and moments, $M_\infty = 1.5$.

100
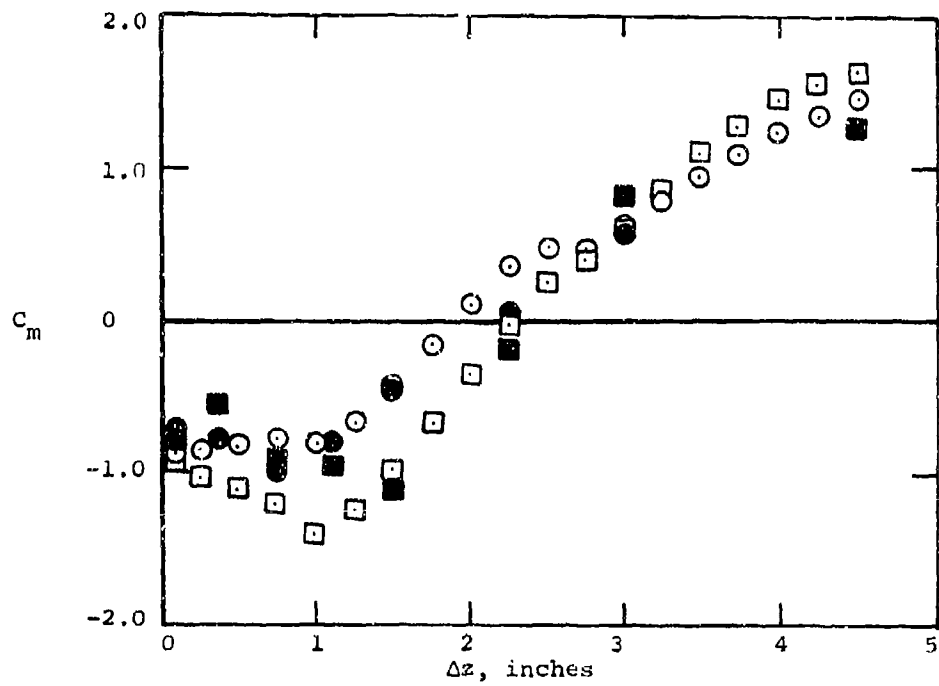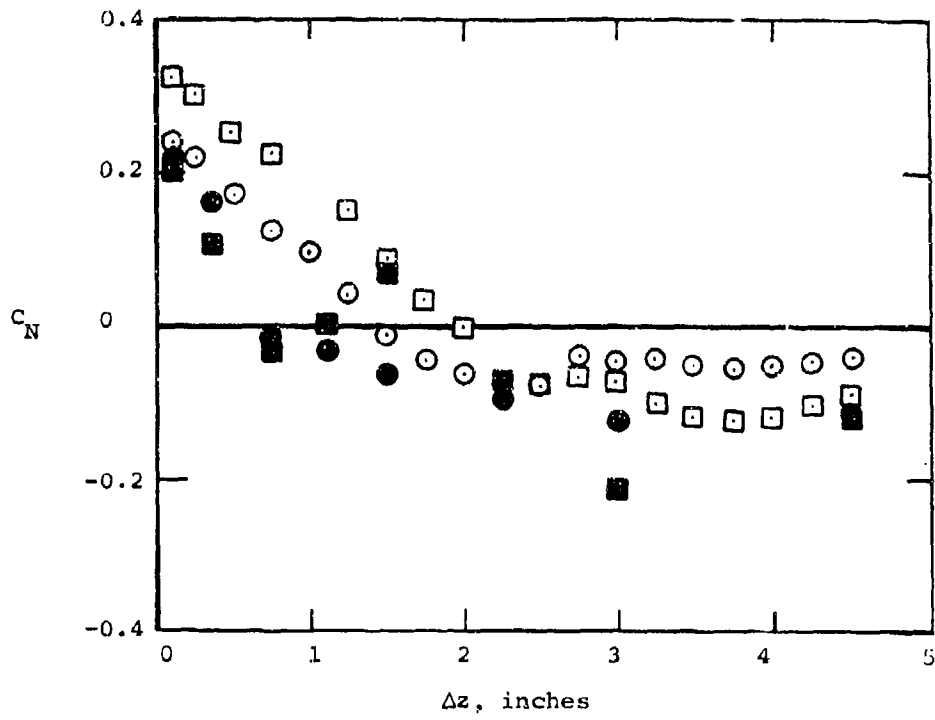
(b) Normal force and pitching moment.

Figure 24.- Concluded.
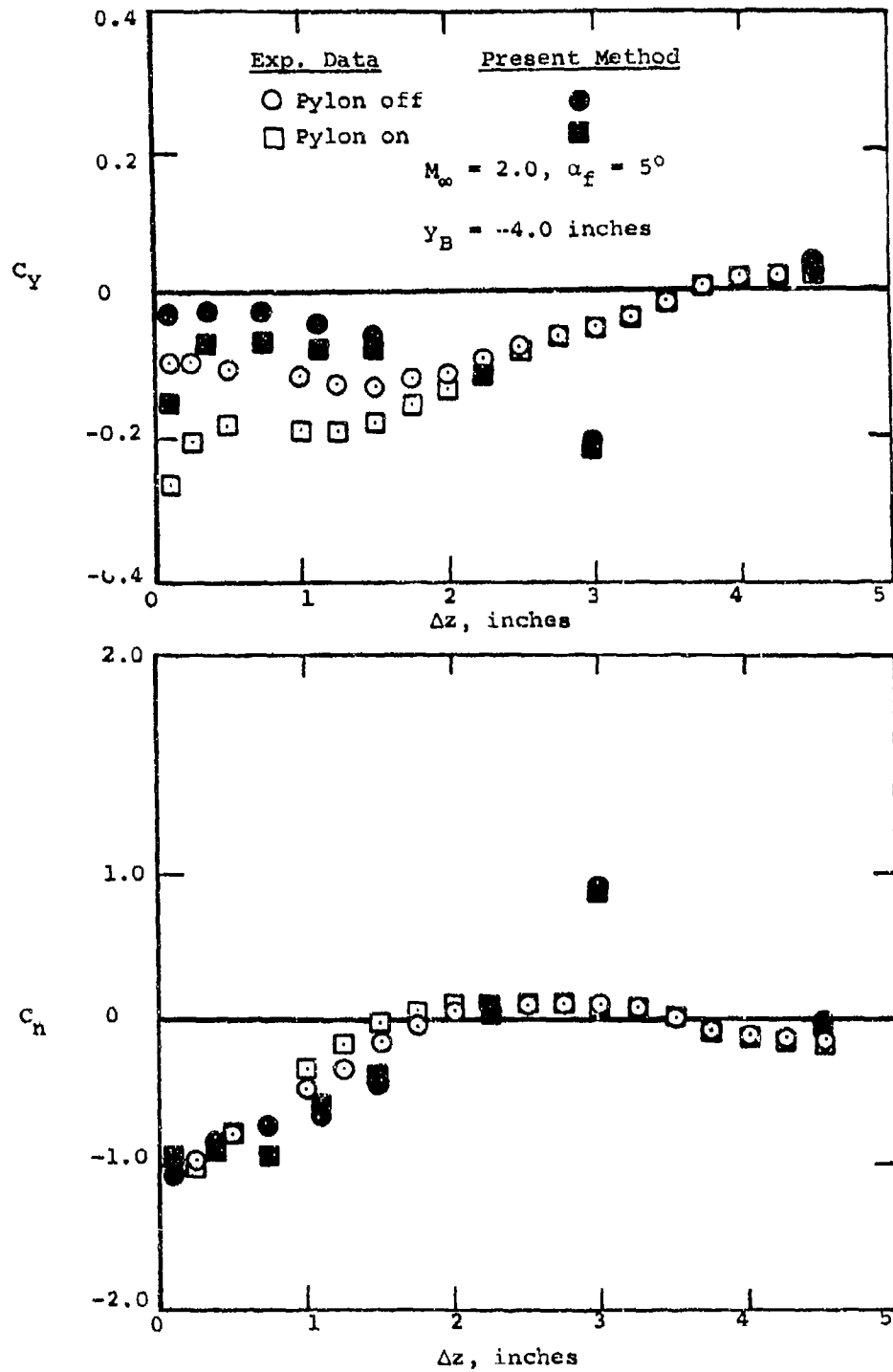
(a) Side force and yawing moment.

Figure 25.- Effects of vertical distance on store
forces and moments, $M_\infty = 2.0$.

102
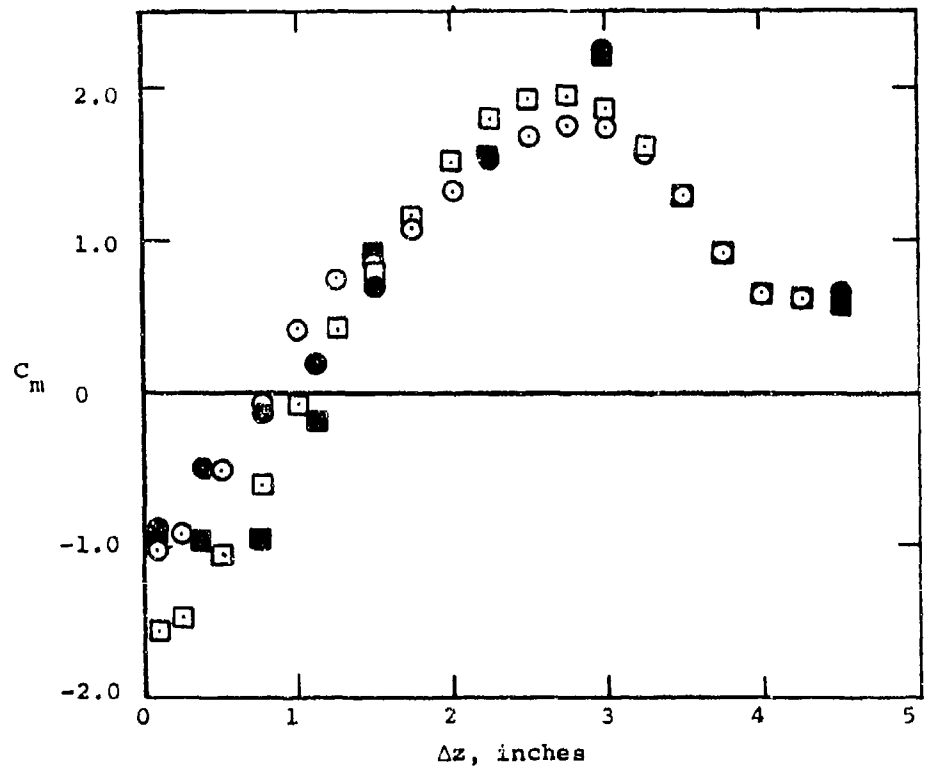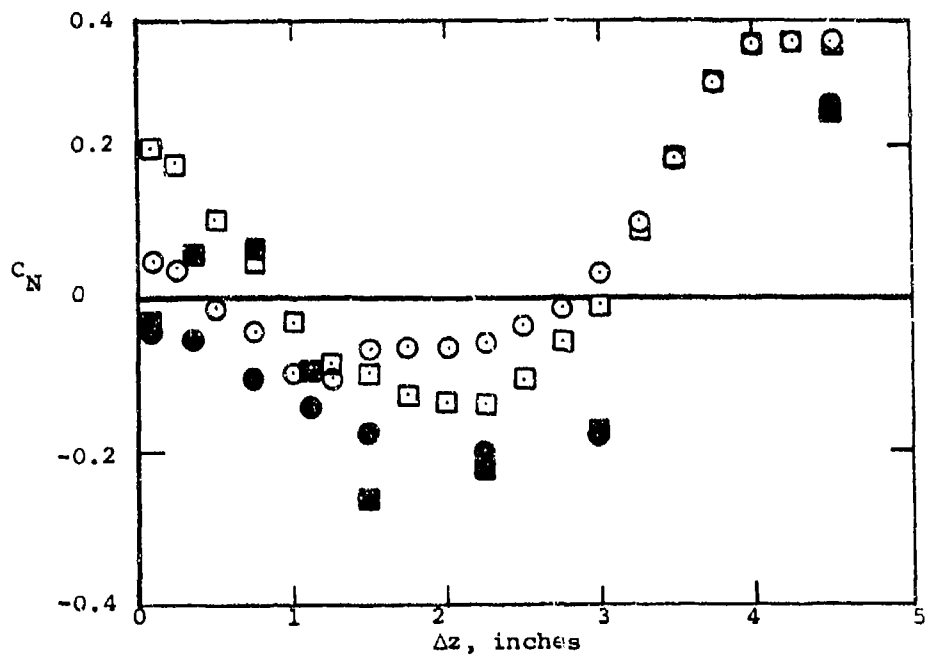
(b)   Normal force and pitching moment.

Figure 25.- Concluded.
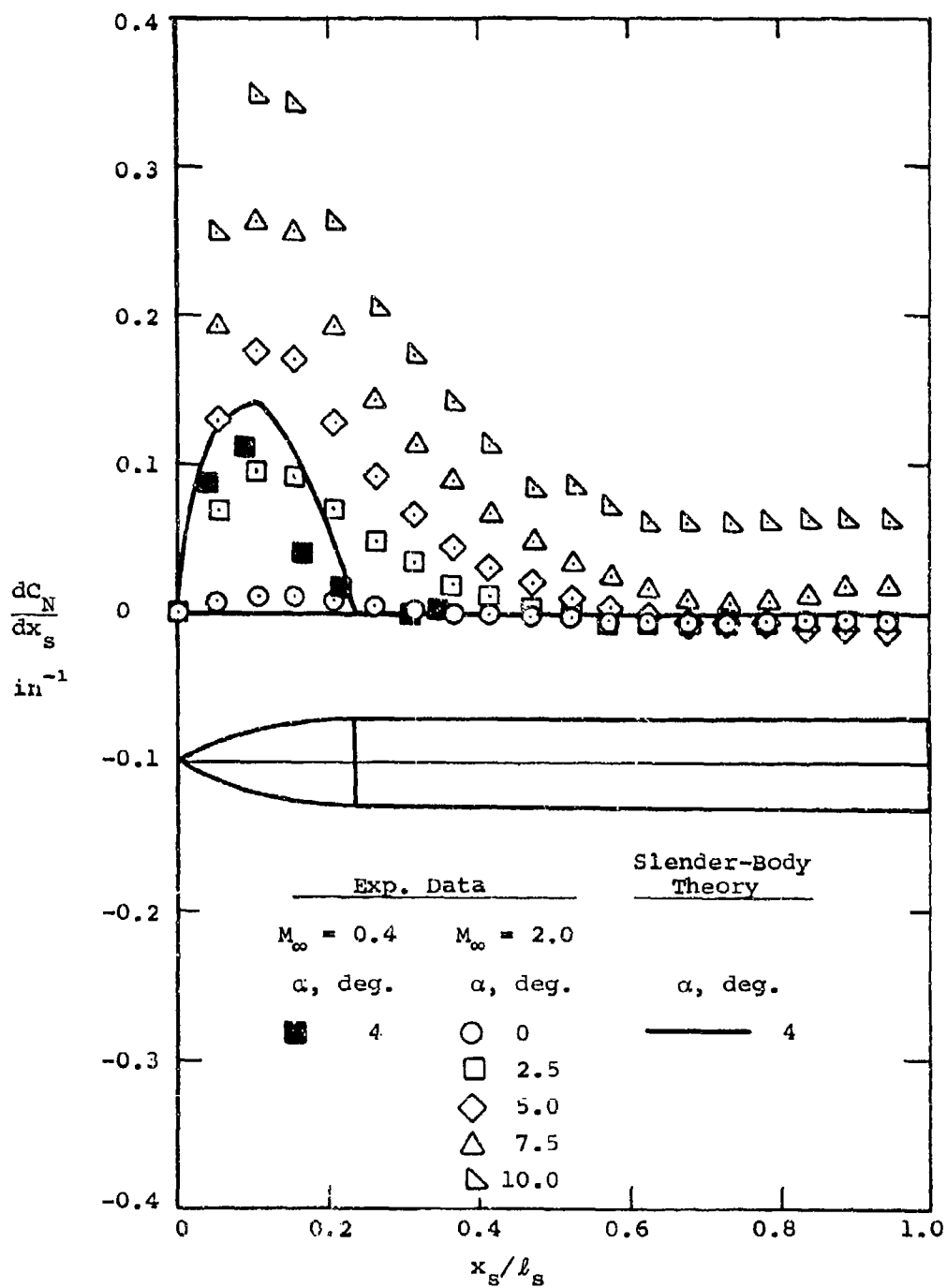
Figure 26.- Normal-force distribution along finless store in uniform flow.
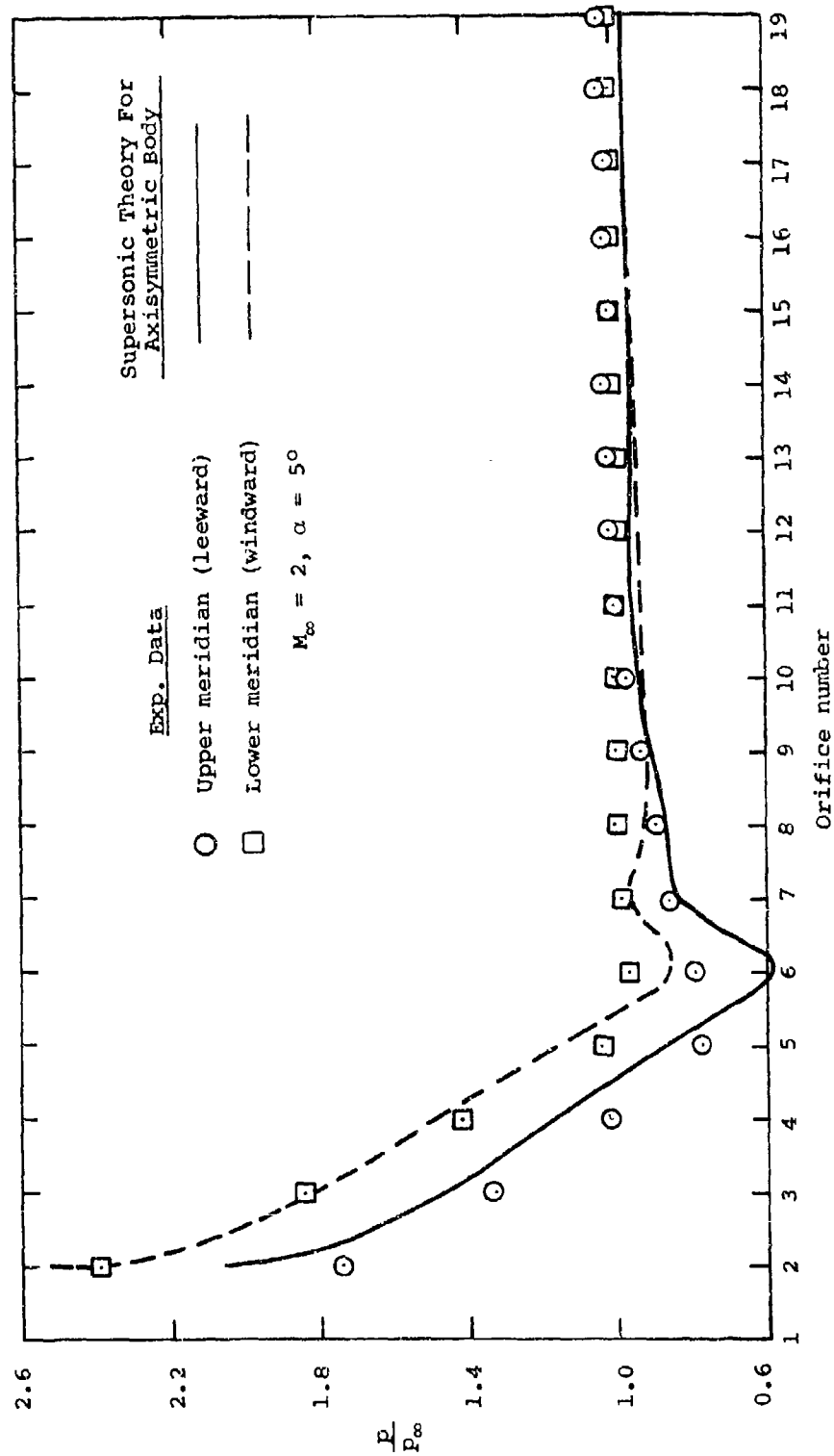
Figure 27.- Pressure distributions along upper and lower meridians of the pressure distribution store model in uniform flow.

105

APPENDIX I

BODY OF REVOLUTION IN SUPERSONIC FLOW

I-1. INTRODUCTION

Although the basic underlying theory is well known, this appendix summarizes the theoretical analysis used to model the flow around an axi-symmetric body in supersonic flow for the sake of completeness. The method makes use of linear, potential flow theory. It is shown in the main text of this report that the problem can be split in two separate problems: a body of revolution in axial flow and a body of revolution in crossflow. The following discussion is concerned with the type of singularities chosen for each problem and the determination of the constants in the distribution of the strengths of the singularities from the flow tangency boundary conditions. References are made to equation numbers in the main text of this report.

The theory described here has been collected from references 6 and 7. Reference 8 describes an early application of the axial flow part of the solution to the calculation of pressures on the nose of a projectile.

I-2. CHOICE OF SINGULARITIES

I-2.1 The Axial Flow Problem

The axial flow potential ϕ_a is governed by equation (5) after omitting the angular dependence term.

$$\frac{\partial^2 \phi_a}{\partial r_B^2} + \frac{1}{r_B} \frac{\partial \phi_a}{\partial r_B} - (M_\infty^2 - 1) \frac{\partial^2 \phi_a}{\partial x_B^2} = 0 \tag{I-1}$$

The solution for this potential may be represented as an integral over an unknown distribution of sources along the body axis.

$$\phi_a(x_B, r_B) = -\int_0^{x_B - \beta r_B} \frac{f(\xi)}{\sqrt{(x_B - \xi)^2 - \beta^2 r_B^2}} \, d\xi \tag{I-2}$$

where

$$\beta^2 = M_\infty^2 - 1 \tag{I-3}$$

107

The unknown function $f(\xi)$ will be described later and ξ is a dummy variable. The meaning of the upper limit of integration is illustrated in the sketch below. The sources are distributed along the x_B axis from 0 to L. To obtain the value of ϕ_a at $P(x_B, r_B)$, it is only
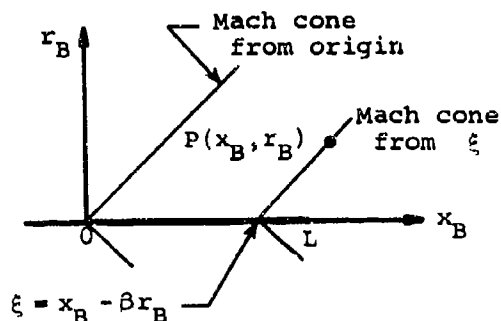
necessary to include sources only up to $\xi = x_B - \beta r_B$ since the sources downstream of this point have no effect on the conditions at $P(x_B, r_B)$. The perturbation velocities associated with the axial potential are obtained by taking derivatives of equation (I-2) in accordance with

$$\left. \begin{aligned} \frac{u_{B,a}}{V_\infty} &= \frac{\partial \phi_a}{\partial x_B} \\[2ex] \frac{v_{B,a}}{V_\infty} &= \frac{\partial \phi_a}{\partial r_B} \end{aligned} \right\} \tag{I-4}$$

Component $u_{B,a}$ is the perturbation velocity along the x_B axis and $v_{B,a}$ is positive outwards along a radial direction.

Since the variables x_B and r_B appear in the upper limit and the integrand in equation (I-2) becomes singular at the upper limit, it is convenient to change the variable of integration and apply Leibnitz's rule for differentiation under the integral sign. Following the procedure described in reference 6, put

$$\xi = x_B - \beta r_B \cosh \sigma \tag{I-5}$$

Then the axial potential can be rewritten as

$$\phi_a(x_B, r_B) = -\int_0^{\cosh^{-1}(x_B/\beta r_B)} f(x_B - \beta r_B \cosh \sigma)\, d\sigma \tag{I-6}$$

108

Consequently, from equation (I-4) the perturbation velocities induced by the axial potential are given by

$$\left.\begin{array}{l} \dfrac{u_{B,a}}{V_\infty} = -\displaystyle\int_0^{\cosh^{-1}(x_B/\beta r_B)} f'(x_B - \beta r_B \cosh \sigma)\, d\sigma \\[30pt] \dfrac{v_{B,a}}{V_\infty} = -\displaystyle\int_0^{\cosh^{-1}(x_B/\beta r_B)} f'(x_B - \beta r_B \cosh \sigma)(-\beta \cosh \sigma)\, d\sigma \end{array}\right\} \qquad (I\text{-}7)$$

where f' denotes differentiation of function f with respect to its argument. It has been assumed that $f(0) = 0$. Later it will be shown that this condition corresponds to bodies with pointed noses.

A particular simple and useful function is the one associated with a line source.

$$\left.\begin{array}{l} f(\xi) = K\xi \\[10pt] f(0) = 0, \quad f'(\xi) = K \end{array}\right\} \qquad (I\text{-}8)$$

Substituting this function into equation (I-6) and using equation (I-5) for ξ gives

$$\phi_a(x_B, r_B) = -Kx_B\left[\cosh^{-1}\left(\frac{x_B}{\beta r_B}\right) - \sqrt{1 - \left(\frac{\beta r_B}{x_B}\right)^2}\,\right] \qquad (I\text{-}9)$$

The associated perturbation velocities can be found by direct differentiation in accordance with equation (I-4).

$$\left.\begin{array}{l} \dfrac{u_{B,a}}{V_\infty} = -K\cosh^{-1}\left(\dfrac{x_B}{\beta r_B}\right) \\[18pt] \dfrac{v_{B,a}}{V_\infty} = K\beta\sqrt{\left(\dfrac{x_B}{\beta r_B}\right)^2 - 1} \\[18pt] \dfrac{w_{B,a}}{V_\infty} = 0 \end{array}\right\} \qquad (I\text{-}10)$$

109

Both nonzero velocities are functions of parameter $x_B/\beta r_B$. Thus, they are invariant along lines for which x_B/r_B is constant; that is, along rays from the origin. The flow field described by equation (I-10) is called conical. For a cone with vertex angle δ_{cone}, reference 6 relates the constant K to the angle through

$$K = \frac{\tan \delta_{cone}}{\sqrt{\cot^2 \delta_{cone} - \beta^2} + \tan \delta_{cone} \cosh^{-1}\left(\frac{\cot \delta_{cone}}{\beta}\right)} \qquad (I-11)$$

The conical flow field is shown in the following sketch. Velocities $u_{B,a}$ and $v_{B,a}$ are constant along the rays from the origin. On the Mach cone the perturbation velocities are zero and the flow is still parallel to the free stream. Two streamlines are shown, one originating in the free stream and one emanating from a point on the line source along the axis. Any streamline can represent a solid surface, but there is only
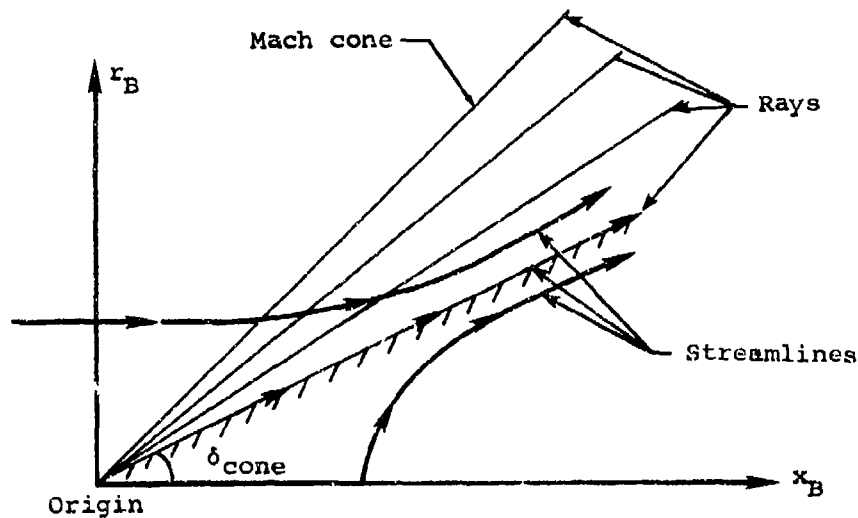
one streamline coincident with a ray. A cone containing that ray represents a solid cone in supersonic flow at least within the constraints of linear theory. The flow field associated with this cone is specified by equation (I-10) with equation (I-11).

The axial flow around an arbitrary but pointed body of revolution aligned with the flow can be obtained by a superposition of conical solutions of the type discussed above since the starting procedure is clear. The procedure is indicated in the following sketch. For the

110

ogive shape shown below, the composite source distribution for the axial flow solution is obtained by generating a superposition of linearly varying sources; that is, a superposition of cone solutions.

$$f(\xi) = K_0 \xi + K_1 (\xi - \xi_1) + K_2 (\xi - \xi_2) + \ldots \tag{I-12}$$
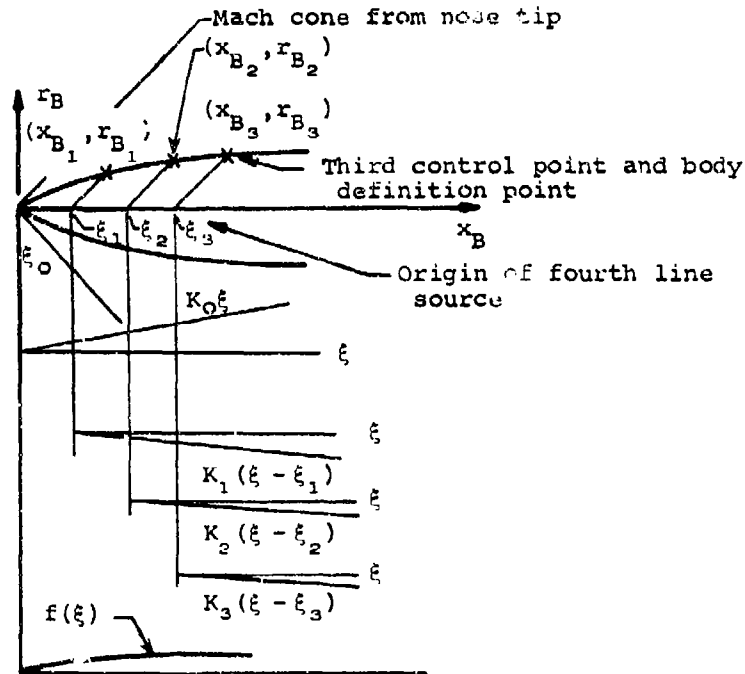
Constants $K_1, K_2,$ and K_3 are negative for the example in the sketch above, and $\xi_0 = 0$, $\xi_1 = x_{B_1} - \beta r_{B_1}$, $\xi_2 = x_{B_2} - \beta r_{B_2}$, etc., are the origins of the line singularities. The constants can be evaluated in a step-by-step manner as follows. The constant K_0 corresponds to the solution which satisfies the flow tangency condition at (x_{B_1}, r_{B_1}) and gives the flow near the nose tip. At the next control point on the body, it is necessary to superimpose another conical solution with its origin located at $\xi_1 = x_{B_1} - \beta r_{B_1}$ and its constant K_1 is chosen so that the flow tangency condition on the body at point (x_{B_2}, r_{B_2}) is satisfied. The second solution does not affect the nose flow ahead of the Mach cone with its origin at ξ_1. It should be noted here that this particular property is characteristic of solutions to the wave equation given by (I-1). Let NXBODY be the number of line sources with origins equally spaced on the body centerline. As a result, the number of control points equals NXBODY.

111

The superposition scheme for representing a body of revolution in supersonic flow is applicable only if the body meridianal section is smooth. For bodies with corners, additional solutions, such as Prandtl-Meyer expansion theory, are required to properly account for the flow near the shoulders. The layout of the body definition points and control points as shown in the preceeding sketch is used in the body flow modeling program of references 9 and 20. Following a suggestion by R. C. Carmichael of NASA/Ames Research Center associated with reference 21, the control points can be shifted forward a half-space, $\Delta x_B/2$. This modification tends to smooth the solution. The modified layout of the body definition and control points is indicated in the following sketch. In this case, the number of line sources NXBODY equals the number of control points.
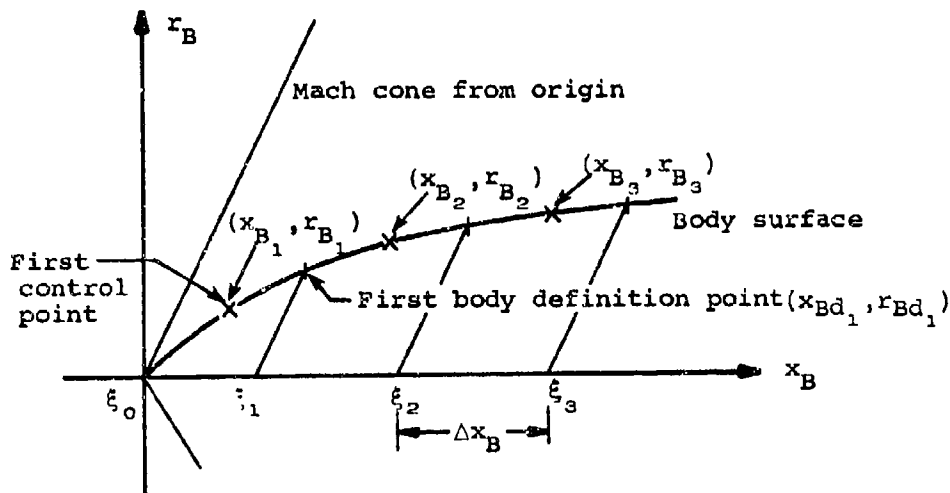
The flow tangency boundary condition for the axial flow problem given by equation (8a) can be rewritten as follows.

$$\left. \frac{\dfrac{dR}{dx_B}}{\dfrac{v_{B,a}}{V_\infty} - \dfrac{u_{B,a}}{V_\infty}\dfrac{dR}{dx_B}} \right|_{\substack{\text{first control} \\ \text{point}}} = 1 \qquad (I\text{-}13)$$

Substituting from equation (I-10) then gives

112

$$K_O = \left. \frac{\frac{dR}{dx_B}}{\beta\sqrt{\left(\frac{x_B}{\beta r_B}\right)^2 - 1} + \left[\cosh^{-1}\left(\frac{x_B}{\beta r_B}\right)\right]\frac{dR}{dx_B}} \right|_{\substack{x_B = x_{B_1} = (\Delta x_B/2) \\ r_B = r_{B_1} = R(x_{B_1})}}$$

(I-14)

where $x_{B_1}^-$ and r_{B_1} are the coordinates of the first control point.

With K_O known, the second constant K_1 can now be explicitly determined from boundary condition (8a) applied to the second control point (x_{B_2}, r_{B_2}) on the body surface.

$$K_1 = \frac{a}{b}$$

$$a = \left.\frac{dR}{dx_B}\right|_2 - K_O\left\{\beta\sqrt{\left(\frac{x_{B_2} - \xi_O}{\beta r_{B_2}}\right)^2 - 1} + \left[\cosh^{-1}\left(\frac{x_{B_2} - \xi_O}{\beta r_{B_2}}\right)\right]\left.\frac{dR}{dx_B}\right|_2\right\}$$

$$b = \beta\sqrt{\left(\frac{x_{B_2} - \xi_1}{\beta r_{B_2}}\right)^2 - 1} + \left[\cosh^{-1}\left(\frac{x_{B_2} - \xi_1}{\beta r_{B_2}}\right)\right]\left.\frac{dR}{dx_B}\right|_2$$

(I-15)

The terms in the above expression are given by

$$\xi_O = 0$$

$$\xi_1 = x_{Bd_1} - \beta r_{Bd_1}$$

$$x_{B_2} = x_{B_1} + \Delta x_B$$

$$\Delta x_B = \frac{\text{body length}}{\text{XBODY}}$$

(I-16)

(Continued on next page)

113

$$r_{B_2} = R(x_{B_2}) \ \dots \ \text{specified}$$

$$\left. \frac{dR}{dx_B} \right|_2 = R'(x_{B_2})$$

(I-16)

(Concluded)

where $R(x_B)$ is a prescribed function of the body contour in the meridian plane according to equation (3) and R' is its derivative. Continuing this step-by-step procedure results in the following general expression for the nth constant determined from the boundary condition applied at the $(n+1)^{th}$ control point $(x_{B_{n+1}}, r_{B_{n+1}})$.

$$a = \left.\frac{dR}{dx_B}\right|_{n+1} - \sum_{k=1}^{n} K_{k-1} \left\{ \beta\sqrt{\left(\frac{x_{B_{n+1}} - \xi_{k-1}}{\beta r_{B_{n+1}}}\right)^2 - 1} \right.$$

$$\left. + \left[\cosh^{-1}\left(\frac{x_{B_{n+1}} - \xi_{k-1}}{\beta r_{B_{n+1}}}\right) \right] \left.\frac{dR}{dx_B}\right|_{n+1} \right\}$$

$$b = \beta\sqrt{\left(\frac{x_{B_{n+1}} - \xi_n}{\beta r_{B_{n+1}}}\right)^2 - 1} + \left[\cosh^{-1}\left(\frac{x_{B_{n+1}} - \xi_n}{\beta r_{B_{n+1}}}\right) \right] \left.\frac{dR}{dx_B}\right|_{n+1}$$

(I-17)

$$K_n = \frac{a}{b}$$

$$n = 1, 2, \dots (NXBODY-1)$$

The terms in the above equation are specified as follows:

$$\xi_o = 0$$

$$\xi_{k-1} = x_{Bd_{k-1}} - \beta r_{Bd_{k-1}} \ ; \ k = 2, 3, \dots$$

(I-18)

$$\xi_n = x_{Bd_n} - \beta r_{Bd_n}$$

114

$$x_{B_{n+1}} = x_{B_n} + \Delta x_B$$

$$\Delta x_B = \frac{\text{body length}}{\text{NXBODY}}$$

$$r_{B_{n+1}} = R(x_{B_{n+1}})$$

$$\left. \frac{dR}{dx_B} \right|_{n+1} = R'(x_{B_{n+1}})$$

(I-18)

(Concluded)

I-2.2 Crossflow Problem

The crossflow solution ϕ_c must satisfy equation (5) subject to the boundary condition given by equation (8b). It is readily shown that if ϕ_a is a solution to equation (I-1) then a solution to the full wave equation, equation (5), can be constructed as follows.

$$\phi_c(x_B, r_B, \theta) = \cos\theta \, \frac{\partial \phi_a}{\partial r_B} \tag{I-19}$$

Thus, a crossflow solution can be obtained readily from an axisymmetric solution. However, the one obtained from the axial potential ϕ_a as in equation (I-9) for the case in question is not the one sought here. Instead, the general form of an axisymmetric potential as given by equation (I-2) is retained. The desired solution for ϕ_c is given by the second expression in equation (I-7) since $v_{B,a}/V_\infty = (\partial \phi_a/\partial r_B)$. Rewriting in terms of the original variable ξ and substituting the differentiated form into (I-19), the result is

$$\phi_c(x_B, r_B, \theta) = \frac{\cos\theta}{r_B} \int_0^{x_B - \beta r_B} \frac{f'(\xi)(x_B - \xi)}{\sqrt{(x_B - \xi)^2 - \beta^2 r_B^2}} \, d\xi \tag{I-20}$$

The function $f'(\xi)$ is, so far, unknown and is to be determined from the flow tangency condition in the crossflow plane given by equation (8b). To avoid confusion with the function $f(\xi)$ used in the axial solution, set

115

$$d(\xi) = f(\xi) \qquad (\text{I-21})$$

since we are dealing now with a doublet distribution.

In accordance with the procedure shown in reference 7, the following linearly varying distribution is used for the doublet strength distribution as given by

$$d(\xi) = K_d \xi \qquad (\text{I-22})$$

Again, letting $\xi = x_B - \beta r_B \cosh \sigma$ as in equation (I-5), and carrying out the integration indicated by (I-20) results in a three-dimensional doublet solution

$$\phi_c(x_B, r_B, \theta) = K_d \cos\theta \left[\frac{x_B}{2r_B} \sqrt{x_B^2 - \beta^2 r_B^2} - \frac{\beta^2 r_B}{2} \cosh^{-1}\left(\frac{x_B}{\beta r_B}\right) \right] \qquad (\text{I-23})$$

Direct differentiation of the crossflow potential gives the perturbation velocities associated with the line doublet.

$$\left.\begin{array}{l}
\dfrac{u_{B,d}}{V_\infty} = \dfrac{\partial\phi_c}{\partial x_B} = K_d \beta \cos\theta \sqrt{\dfrac{x_B^2}{\beta^2 r_B^2} - 1} \\[4ex]
\dfrac{v_{B,d}}{V_\infty} = \dfrac{\partial\phi_c}{\partial r_B} = - K_d \dfrac{\beta^2 \cos\theta}{2} \left[\cosh^{-1}\left(\dfrac{x_B}{\beta r_B}\right) + \dfrac{x_B}{\beta r_B} \sqrt{\dfrac{x_B^2}{\beta^2 r_B^2} - 1} \right] \\[4ex]
\dfrac{w_{B,d}}{V_\infty} = \dfrac{1}{r_B}\dfrac{\partial\phi_c}{\partial\theta} = - \dfrac{K_d \sin\theta}{r_B} \left[\dfrac{x_B}{2r_B} \sqrt{x_B^2 - \beta^2 r_B^2} - \dfrac{\beta^2 r_B}{2} \cosh^{-1}\left(\dfrac{x_B}{\beta r_B}\right) \right]
\end{array}\right\} \qquad (\text{I-24})$$

The crossflow around an arbitrary body of revolution can be obtained by a superposition of doublet solutions in the same manner used for the axial flow problem. Thus, the composite doublet distribution for the crossflow solution is obtained by generating a superposition of linearly varying doublet distributions

$$d(\xi) = K_{d,o}\xi + K_{d,1}(\xi - \xi_1) + K_{d,2}(\xi - \xi_2) + \ldots \qquad (\text{I-25})$$

116

in terms of constants $K_{d,0}, K_{d,1}, K_{d,2}$ and $\xi_0 = 0$, $\xi_1 = x_{Bd_1} - \beta r_{Bd_1}$, $\xi_2 = x_{Bd_2} - \beta r_{Bd_2}$, etc., are the origins of the line singularities. These constants are also evaluated in the same step-by-step manner employed in the axial flow problem but with the boundary condition specified by equation (8b). It is noted that the perturbation velocity terms required by that equation are given by the first two of equation (I-24) and contain the term $\cos \theta$. Consequently, the $\cos \theta$ term is calcelled in equation (8b). The first constant is obtained from the boundary condition applied at the first control point (x_{B_1}, r_{B_1}). Rewriting equation (8b) gives

$$\frac{\alpha_f \cos \theta}{\dfrac{u_{B,d}}{V_\infty} \dfrac{dR}{dx_B}\bigg|_1 - \dfrac{v_{B,d}}{V_\infty}} = 1 \qquad (I-26)$$

Substitution from equation (I-24) leads to

$$K_{d,0} = \frac{\alpha_f}{\dfrac{\beta^2}{2}\left[\cosh^{-1}\left(\dfrac{x_{B_1}}{\beta r_{B_1}}\right) + \dfrac{x_{B_1}}{\beta r_{B_1}}\sqrt{\dfrac{x_{B_1}^2}{\beta^2 r_{B_1}^2} - 1}\right] + \dfrac{dR}{dx_B}\bigg|_1 \beta\sqrt{\dfrac{x_{B_1}^2}{\beta^2 r_{B_1}^2} - 1}} \qquad (I-27)$$

Let NXBODY be the number of line doublets with origins equally spaced on the body centerline. In general, the nth constant is explicitly determined from the boundary condition applied at the $(n+1)^{th}$ control point as follows.

$$a = \alpha_f - \sum_{k=1}^{n} K_{d,k-1}\left\{\frac{\beta^2}{2}\left[\cosh^{-1}\left(\frac{x_{B_{n+1}} - \xi_{k-1}}{\beta r_{B_{n+1}}}\right) + \left(\frac{x_{B_{n+1}} - \xi_{k-1}}{\beta r_{B_{n+1}}}\right)\right.\right.$$
$$\left.\left. \times \sqrt{\frac{(x_{B_{n+1}} - \xi_{k-1})^2}{\beta^2 r_{B_{n+1}}^2} - 1}\right] + \frac{dR}{dx_B}\bigg|_{n+1}\beta\sqrt{\frac{(x_{B_{n+1}} - \xi_{k-1})^2}{\beta^2 r_{B_{n+1}}^2} - 1}\right\} \qquad (I-28)$$

117

$$b = \frac{\beta^2}{2}\left[\cosh^{-1}\left(\frac{x_{B_{n+1}} - \xi_n}{\beta r_{B_{n+1}}}\right) + \left(\frac{x_{B_{n+1}} - \xi_n}{\beta r_{B_{n+1}}}\right)\sqrt{\frac{(x_{B_{n+1}} - \xi_n)^2}{\beta^2 r^2_{B_{n+1}}} - 1}\right]$$

$$+ \left.\frac{dR}{dx_B}\right|_{n+1} \beta\sqrt{\frac{(x_{B_{n+1}} - \xi_n)^2}{\beta^2 r^2_{B_{n+1}}} - 1}$$

$$K_{d,n} = \frac{a}{b}$$

$$n = 1, 2, \ldots (\text{NXBODY}-1)$$

(I-28)

(Concluded)

where

$$\xi_o = 0$$

$$\xi_{k-1} = x_{Bd_{k-1}} - \beta r_{Bd_{k-1}}; \quad k = 2, 3, \ldots$$

$$\xi_n = x_{Bd_n} - \beta r_{Bd_n}$$

$$x_{B_{n+1}} = x_{B_n} + \Delta x_B$$

$$\Delta x_B = \frac{\text{Body length}}{\text{NXBODY}}$$

$$r_{B_{n+1}} = R(x_{B_{n+1}})$$

$$\left.\frac{dR}{dx_B}\right|_{n+1} = R'(x_{B_{n+1}})$$

(I-29)

References 9 and 20 give an equivalent form of equation (I-28).

I-3. BODY INDUCED PERTURBATION VELOCITIES

The induced perturbation velocities due to one line source are given by equation (I-10). The contributions from one line doublet are specified by equation (I-24). The perturbation velocities induced by a body with a number, NXBODY, of line sources and doublets distributed along the centerline are obtained by adding the effects of all the singularities.

118

The constants K_n and $K_{d,n}$ have been determined above. At a field point specified in body coordinates x_B, r_B, θ, the body induced perturbation velocities are

$$\frac{u_B}{V_\infty} = \frac{u_{B,a}}{V_\infty} + \frac{u_{B,d}}{V_\infty} = \sum_{n=0}^{NXBODY-1} \left[-K_n \cosh^{-1} \frac{x_B - \xi_n}{\beta r_B} \right.$$

$$\left. + K_{d,n} \beta \cos \theta \sqrt{\frac{(x_B - \xi_n)^2}{\beta^2 r_B^2} - 1} \right]$$

$$\frac{v_B}{V_\infty} = \frac{v_{B,a}}{V_\infty} + \frac{v_{B,d}}{V_\infty} = \sum_{n=0}^{NXBODY-1} \left\{ K_n \beta \sqrt{\left(\frac{x_B - \xi_n}{\beta r_B}\right)^2 - 1} \right.$$

$$- K_{d,n} \frac{\beta^2 \cos \theta}{2} \left[\cosh^{-1} \left(\frac{x_B - \xi_n}{\beta r_B}\right) \right.$$

$$\left. \left. + \left(\frac{x_B - \xi_n}{\beta r_B}\right) \sqrt{\left(\frac{x_B - \xi_n}{\beta r_B}\right)^2 - 1} \right] \right\}$$

$$\frac{w_B}{V_\infty} = \frac{w_{B,d}}{V_\infty} = \sum_{n=0}^{NXBODY-1} \left\{ -\frac{K_{d,n} \sin \theta}{r_B} \left[\left(\frac{x_B - \xi_n}{2r_B}\right) \sqrt{(x_B - \xi_n)^2 - \beta^2 r_B^2} \right. \right.$$

$$\left. \left. - \frac{\beta^2 r_B}{2} \cosh^{-1} \left(\frac{x_B - \xi_n}{\beta r_B}\right) \right] \right\}$$

$$\left. \right\} \quad (I\text{-}30)$$

where

$$\left. \begin{array}{l} \beta^2 = M_\infty^2 - 1 \\[2mm] \xi_n = x_{Bd_n} - \beta r_{Bd_n} \end{array} \right\} \quad (I\text{-}31)$$

119

and

x_{Bd_n}, r_{Bd_n} = coordinates of the nth body definition point

u_B = axial perturbation velocity component

v_B = radial perturbation velocity component

w_B = tangential perturbation velocity component

The positive directions are shown again for convenience in the following sketch.
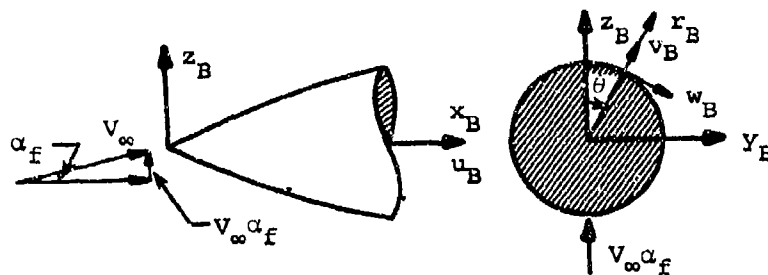
APPENDIX II

PERTURBATION VELOCITIES INDUCED BY A
SEMI-INFINITE TRIANGLE

II-1. INTRODUCTION

This appendix describes the perturbation velocities induced by a semi-infinite triangle with a sweptback leading edge, as shown in figure 3 of the main text in supersonic flow for two cases. First, the triangle is subjected to a constant jump in axial velocity across its plane. Second, a source distribution of constant strength is placed in its plane. Even though certain elements and difficulties of the underlying theory are discussed, the primary purpose of this appendix is to specify the formulations for perturbation velocities as used by the computer program.

II-2. ANALYTICAL APPROACH

The general method of finding the potential flow solution for a semi-infinite triangle with a swept back leading edge in supersonic flow is given in some detail in references 9 and 20. A summary of the method is contained in reference 10. In particular, the last reference discusses the difficulties associated with the nonplanar case. For that case, the plane of the semi-infinite triangle makes an angle with the x-axis in contradistinction with the planar case shown in figure 3. It is shown in reference 10 that the solution obtained in references 9 or 20 for the nonplanar case can introduce additional streamwise vortex sheets in the flow field. In addition, the nonplanar solution features a built-in thickness distribution for the case of the triangle being subjected to a jump condition in u-velocity. In principle, this undesirable thickness distribution is removable by subtracting another thickness distribution to cancel the effects of the undesired one. However, a simple means for eliminating the unwanted vortex sheet of vorticity has not been found. Accordingly, only planar solutions are used for the case of triangles with a jump in axial velocity. For simplicity, only planar solutions for triangles with constant source strength are employed herein.

For the sake of completeness, the method of solution will now be outlined. The linearized differential equation for the velocity potential generated by a small perturbation of a steady supersonic flow characterized by Mach number, M_∞, is given by the three-dimensional wave equation

121

$$(M_\infty^2 - 1)\phi_{xx} - \phi_{yy} - \phi_{zz} = 0 \qquad \text{(II-1)}$$

Perturbation velocities u, v, w also obey this wave equation. The coordinate system is shown in figure 3. Let Ω be an arbitrary variable representing either the potential ϕ or any one of the perturbation velocities. Reference 22 describes how a general solution to equation (II-1) can be obtained using Volterra's solution to the two-dimensional version of the wave equation. Considering a small flow perturbation originating on a surface, S, the value of either the potential or a perturbation velocity at any point, $P(x,y,z)$, is given by the following integral equation.

$$\Omega(x,y,z) = -\frac{1}{2\pi}\frac{\partial}{\partial x} \iint_\tau \left(\frac{\partial\Omega}{\partial\nu} + \frac{\partial\Omega'}{\partial\nu'}\right)\sigma\, dS$$

$$+ \frac{1}{2\pi}\frac{\partial}{\partial x} \iint_\tau (\Omega - \Omega')\frac{\partial\sigma}{\partial\nu}\, dS \qquad \text{(II-2)}$$

The domain of dependence τ is the Mach forecone from point P. Both integrals are to be evaluated over the part of surface S intercepted by the Mach forecone from P. The unprimed variable denotes the value of that variable on the same side of surface S as point P while the primed variable denotes its value on the opposite side of S. The function σ is the particular solution of equation (II-1) specified by Volterra which vanishes, together with its derivative $\partial\sigma/\partial\nu$, everywhere on the Mach forecone from P.

$$\sigma = \cosh^{-1}\frac{x - \xi}{\beta\sqrt{(y - \eta)^2 + (z - \zeta)^2}} \qquad \text{(II-3)}$$

In fact, this function is the indefinite integral of the fundamental solution to the wave equation (II-1) associated with a three-dimensional source at (ξ, η, ζ) in supersonic flow. The variable ν is associated with a vector called the conormal to the surface S. This vector is related to the normal vector to that surface. It has a special property in that the conormal to the Mach forecone lies in the surface of the Mach cone.

122

After performing substitutions for $\sigma, \partial\sigma/\partial\nu$, and dS in equation (II-1), it is possible to rewrite the integrals in equation (II-2) for either an inclined triangle or a triangle in the x-y plane such as the one shown in figure 3. The integrals can then be evaluated if the terms $(\Omega - \Omega')$ and $(\partial\Omega/\partial\nu + \partial\Omega'/\partial\nu')$ are prescribed on surface S which in this case is the semi-infinite triangle. It is most convenient (but possibly somewhat restrictive) to set the terms equal to a constant or zero. One choice is to specify a constant jump in axial velocity u across the triangular surface corresponding to a lifting surface. Another choice is to set Ω equal to the potential ϕ and the result is the integral form of the potential due to a surface distribution of sources.

In the following discussion, the formulations have been especially tailored to suit the computer program. They have been deduced from the results obtained by Woodward as published in reference 9.

II-2.1 Velocities Induced by a Semi-Infinite Triangle with a Jump in u-Velocity Across Its Plane

For this case, variable Ω in equation (II-2) is set equal to the perturbation velocity u_+ on the upper surface of the semi-infinite triangle shown in figure 3. The desired solution must have a constant discontinuity in u everywhere on S. Reference 9 shows the procedure required to obtain the solution expressed in terms of a pressure jump. In that reference, the pressure jump is actually directly related to the axial velocity jump through the linear velocity-pressure relationship. In this work, the more fundamental constant u-velocity jump concept is retained. For the reasons mentioned earlier in this appendix, only the solution for the triangle in the x-y plane is considered.

The coordinate system associated with the semi-infinite, sweptback triangle located in the x-y plane as shown in figure 3 is used in the following expressions for the perturbation velocities. In terms of functions to be specified, the perturbation velocities at a point $P(x,y,z)$ are given below for $x > 0$. Unswept triangles are discussed separately and expressions for the perturbation velocities are given later.

123

$$\frac{u}{V_\infty} = \frac{1}{\pi}\left(\frac{u_+}{V_\infty}\right) F_1$$

$$\frac{v}{V_\infty} = \frac{1}{\pi}\left(\frac{u_+}{V_\infty}\right)\left(F_7 - m_{\ell e} F_1\right)$$

$$\frac{w}{V_\infty} = \frac{1}{\pi}\left(\frac{u_+}{V_\infty}\right)\left[m_{\ell e}\left(1 - \frac{\beta^2}{m_{\ell e}^2}\right) F_2 - m_{\ell e} F_5 - F_4\right]$$

$$\beta^2 = M_\infty^2 - 1$$

(II-4)

The quantity $m_{\ell e}$ is the tangent of the sweep angle, $\psi_{\ell e}$. For $x \leq 0$, the velocities are zero. The strength of the singularity in the semi-infinite triangle is given by u_+/V_∞. Functions F_1, F_2, F_4, F_5, and F_7 depend on the geometry and are different for subsonic, sonic, and supersonic leading edges associated with the semi-infinite triangle. The unswept leading edge is dealt with separately. All four cases are discussed below

Subsonic Leading Edge $m_{\ell e}^2 > \beta^2$, $m_{\ell e} = \tan \psi_{\ell e}$
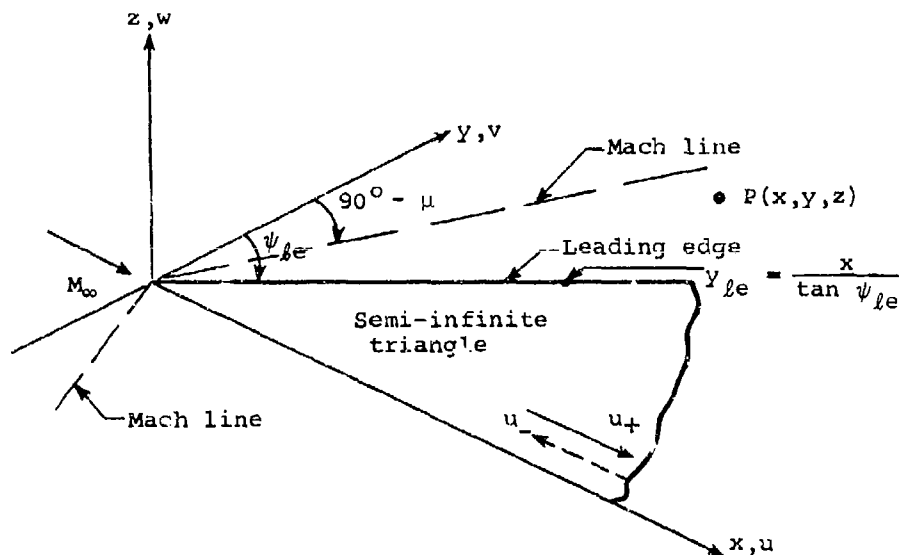
$$\tan(90^\circ - \mu) = \cot \mu = M_\infty^2 - 1 = \beta^2$$

124

$$F_1 = \tan^{-1} \frac{z\sqrt{x^2 - \beta^2(y^2 + z^2)}}{y^2 m_{\ell e} + z^2 m_{\ell e} - xy} \; ; \; F_1 = \pi \quad \text{for} \quad 0 < y < y_{\ell e}, \; z = 0$$

$$F_2 = \frac{m_{\ell e}}{\sqrt{m_{\ell e}^2 - \beta^2}} \; \ell n \; \frac{xm_{\ell e} - \beta^2 y + \sqrt{(xm_{\ell e} - \beta^2 y)^2 - \beta^2[(x - ym_{\ell e})^2 + z^2(m_{\ell e}^2 - \beta^2)]}}{\beta\sqrt{(x - ym_{\ell e})^2 + z^2(m_{\ell e}^2 - \beta^2)}}$$

$$F_4 = \frac{y}{y^2 + z^2} \sqrt{x^2 - \beta^2(y^2 + z^2)} \; ; \quad F_5 = \ell n \; \frac{x + \sqrt{x^2 - \beta^2(y^2 + z^2)}}{\beta\sqrt{y^2 + z^2}}$$

$$F_7 = \frac{z}{y^2 + z^2} \sqrt{x^2 - \beta^2(y^2 + z^2)} \tag{II-5}$$

The above functions are to be substituted into equation (II-4). On the x-axis or along the leading edge, the resulting velocities are singular or indeterminate. The computer program has been arranged to set the velocities equal to zero when the field point lies either on the x-axis or the leading edge. If the coordinates of point P satisfy the relation

$$x^2 - \beta^2(y^2 + z^2) \leq 0 \tag{II-6}$$

then the point P lies on or outside the Mach cone from the origin. For this case, the velocities are also zero.

125

Sonic Leading Edge $m^2_{\ell e} = \beta^2$, $m_{\ell e} = \tan \psi_{\ell e}$, $\tan(90 - \mu) = \beta^2$
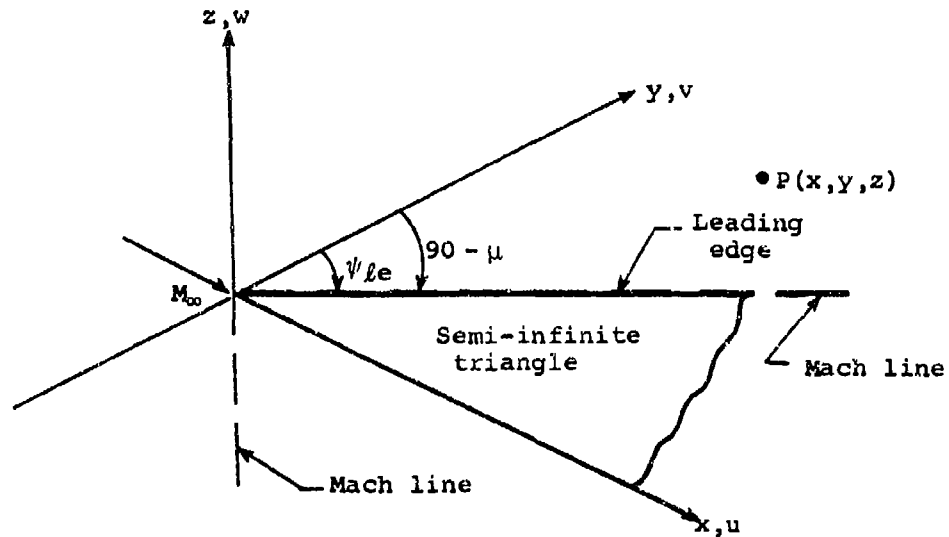

All functions are the same as for the subsonic leading-edge case given by equation (II-5) except function F_2. It is now specified as follows.

$$F_2 = \frac{\sqrt{x^2 - \beta^2(y^2 + z^2)}}{x - \beta y} \tag{II-7}$$

The velocity components are singular or indeterminate at points along the x-axis or the leading edge and are set equal to zero by the program. If the coordinates of point P satisfy equation (II-6), all velocity components are zero.

126

$$m_{\ell e}^2 < \beta^2 \;,\; m_{\ell e} = \tan \psi_{\ell e} \;,\; \tan(90 - \mu) = \beta^2$$

$$x_{\ell e} = y \tan \psi_{\ell e}$$
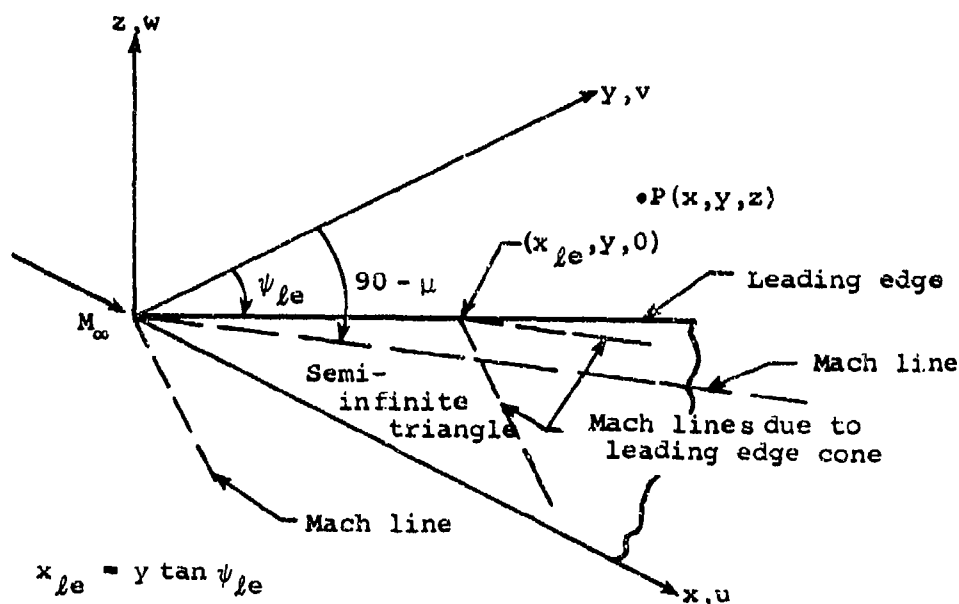
The field point $P(x,y,z)$ lies inside the Mach cone from the origin when the following condition is satisfied by its coordinates.

$$x^2 - \beta^2 (y^2 + z^2) > 0 \tag{II-8}$$

For this case, all functions are given by equation (II-5) except F_2 which is changed to

$$F_2 = \frac{m_{\ell e}}{\sqrt{\beta^2 - m_{\ell e}^2}} \tan^{-1} \frac{\sqrt{(\beta^2 - m_{\ell e}^2)[x^2 - \beta^2(y^2 + z^2)]}}{x m_{\ell e} - \beta^2 y} \tag{II-9}$$

The velocity components are singular or indeterminate at points along the x-axis. The computer program is arranged to set u,v,w equal to zero when both y and z are zero. If the point $P(x,y,z)$ lies outside the Mach cone from the origin (equation (II-8) not satisfied) but is inside the Mach cone with its origin at $(x_{\ell e}, y, 0)$ on the leading edge, then the following conditions are met.

127

$$y > 0$$

$$(x - x_{\ell e})^2 - \beta^2 z^2 > 0 \qquad \Biggr\} \qquad \text{(II-10)}$$

For this situation, the functions assume the following constant values

$$F_1 = \begin{cases} \pi \ \text{for} \ z \geq 0 \\[2mm] -\pi \ \text{for} \ z < 0 \end{cases}$$

$$F_2 = \frac{\pi m_{\ell e}}{\sqrt{\beta^2 - m_{\ell e}^2}} \qquad \Biggr\} \qquad \text{(II-11)}$$

$$F_4 = F_5 = F_7 = 0$$

If the point P is outside the Mach cone from the origin and its y-coordinate is negative, then all velocities are set equal to zero. Zero velocities also result when the point is outside the Mach cone from the origin and the Mach cone from the leading edge.

Unswept Leading Edge $\qquad m_{\ell e} = 0, \ \beta^2 = M_\infty^2 - 1$

128
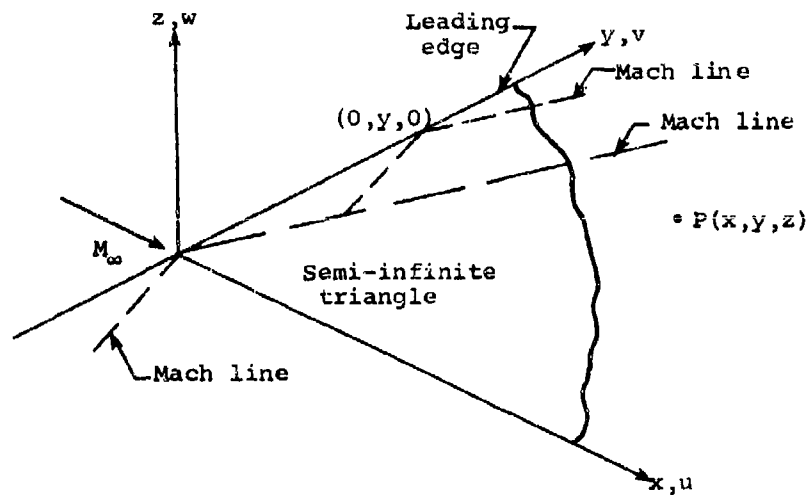
This case is really a special version of the semi-infinite triangle with a supersonic leading edge. Equation (II-4) does not apply to this case. Instead, the following expressions specify the perturbation velocities induced at a point $P(x,y,z)$ by the unswept semi-infinite triangle with a constant jump in u-velocity.

$$\frac{u}{V_\infty} = \frac{1}{\pi} \left(\frac{u_+}{V_\infty} \right) F_1$$

$$\frac{v}{V_\infty} = \frac{1}{\pi} \left(\frac{u_+}{V_\infty} \right) F_7 \tag{II-12}$$

$$\frac{w}{V_\infty} = \frac{1}{\pi} \left(\frac{u_+}{V_\infty} \right) (F_2 - F_4)$$

Functions F_1, F_2, F_4 and F_7 depend on the location of the field point. If the point lies inside the Mach cone from the origin, its coordinates satisfy equation (II-8). Functions F_4 and F_7 are given by equation (II-5) and

$$F_1 = \tan^{-1} \frac{z\sqrt{x^2 - \beta^2(y^2 + z^2)}}{-xy}$$

$$F_2 = -\beta \tan^{-1} \frac{\sqrt{x^2 - \beta^2(y^2 + z^2)}}{-\beta y} \tag{II-13}$$

The velocity components are singular or indeterminate at points along the x-axis. The computer program is arranged to set u, v, w equal to zero when both y and z are zero. If the point $P(x,y,z)$ lies outside the Mach cone from the origin but is inside the Mach cone with its origin at $(0,y,0)$ on the leading edge, then conditions (II-6) and (II-10) are satisfied. The functions then assume the following constant values.

129

$$F_1 = \begin{cases} \pi & \text{for } z \geq 0 \\ -\pi & \text{for } z < 0 \end{cases}$$

$$F_2 = -\beta\pi$$

$$F_4 = F_5 = F_7 = 0$$

(II-14)

Figure II-1 shows the behavior of velocity components u/V_∞, v/V_∞, and w/V_∞ for unit strength u_+/V_∞ along a traverse parallel to the y-axis in the $z = 0$ plane. Results are shown for the subsonic, sonic, and supersonic leading-edge cases and the Mach number equals $\sqrt{2}$.

II-2.2 Velocities Induced by a Semi-Infinite Triangle with a Source Distribution of Constant Strength

For the purpose of generating the solution for this case, variable Ω in equation (II-2) is set equal to the potential ϕ on the upper surface of the semi-infinite triangle shown in figure 3. The partial derivative $\partial\phi/\partial v$ in equation (II-2) represents the velocity component along the conormal to the upper surface of the triangle and $\partial\phi'/\partial v'$ is the velocity component along the conormal to the lower surface. If ϕ' has the same sign as ϕ, a discontinuity in that velocity component will appear in the flow at the surface of the triangle. For the sweptback triangle located in the x-y plane as shown in figure 3 (disregarding the u_+ and u_- vectors shown), the velocity component under consideration is in fact the velocity component w in the z-direction. Therefore, the resulting solution is one which produces an upwash on the upper surface of the triangle and a downwash just below the surface. Since the planar solution for the constant u-velocity jump triangle is used in the computer program as described in the preceding section, the planar solution for the source triangle given in reference 9 is used here for the sake of consistency.

The coordinate system shown in figure 3 is used again in the expressions for the perturbation velocities that follow. For $x > 0$ and with nonzero leading-edge sweep, the perturbation velocities induced at a given point $P(x,y,z)$ by a semi-infinite triangle with a source distribution of constant strength are given below. For $x \leq 0$, the velocities are zero. The case for an unswept triangle is discussed separately and expressions for perutrbation velocities are given.

130

$$\frac{u}{V_\infty} = -\frac{1}{\pi} (\tan \theta) \frac{F_2}{m_{\ell e}}$$

$$\frac{v}{V_\infty} = \frac{1}{\pi} (\tan \theta)(F_2 - F_5)$$

$$\frac{w}{V_\infty} = \frac{1}{\pi} (\tan \theta) F_1$$

$$m_{\ell e} = \tan \psi_{\ell e}$$

$$(II-15)$$

The source strength, $\tan \theta$, of the semi-infinite triangle under consideration is associated with the slope of the thickness envelope of the surface under consideration. As discussed in the flow field calculation section in the main text, the thickness slope is bounded in magnitude. Referring to the general panel layout shown in figure 1, the required source strengths for the four semi-infinite triangles used to generate the solution for one source panel shown on the wing are given by the slope of the wing thickness envelope calculated at the panel centroid. Functions F_1, F_2, and F_5 are determined as described in section II-2.1 for the cases of subsonic, sonic, and supersonic leading edges. In all three cases, the v and w components are singular or indeterminate at points on the x-axis. Furthermore, the u, v, and w components are singular or indeterminate at the leading edge. The computer program is arranged to set the velocity components equal to zero.

As already mentioned in connection with the constant u-velocity jump triangle, the unswept leading-edge case is a special version of the semi-infinite triangle with a supersonic leading edge. Equation (II-15) is not used for this case. The expressions below specify the perturbation velocities induced at a point $P(x,y,z)$ by the unswept semi-infinite source triangle for $x > 0$. If $x \leq 0$, the velocities are zero.

131

$$\frac{u}{V_\infty} = -\frac{1}{\pi} (\tan \theta) F_2$$

$$\frac{v}{V_\infty} = -\frac{1}{\pi} (\tan \theta) F_5 \qquad \qquad (II\text{-}16)$$

$$\frac{w}{V_\infty} = \frac{1}{\pi} (\tan \theta) F_1$$

Functions F_1, F_2, and F_5 depend on the location of the point P. If the point lies inside the Mach cone from the origin, its coordinates satisfy equation (II-8). Function F_1 is given by equation (II-13), function F_5 by equation (II-5), but F_2 is changed to

$$F_2 = \frac{1}{\beta} \tan^{-1} \frac{\sqrt{x^2 - \beta^2(y^2 + z^2)}}{\beta y} \qquad \qquad (II\text{-}17)$$

The velocity components are singular or indeterminate at points along the x-axis. The computer program is arranged to set the velocities equal to zero. If the point $P(x,y,z)$ lies outside the Mach cone from the origin but is inside the Mach cone with its origin at $(0,y,0)$ on the leading edge, then equations (II-6) and (II-10) are satisfied. The functions then acquire the following constant values.

$$F_1 = \begin{cases} \pi & \text{for} \quad z \geqslant 0 \\ -\pi & \text{for} \quad z < 0 \end{cases}$$

$$F_2 = \frac{\pi}{\beta} \qquad \qquad (II\text{-}18)$$

$$F_5 = 0$$

It is seen that for points in the plane of the semi-infinite triangle between the Mach line from the origin and the unswept leading edge, sidewash component v is zero and components u and w are constant.

132

The behavior of the velocity components, u/V_∞, v/V_∞, and w/V_∞, for given source strength $\tan \theta$ is shown in figure II-2 for a swept semi-infinite triangle along a traverse parallel to the y-axis in the $z = 0$ plane. Results are shown for the subsonic, sonic and supersonic leading-edge cases and the Mach number is $\sqrt{2}$.
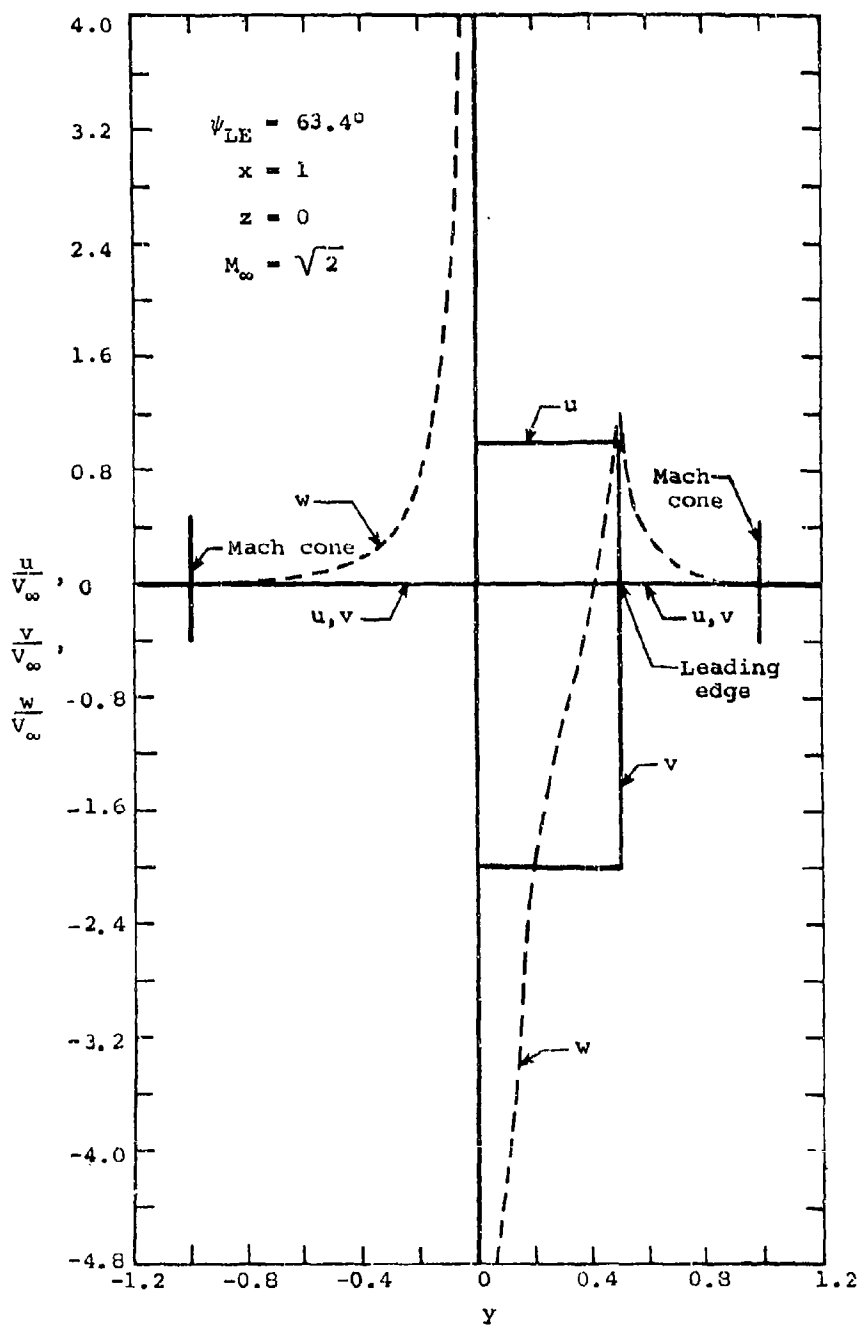
(a)   Subsonic leading edge.

Figure II-1.- Velocity components along y-traverse
in the plane of the semi-infinite triangle
with a jump in u-velocity.

134
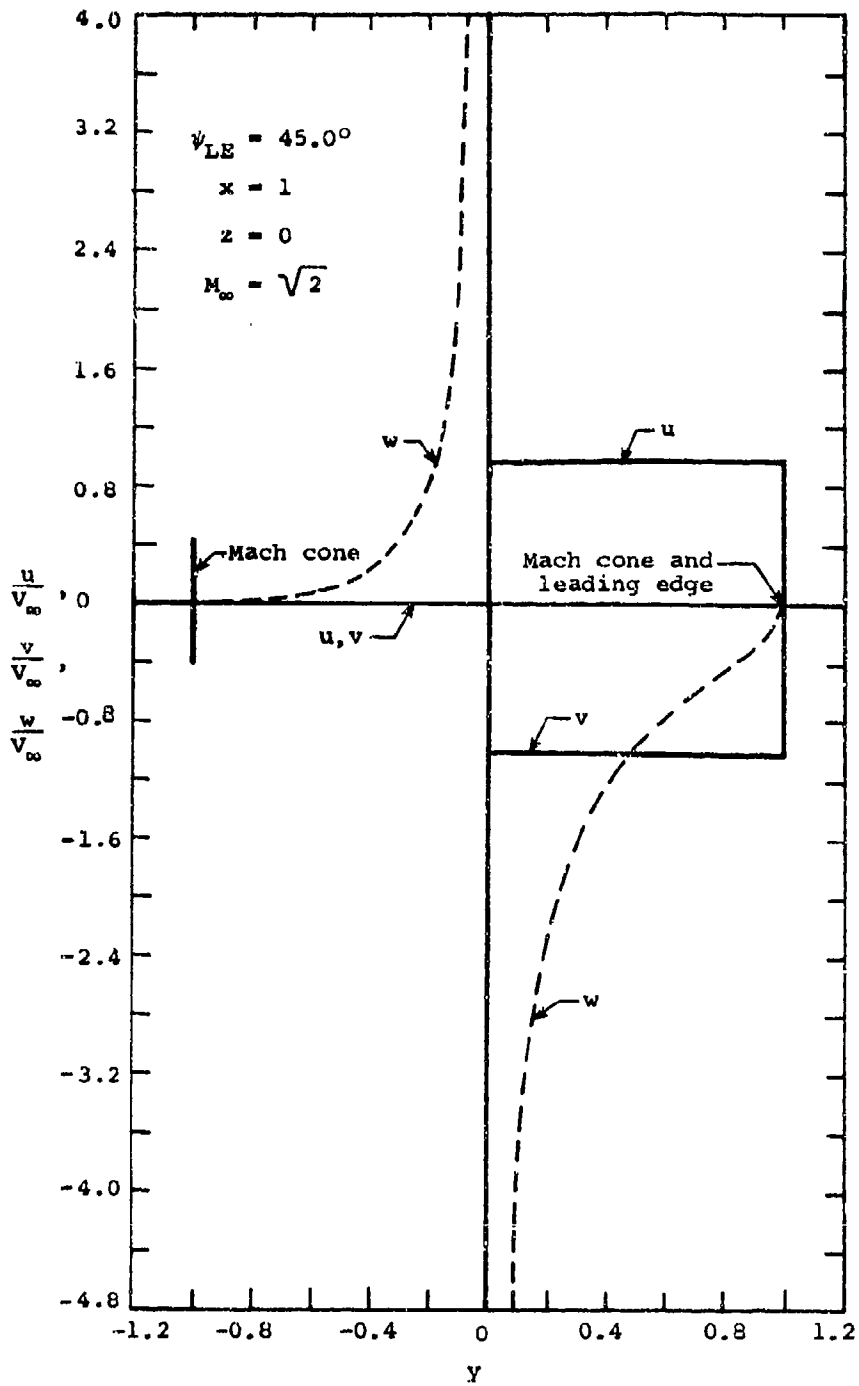
(b) Sonic leading edge.

Figure II-1.- Continued.

135
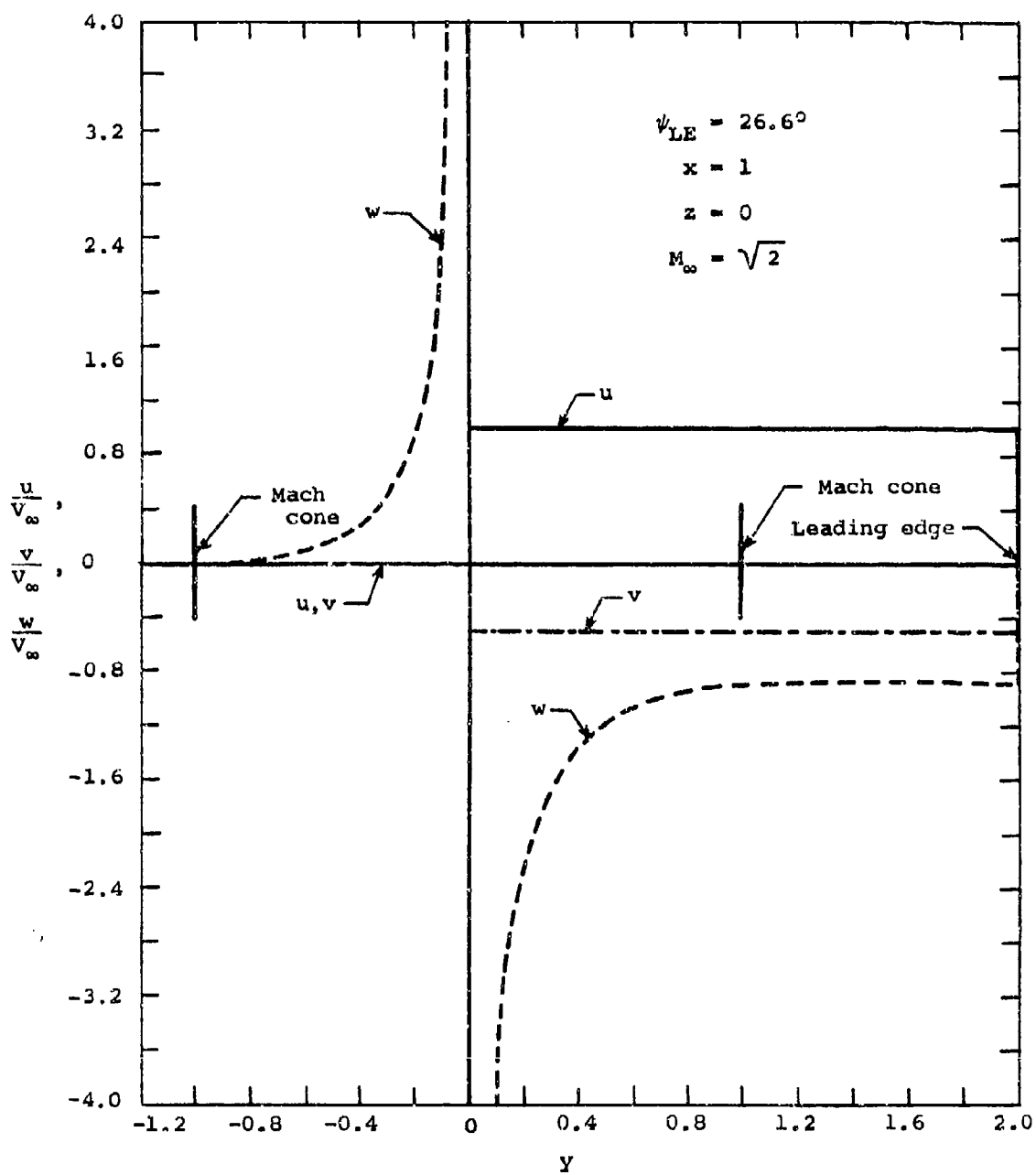
(c) Supersonic leading edge.

Figure II-1.- Concluded.

136
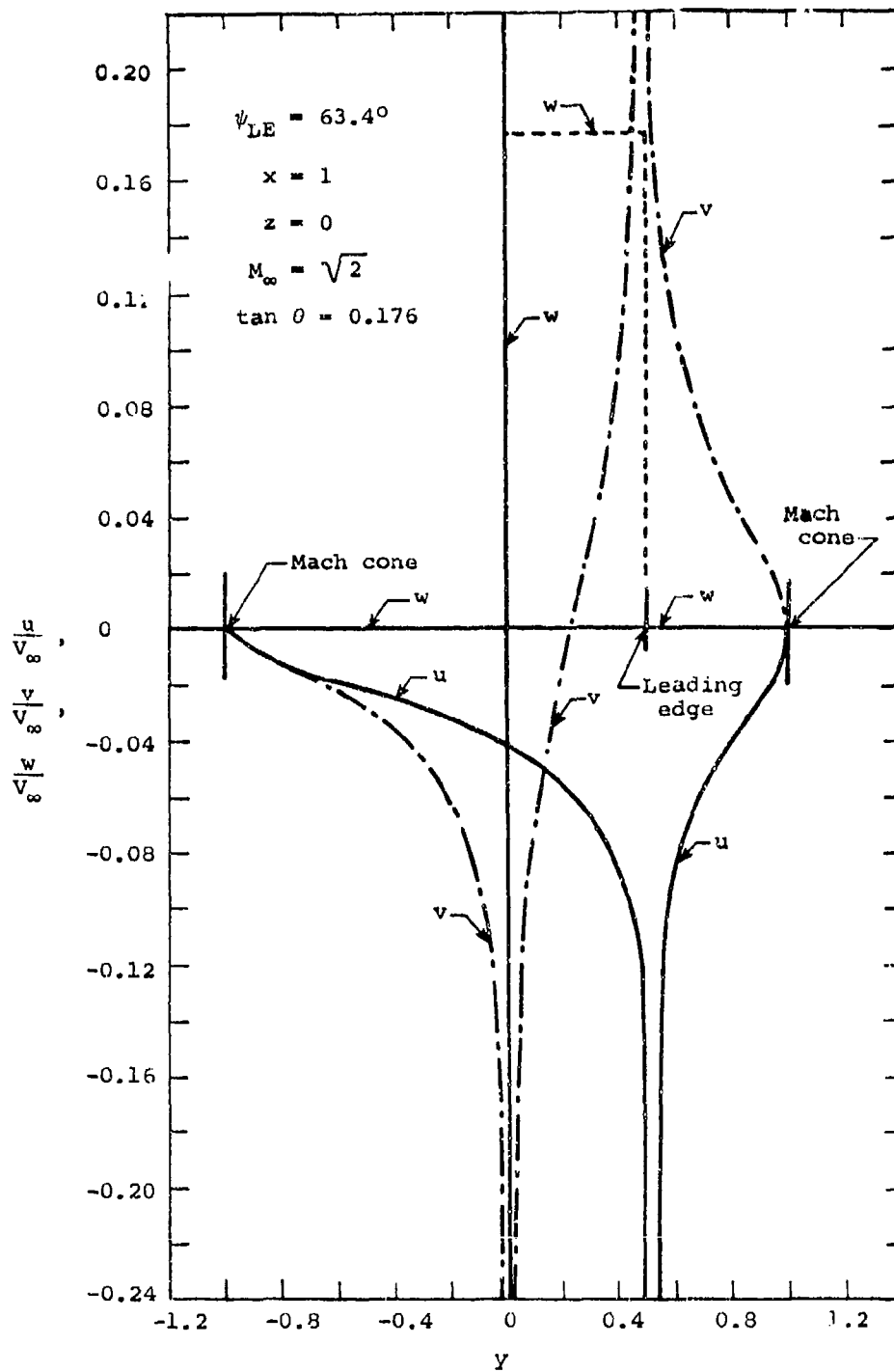
(a)   Subsonic leading edge.

Figure II-2.- Velocity components along y-traverse
in the plane of the semi-infinite triangle
with constant source strength.

137
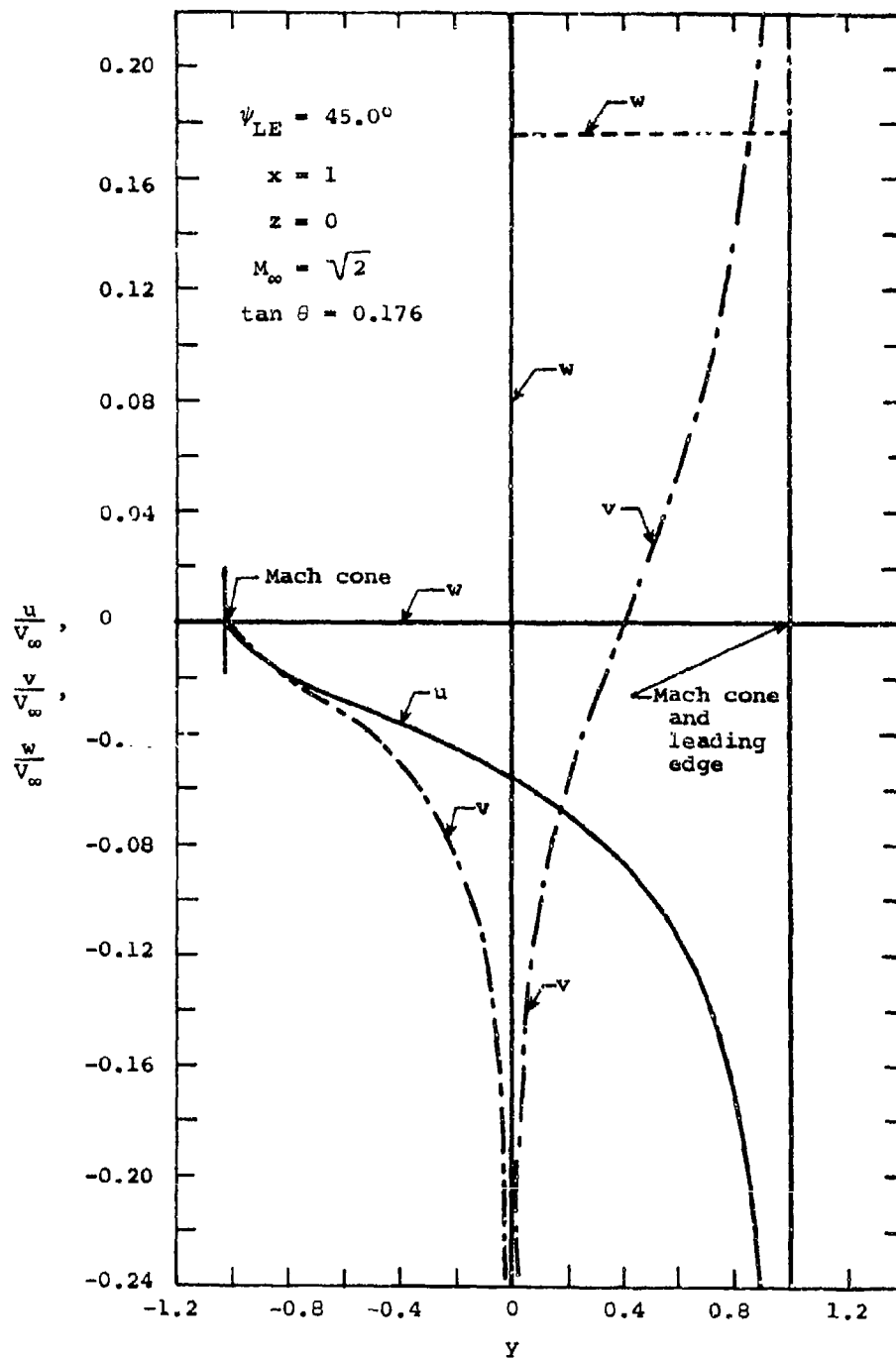
(b) Sonic leading edge.

Figure II-2.- Continued.
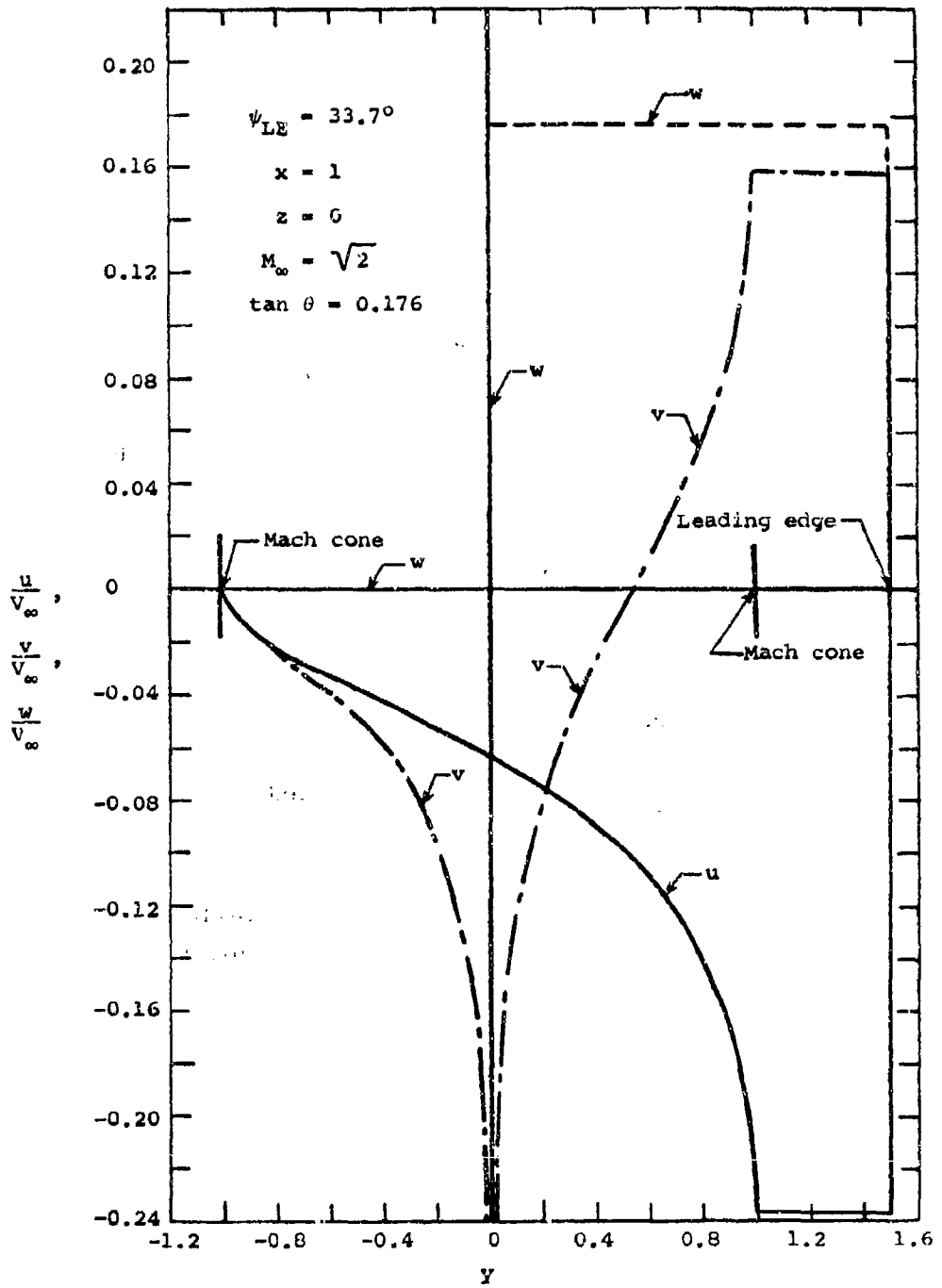
(c) Supersonic leading edge.

Figure II-2.- Concluded.

139

APPENDIX III

DETACHED SHOCK ANALYSIS

III-1. INTRODUCTION

In this appendix, a method is described for predicting the shape of a detached shock which stands ahead of a two-dimensional shape with a blunt leading edge. For shapes with cylindrical forebodies, Love in reference 14 presents a shock shape and location determination method based on simple concepts and augmented with certain corrections obtained from experimental data. Recently, Rizzi at the NASA/Ames Research Center performed calculations to determine shock standoff distance and other properties of the flow over a two-dimensional flat body with cylindrical leading edge. His calculations involve solving the Euler equations (inviscid Navier-Stokes equations) by means of a finite-differencing scheme and this method is cited in reference 15.

During the course of work performed on the development of the flow field calculation method described in this report, the above-mentioned shock prediction methods were investigated in connection with correcting the linear flow theory for nonlinear shock effects. As it turned out, the present flow field calculation method itself predicts the shock location. Nevertheless, an independent shock prediction method was found to be useful in checking the shock shape predicted by the present method as implemented in the computer program.

In what follows, the actual mechanics involved in applying the detached shock prediction method to a cylindrical forebody shape are described. The method for determining the shock shape is basically that of Love in reference 14 but with standoff distance taken from calculations performed by Rizzi of reference 15.

In addition, a criterion for the maximum value of the wing thickness slope is developed on the basis of the detached shock model. An upper bound is required by the present flow field calculation method when the configuration of interest includes a wing with a blunt leading edge. For such a wing, the wing thickness slope is infinite at the leading edge. As described in this report, the strengths of the source panels used to model thickness are directly related to the thickness slopes measured in the streamwise direction at the panel centroids. If the number of source

panels in a chordwise row is large, the thickness slopes associated with the forward source panels may become too large in magnitude and are then incompatible with the linear, potential theory on which the solution for the source panel is based.

III-2. PROCEDURE FOR CALCULATING SHAPE OF DETACHED SHOCK

The procedure described here is the one developed by Love in reference 14 with the exception of the determination of the shock detachment distance. Rizzi of reference 15 solved the Euler equations using a finite element technique to obtain details of the flow over a two-dimensional flat shape with a cylindrical forebody at transonic or supersonic speeds. The flow region was divided into a mesh of many quadrilateral panels of varying size. The results of Rizzi's computations in terms of shock standoff distance and sonic line location are useful as the starting point of the approximate shock shape model developed by Love.

Figure III-1 shows the two-dimensional standoff distance of shocks associated with flow normal to a circular cylinder as a function of Mach number, M_1, normal to the body. The theoretical points represent the converged results from calculations performed by Rizzi for different mesh sizes. Also shown are a few points from experimental measurements published in reference 6. Agreement between theory and experiment is very good for the two experimental points shown. Rizzi's calculations also include the location of the sonic point on the body. This location is schematically shown in figure III-2. Although the calculated standoff distances showed convergence with finer mesh size used by Rizzi, the sonic point locations did not. Apparently, the angular locations of the sonic point require even finer or differently spaced quadrilaterals before convergence is reached. Work is presently under way to try a mesh size which is exponentially varied and is very fine near the body surface.

The equations required for calculating the shock shape by the approximate method of Love are given in reference 14 and will now be expressed in the coordinates (x,y) and radius $d/2$ shown in figure III-2. Based on a hyperbolic representation of the shock, the shape of the shock is given as follows.

$$\frac{y}{d} = \frac{\cos\ \delta_{det}}{\beta} \sqrt{\left(\frac{x}{d\ \cos\ \delta_{det}}\right)^2 - \left(\frac{x_o}{d'}\right)^2}$$

$$\beta = \sqrt{M_1^2 - 1}$$

$$\text{(III-1)}$$

The ratio x_o/d' is given by the following expression:

$$\frac{x_o}{d'} = \frac{\beta\sqrt{\beta^2\tan^2\epsilon_s - 1}\left(\frac{x'}{d'} + \frac{\tan\ \eta}{2}\right)}{\beta^2\tan\ \epsilon_s - \beta\sqrt{\beta^2\tan^2\epsilon_s - 1} + \tan\ \eta} \qquad \text{(III-2)}$$

Angle ϵ_s is the shock wave angle for sonic flow behind the shock. It can be calculated from equation (167) in reference 11.

$$\sin^2\epsilon_s = \frac{1}{7M_1^2}\left[3M_1^2 - 2 + \sqrt{3(3M_1^4 - 4M_1^2 + 13)}\right] \qquad \text{(III-3)}$$

Angle η is the angle between the normal to the free stream and the control line. The most convenient and accurate way to determine it is to read its value from figure 10 in reference 14 as a function of M_1. Finally, quantity x'/d' is related to the shock standoff distance

$$\frac{x'}{d'} = \frac{x'}{d}\frac{d}{d'} = \left(\frac{\Delta x_R}{d} + \frac{1}{2} - \frac{1}{2}\sin\ \delta_{det}\right)\frac{1}{\cos\ \delta_{det}} \qquad \text{(III-4)}$$

In this equation, $\Delta x_R/d$ is given in figure III-1 as a function of M_1. Angle δ_{det} is the semiapex angle for a wedge for which the shock is first detached. It can be determined from chart 2 in reference 11, or the following relations can be used. The shock wave angle $\theta_{\delta_{det}}$ for maximum stream deflection behind the shock (which occurs when it is first detached) is given by equation (168) in reference 11.

142

$$\sin^2\theta_{\delta_{det}} = \frac{1}{7M_1^2}\left[3M_1^2 - 5 + \sqrt{3(3M_1^4 + 4M_1^2 + 20)}\right] \qquad (III-5)$$

The corresponding maximum wedge angle, δ_{det}, or the angle for which the shock first is detached is given by equation (138) in reference 11.

$$\cot\delta_{det} = \tan\theta_{\delta_{det}}\left[\frac{6M_1^2}{5(M_1^2\sin^2\theta_{\delta_{det}} - 1)} - 1\right] \qquad (III-6)$$

III-3.   MAXIMUM SLOPE ANGLE

The actual flow behind the detached shock includes the following features. A region of subsonic flow exists between the body surface, the shock, and the sonic line which is curved in reality. At the sonic line, the flow has accelerated from subsonic and enters the supersonic speed region. No part downstream of the sonic point on the body affects the detachment process. The situation is depicted schematically in the following sketch.
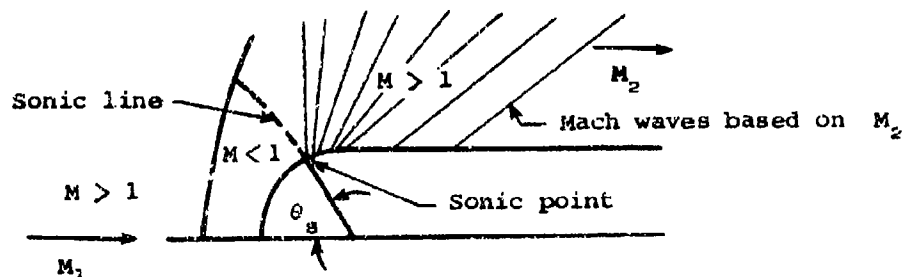
From the sonic point on, the flow accelerates to uniform speed in the region next to the body. Near the shock and away from the body, curved lines (characteristics) originating at points on the body behind the sonic point are propagated out to the shock and cause it to curve.

On the basis of the above observations, the first body slope used in the supersonic flow field calculation method is bounded by the slope of the body at the sonic point. Until Rizzi's calculations generate converged results for the values of angle θ_s associated with the sonic point, angle δ_{det} should be used as the upper limit on the surface slopes. This result is based on the assumption that the nose contour in front of the sonic line

143

will not change the detached shock location. This assumption is satis-
fied if the nose contour lies within the wedge formed by drawing the
tangent to the nose at the sonic point. This assumption was first
suggested by Busemann (ref. 23). As can be seen from figure III-3,
angle δ_{det} approaches zero as the Mach number M_1 is reduced to 1.

In the application of the above to blunt wings with marginally
supersonic leading edges, it is probably better to consider the edge
subsonic. The upper limit on the thickness slopes is then determined
on the basis of the free-stream Mach number as described in this report.
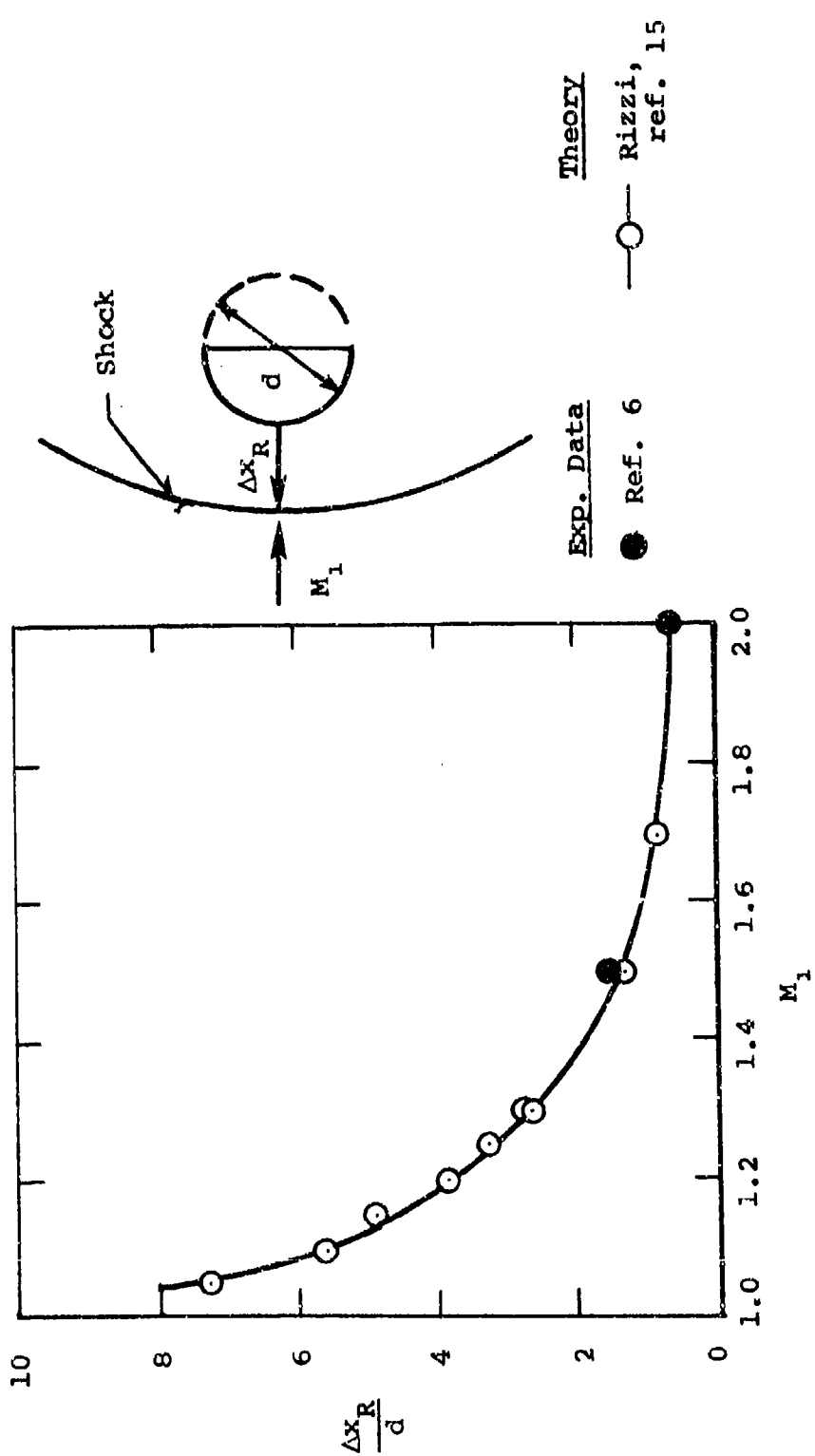
Figure III-1.- Shock standoff distance for cylindrical forebodies.

145
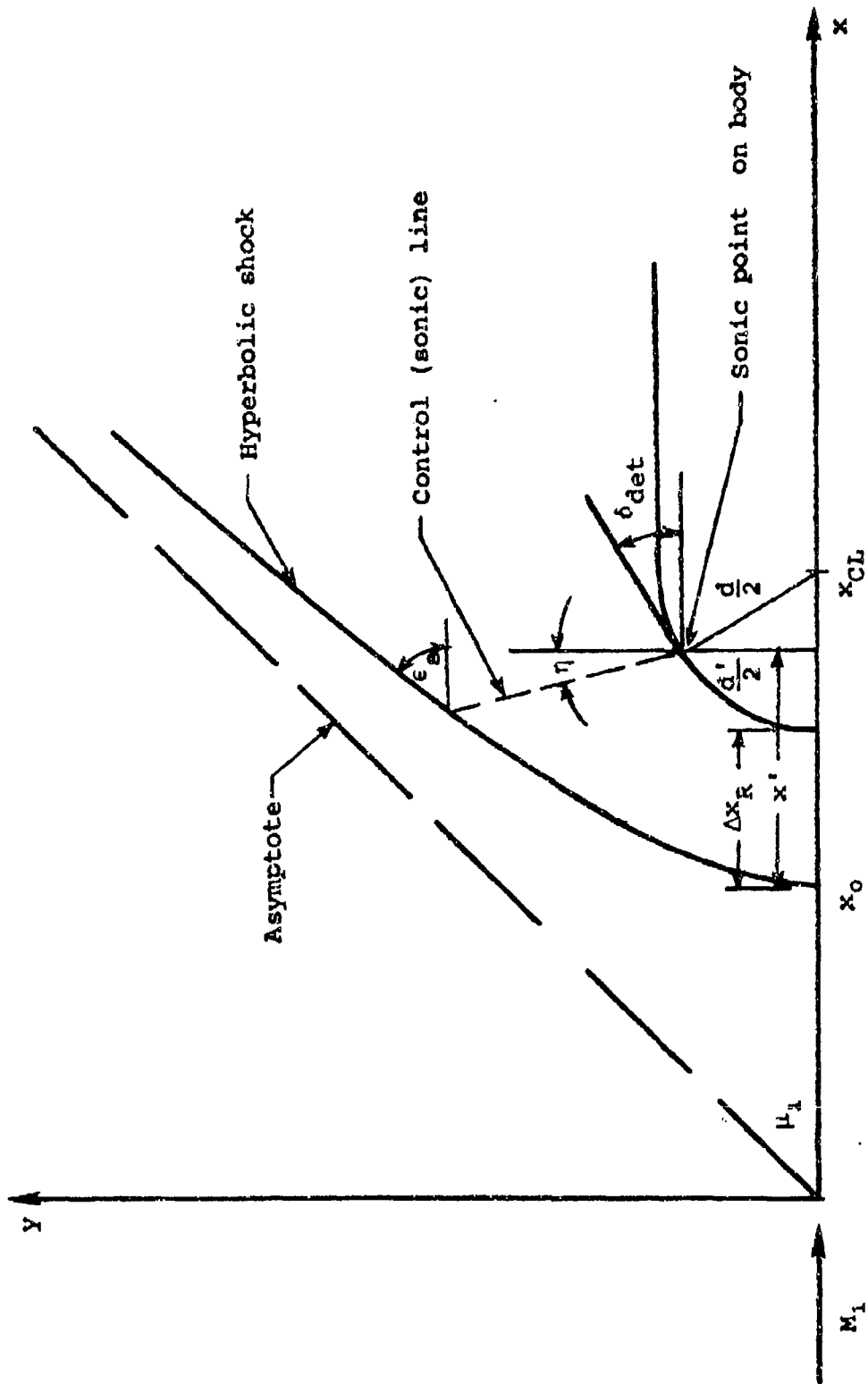
Figure III-2.- Coordinates associated with detached shock model.

146
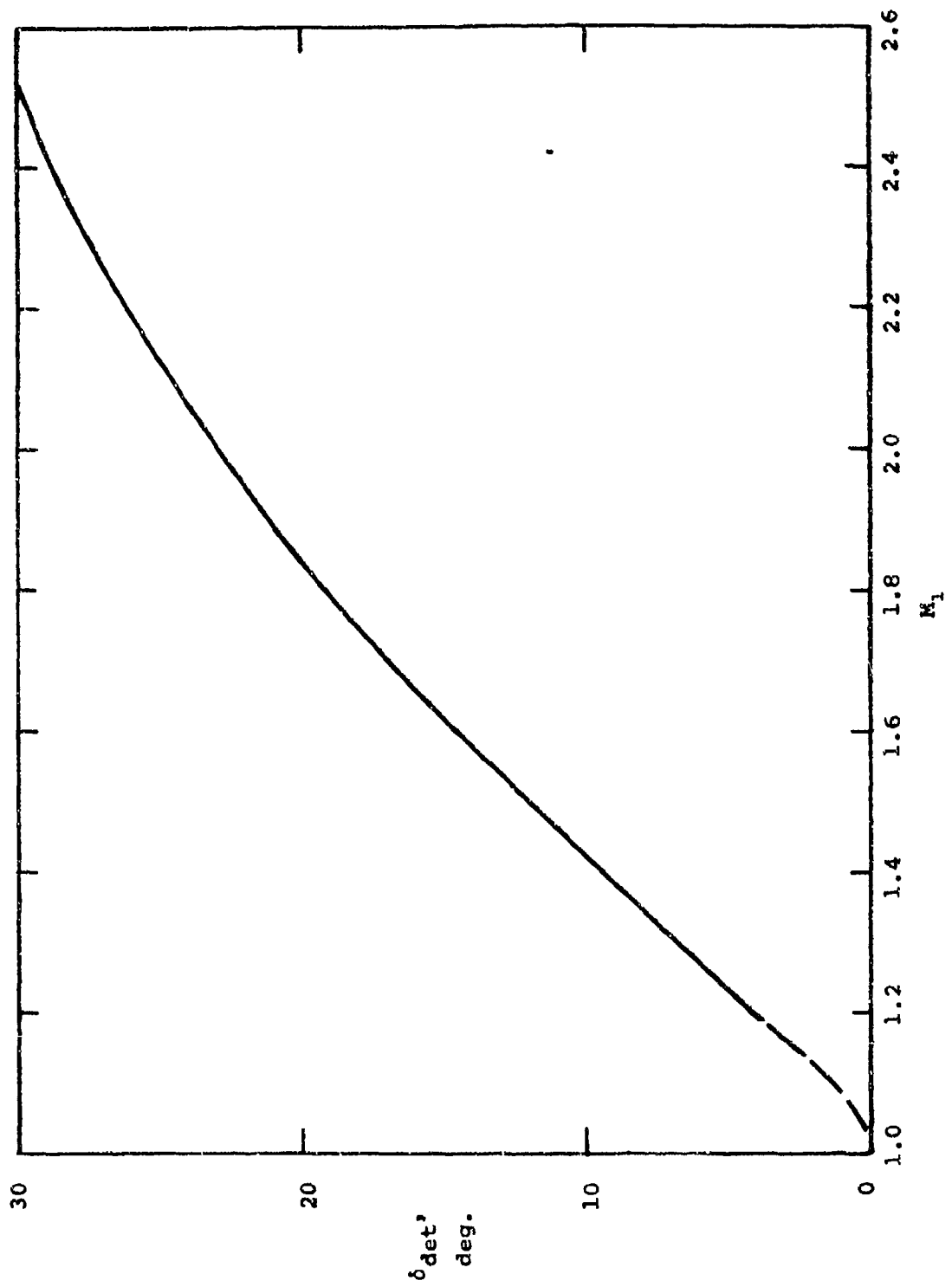
Figure III-3.- Variation of shock detachment angle with upstream Mach number for wedges.

REFERENCES

1. Dillenius, M. F. E., Goodwin, F. K., and Nielsen, J. N.: _Extension of the Method for Predicting Six-Degree-of-Freedom Store Separation Trajectories at Speeds up to the Critical Speed to Include a Fuselage with Noncircular Cross Section. Volume I - Theoretical Methods and Comparisons with Experiment. Volume II - Users Manual for the Computer Program._ AFFDL-TR-74-130, Vols. I and II, Nov. 1974.

2. Goodwin, F. K., Dillenius, M. F. E., and Nielsen, J. N.: _Prediction of Six-Degree-of-Freedom Store Separation Trajectories at Speeds up to the Critical Speed. Volume I - Theoretical Methods and Comparison with Experiment. Volume II - Users Manual for the Computer Program._ AFFDL-TR-72-83, Vols. I and II, Oct. 1974.

3. Goodwin, F. K., Keirstead, M. M., and Dillenius, M. F. E.: _Prediction of Supersonic Store Separation Characteristics. Volume II - Users Manual for the Computer Program._ AFFDL-TR-76-41, Vol. II, May 1976.

4. Perkins, S. C. and Goodwin, F. K.: _Data Report for an External Store Test Program Conducted at Supersonic Speeds._ Volumes I-VII. NEAR TR 103, Dec. 1975.

5. Goodwin, F. K., Nielsen, J. N., and Dillenius, M. F. E.: _A Method for Predicting Three-Degree-of-Freedom Store Separation Trajectories at Speeds up to the Critical Speed._ AFFDL-TR-71-81, Nov. 1974.

6. Liepmann, H. W. and Roshko, A.: _Elements of Gas Dynamics._ John Wiley and Sons, Inc., 1957, pp. 226-233 and 240-242.

7. Tsien, H. S.: _Supersonic Flow Over an Inclined Body of Revolution._ Jour. Aero. Sci., vol. 5, no. 12, 1938, pp. 480-483.

8. von Kármán, T. and Moore, M. B.: _Resistance of Slender Bodies Moving with Supersonic Velocities, With Special Reference to Projectiles._ ASME Trans. APM 54-27, 1938, p. 303.

9. Woodward, F. A. and Larson, J. W.: _A Method of Optimizing Camber Surfaces for Wing-Body Combinations at Supersonic Speeds. Part I - Theory and Application._ Doc. D6-10741, Pt. I, The Boeing Company, Oct. 1965.

10. Dillenius, M. F. E. and Nielsen, J. N.: _Supersonic Lifing-Surface Computer Program for Cruciform Wing-Body Combinations in Combined Pitch and Sideslip._ Office of Naval Research Contract No. N00014-74-C-0050, Annual Report, Dec. 1974 (also NEAR TR 74).

11. NACA Ames Research Staff: _Equations, Tables, and Charts for Compressible Flow._ NACA Rept. 1135, 1953.

12. Hall, I. M.: _Inversions of the Prandtl-Meyer Relation._ Aero. Jour., Roy. Aero. Soc., UK, Sept. 1975, pp. 417-418.

13. Carlson, H. W.: _Measurements of Flow Properties in the Vicinity of Three Wing-Fuselage Combinations at Mach Numbers of 1.61 and 2.01._ NASA TM X-64, Oct. 1959.

14. Love, E. S.: A Reexamination of the Use of Simple Concepts for Predicting the Shape and Location of Detached Shock Waves. NACA TN 4170, Dec. 1957.

15. Rizzi, A. W.: Transonic Solutions of the Euler Equations by the Finite Volume Method. Paper presented at Transsonicum Symposium II sponsored by IUTAM, Sept. 1975, Göttingen, Germany.

16. Mack, R. J.: A Study of Methods Which Predict Supersonic Flow Fields from Body Geometry, Distance, and Mach Number. NASA TN D-7387, Nov. 1973.

17. Morkovin, M. V., Migotski, E., Bailey, H. E., and Phinney, R. E.: Experiments on Interaction of Shock Waves and Cylindrical Bodies at Supersonic Speeds. Jour. Aero. Sci., vol. 19, Apr. 1952, pp. 237-249.

18. Whitham, G. B.: The Flow Pattern of a Supersonic Projectile. Communications on Pure and Applied Math., vol. V, 1952, pp. 301-348.

19. Friedrichs, K. O.: Formation and Decay of Shock Waves. Communications on Pure and Applied Math., vol. I, no. 3, 1948, pp. 211-245.

20. Woodward, F. A., Tinoco, E. N., and Larson, J. W.: Analysis and Design of Supersonic Wing-Body Combinations, Including Flow Properties in the Near Field. Part I - Theory and Application. NASA CR-73106, Aug. 1967.

21. Carmichael, R. L. and Woodward, F. A.: An Integrated Approach to the Analysis and Design of Wings and Wing-Body Combinations in Supersonic Flow. NASA TN D-3685, Oct. 1966.

22. Bateman, H.: Partial Differential Equations of Mathematical Physics. Dover Publications, New York, NY, 1944, p. 190.

23. Busemann, A.: A Review of Analytical Methods for the Treatment of Flows with Detached Shocks. NACA TN 1858, 1949.